

Boronic acids in Molecular Layer Deposition

Synthesis and characterization

Veljko Petrović



Master's Degree Thesis

Materials, Energy and Nanotechnology

60 study points

Department of Chemistry

Faculty of Mathematics and Natural Sciences

UNIVERSITY OF OSLO

June / 2019

Boronic acids in Molecular layer deposition

Veljko Petrović

Thesis for the Master's Degree in Materials, Energy, and Nanotechnology

60 study points

Department of Chemistry

Faculty of Mathematics and Natural Sciences

University of Oslo

May 2019

© Veljko Petrović

2019

Boronic acids in Molecular Layer Deposition

Veljko Petrović

<http://www.duo.uio.no/>

The University Print Center, University of Oslo

Abstract

Covalent organic frameworks (COFs) are a relatively new class of materials. Although several strategies for the synthesis of COF thin films exist, efficient, and direct synthesis routes are always highly desirable. The idea behind this project was to grow thin films of COF structures such as COF-1 and COF-5 using an all-gas technique known as molecular layer deposition (MLD). Since this is an all-gas-phase technique, it is important that all the reactants can be brought into the gas phase as easy as possible. The building block of COF-1 and COF-5 structures is benzene-1,4-diboronic acid (BDDBA) and has a sublimation temperature of about 150 °C based on the results of the thermogravimetric analysis (TGA) and the precursor tester. The compound also shows tendencies to polymerize or decompose if used at higher temperatures, which is not ideal for an MLD process. The growth of COF-1 and COF-5 was studied through test depositions, quartz crystal microbalance (QCM) response experiments, and x-ray photoelectron spectroscopy (XPS), but it was not possible to achieve growth for neither of the two structures.

When BDDBA was combined with trimethylaluminum (TMA) and titanium(IV)chloride (TiCl_4) to produce hybrid films, the growth rates showed to be temperature dependent. When using TMA, we observed a decreasing trend from 1.6 Å/cycle at 180 °C to 0.6 Å/cycle at 340 °C and when using TiCl_4 from 1.2 Å/cycle at 230 °C to 0.6 Å/cycle at 300 °C. Even though it was not possible to precisely determine the growth mechanism of these two hybrid systems, the presence of boron in the films was confirmed by XPS and the presence of aromatic rings based of the results from the transmission spectroscopy in the UV and visible range (UV-Vis), and transmission and reflection spectrometry in the infrared range. These amorphous films were observed to have relatively smooth surfaces evidenced by the topography study via Atomic Force Microscopy (AFM) and density values obtained through x-ray reflectometry (XRR), being different from the density values of Al_2O_3 and TiO_2 films deposited at the same temperatures as the hybrid films.

Additionally, 1,2,3,4,5,6-Benzenehexol (BH) was combined with TMA to investigate another material system with MLD. Result of the QCM experiments performed to investigate the most optimal pulse and purge parameters showed self-limiting growth for TMA, but when it comes to BH, not even 70s seconds were enough to saturate the surface of a QCM unit at 200 °C. The analysis by Fourier transform infrared (FTIR) showed clear differences in stretching vibrations (in both transmission and reflection mode) of the hybrid TMA and BH and Al_2O_3 films deposited at 200 °C. The UV-Vis measurement of the hybrid film in transmission mode showed peaks at around 230 nm and a form of a shoulder at about 280 nm proving aromaticity of the film, and we also observed that they absorb light at about 420 nm, a feature different from the oxide film deposited at the same temperature.

Preface

The work in this thesis has been performed in the Center for Materials Science and Nanotechnology (SMN) and the research group Nanostructures and Functional Materials (NAFUMA) at the Department of Chemistry at the University of Oslo. The master project started in August of 2017 and ended in June of 2019.

I want to express my gratitude to my main supervisor Professor Ola Nilsen and co-supervisor Dr. Kristian Lausund Blindheim, for their support throughout my master project. As I hope they know, their mentoring and kindness have been essential for the completion of this project, and I consider myself lucky to have been their master student.

The thin film group at NAFUMA is filled with friendly and easy-going people always willing to help. I want to thank Kristian Weibye for measuring and analyzing my samples by XPS and helping me out with presenting the data, Thomas Aarflot Storaas for teaching me how to use an AFM. Big thanks also go to Henrik Hovde Sønsteby and Jon Einar Bratvold for helping me out with XRD, XRR measurements and whatever other problem I had in the lab. Per-Anders Hansen deserves a big thanks for his expertise in UV-Vis spectroscopy and ellipsometry measurements. I am also grateful for all the current and former students at MENA and NAFUMA employees for their support during my five-year journey at the Department of Chemistry.

Finally, I have to thank my closest ones, my mother Svetlana, my father Dragan and brother Nikola for their love and support throughout my life. My parents dedicated huge parts of their lives to the development of my brother and me, even coming to a new country. Without them and my brother, I would not be the person I am today.

Veljko Petrović
Oslo, Norway, June 2019

Table of Contents

Abstract	V
Preface.....	VII
1 Introduction	1
1.1 Historical and theoretical background	1
1.1.1 Thin films	1
1.1.2 Molecular Layer Deposition.....	2
1.1.3 Porous materials	3
1.1.4 Metal-organic frameworks	4
1.1.4.1 Thin films of metal-organic frameworks.....	5
1.1.5 Covalent organic frameworks.....	8
1.1.5.1 Thin films of covalent organic frameworks	9
1.2 Motivation.....	11
2 Theory and methods	12
2.1 Molecular Layer Deposition	12
2.1.1 Parameters affecting growth rate.....	13
2.2 Precursors.....	15
2.2.1 Precursor tester	15
2.2.2 Thermogravimetric analysis	16
2.3 Characterization of thin films	16
2.3.1 In-situ quartz crystal microbalance	16
2.3.2 Spectroscopic ellipsometry.....	18
2.3.3 X-ray Diffraction.....	20
2.3.4 X-ray Reflectometry	21
2.3.5 Fourier-transformed infrared spectroscopy	21
2.3.6 X-ray photoelectron spectroscopy.....	23
2.3.7 Ultraviolet and visible light spectroscopy	23
2.3.8 Atomic force microscopy	24

3	Experimental	25
3.1	Precursors.....	25
3.2	Depositions	26
3.3	Substrates	27
3.4	Characterization of films.....	28
3.4.1	Spectroscopic ellipsometry.....	28
3.4.2	Quartz crystal microbalance characterization.....	29
3.4.3	Fourier-transformed infrared spectroscopy	32
3.4.4	Ultraviolet and visible range spectroscopy.....	32
3.4.5	Diffraction techniques	33
3.4.6	Atomic force microscopy	33
3.4.7	X-ray photoelectron spectroscopy.....	33
3.5	Material systems investigated.....	34
4	Results	35
4.1	Precursors and their thermal properties	35
4.2	The reaction of BDBA with itself.....	39
4.3	The BDBA and HMTP system	39
4.4	The TMA and BDBA system	42
4.5	The TiCl ₄ and BDBA system.....	50
4.6	The TMA and BDBA-BPE system.....	57
4.7	The BDBA and BH system.....	59
4.8	The TMA and BH system.....	60
5	Discussion	64
5.1	Precursors and their thermal properties	64
5.2	The reaction of BDBA with itself.....	66
5.3	The BDBA and HMTP system	66
5.3.1	The study of growth	66
5.3.2	Chemical composition.....	68

5.4	The hybrid BDBA systems	69
5.4.1	The study of growth, optical and structural properties.....	69
5.4.2	Chemical identity and bonding.....	72
5.4.3	Chemical composition.....	74
5.5	The hybrid BH system.....	75
6	Conclusion.....	76
7	Future work.....	78
8	Bibliography.....	79

Abbreviations

AFM	Atomic Force Microscopy
ALCVD	Atomic Layer Chemical Vapor Deposition
ALD	Atomic Layer Deposition
ALE	Atomic Layer Epitaxy
AFM	Atomic Force Microscopy
BASF	Badische Anilin und Soda Fabrik
BDBA	Benzene-1,4-diboronic acid
BDBA-BPE	Benzene-1,4-diboronic acid bis(pinacol) ester
BDC	Benzene-1,4-dicarboxylic acid
BH	1, 2, 3, 4, 5, 6 - Benzenehexol
BOF	Boronic Organic Framework
COF	Covalent Organic Framework
CVD	Chemical Vapor Deposition
DEZ	Diethyl zinc
DFT	Density Functional Theory
EDS	Energy Dispersive x-ray Spectroscopy
EG	Ethylene glycol
FTIR	Fourier Transformed Infrared Spectroscopy
GIXRD	Grazing Incidence x-ray Diffraction
HHTP	2, 3, 6, 7, 10 , 11 - Hexahydroxytriphenylene
HKUST	Hong Kong University of Science and Technology
HMTp	2, 3, 6, 7, 10, 11 – Hexametoxytriphenylene
HQ	Hydroquinone
ML	Molecular Layering
MLD	Molecular Layer Deposition
MOF	Metal-organic Framework
MSE	Mean square error
PVD	Physical Vapor Deposition
PXRD	Powder x-ray Diffraction
QCM	Quartz Crystal Microbalance
SBU	Secondary Building Unit
SE	Secondary Electrons
SEM	Scanning Electron Microscopy
TGA	Thermogravimetric analysis

TMA	Trimethylaluminum
UiO	University of Oslo
UV-Vis	Ultraviolet-Visible spectroscopy
XPS	X-ray Photoelectron Spectroscopy
XRD	X-ray Diffraction
XRR	X-ray Reflectometry
ZIF	Zeolitic Imidazolate Framework
ZSM	Zeolite Socony Mobil

1 Introduction

Materials occupy an important place in our societies, contributing to our everyday lives, from small atomic-scale structures in our computers to constructions of hundreds of meters high. The material science research is focused on using different techniques to get to know the internal structure and characteristics of these materials, to ensure the right material is put to the right place. If we make an effort of assessing next-generation technologies and challenges, it becomes evident that one of many technological solutions depend on the development of new materials with properties superior from today's materials. Structuring materials down to the nanoscale in the form of thin films enables such superiority, giving rise to materials with either specific electrical, optical or magnetic properties or materials with particular structural features such as porosity.

However, for these materials to indeed affect most practical applications, they have to become available in large quantities and at an affordable price. Whether these materials will improve the quality of our lives depends on the development of synthesis methods that can integrate atomic-level precision with production routes that are relevant for an industrial scale. The current project is about exploring the possibilities of the molecular layer deposition (MLD) technique to fabricate coatings that belong to the family of coordination polymer materials. MLD is a synthesis method that can be scaled to an industrial level and allows molecular level control of the amount of synthesized material through alternating self-limiting gas-to-surface reactions. A more detailed description of MLD will be given in Chapter 3. The following chapter will introduce the reader to the historical and theoretical context relevant to this thesis.

1.1 Historical and theoretical background

1.1.1 Thin films

A material generally consists of a bulk and a surface. The properties of the bulk might be more imminent due to size, but it is the surface that interacts with the surrounding. Changing the surface of a material by applying a thin film with thickness ranging from 1 to 1000 nm (or more) gives rise to entirely new chemical and physical phenomena. One of the most apparent phenomena are the optical properties of thin films. An example of this is the interference pattern generated from thin films, documented already by the end of the 1600s by Robert Boyle and Robert Hooke^[1]. Some examples of thin films are displayed in Figure 1. The theory behind these discoveries was not proven until Thomas Young conducted his famous slit experiment that ultimately determined that light interferes just like water waves^[2].

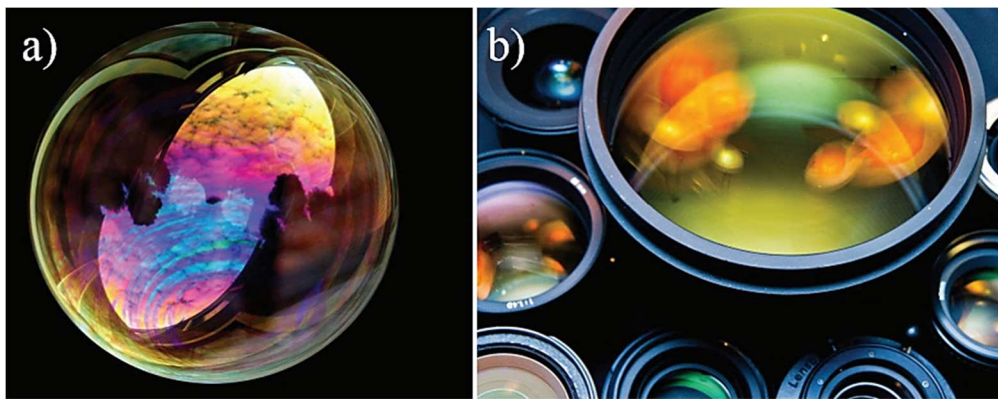


Figure 1: a) The soap bubble is showing different colors. It consists of a thin soap water film enclosed by two soap films. Light is reflected from both soap films in the same direction. The thickness of the layer of water determines which wavelength of light results from the interference^[3]. b) An image of a camera lens, the lenses are covered with anti-reflective coatings, which are thin films^[4].

The first breakthrough concerning applications of thin films was made by Justus von Liebig in 1835, providing us with today's production route of mirrors^[5]. More recently, the development of the production processes of thin films was tightly bonded to the simultaneous development of vacuum technology. Being able to acquire lower vacuum by the end of the 1920s and avoid oxidation of materials by exposure to air, enabled the development of several techniques for deposition of thin films^[6]. One of them is Physical Vapor Deposition (PVD), in which the material evaporates before it condenses onto a substrate^[7] and Chemical Vapor Deposition (CVD), where one or more types of reactants react above a substrate^[8]. In this thesis, the focus is on the MLD technique, which is a particular case of CVD.

1.1.2 Molecular Layer Deposition

Atomic Layer Deposition (ALD) is a technique that has been known for over fifty years^[9]. The principle behind ALD is based on pulsing gas-phase precursors onto a substrate to achieve self-limiting reactions that form a monolayer on the surface of that substrate. The precursors are pulsed in an alternating manner, separated by a purge step. The whole process is repeated cyclically as many times as required, and the film is produced one atomic layer at a time. ALD research began around the 1960s and 1970s in the Former USSR and Finland. In the former USSR, the technique based on the gas-phase chemical assembly of solids was initially called Molecular Layering (ML) and was developed by Prof. V.B. Aleskovskii and his Ph.D. student at the time, S.I.Koltsov^[10]. Around the same time and independent of each other's work, Tuomo Suntala and his scientific group developed Atomic Layer Epitaxy (ALE) technique. Their goal was to produce flat screens of thin electroluminescent films, which at that time was a success, as the technique provided pinhole films with low thickness gradients^[9].

The name ALE eventually changed to ALD to mark that a deposition process is not dependent on an epitaxial growth. At present, ALD is one of the most important techniques for the synthesis of nanomaterials for electronics. Later on, the MLD technique was developed, with the only difference being that ALD serves exclusively for deposition of inorganic materials, while the MLD uses one or more organic molecules as precursors. Yoshimura et al.^[11] coined the term MLD in 1991 in an article that showed that the self-limiting growth of organic polyimide films occurs when using precursors based on diamines and dicarboxylic acids. Since then, MLD was used to produce other polymer materials such as polyamides and many others. The repertoire became even more extended by realizing that metal-organic precursors could be used together with organic molecules^[12-14]. These deposition processes generated an entirely new family of materials, namely hybrid organic-inorganic thin films, where the desired material property include well-defined pores.

1.1.3 Porous materials

Development of porous materials started already with nature herself, which has for billions of years produced materials with permanent porosity. Some of the examples of such materials include skeleton structures of the simplest one-celled organisms, while others include wood, cork, and zeolites. Porous materials are generally characterized in terms of their pore sizes. The following IUPAC conventions are established for classifying pore diameter ranges: Microporous (> 2 nm), mesoporous (< 2 nm and > 50 nm), and macroporous (< 50 nm)^[15].

One of the most prominent examples of naturally occurring porous materials is zeolites. These aluminosilicates offer high degrees of structural and compositional diversity, as well as a broad range of chemical and physical properties^[16]. One example of a zeolite structure is the Zeolite Socony Mobil (ZSM) structure that has been extensively studied and applied in many domestic and industrial areas. The versatile applications of, for instance, ZSM-5 structure in catalysis, petrochemistry, detergent technology, but also as molecular sieves have excelled their importance^[17].

However, some limitations, such as their pore size and their rigidity inspired scientists to develop new types of synthetic porous materials just within the past two decades^[18]. These include the metal-organic framework (MOF) and covalent organic framework (COF) structures, which have demonstrated various porous topologies and other remarkable properties. The defining features of these materials are their coordinative and strong covalent bonding combined with a continuous lattice arrangement. As such, these materials tend to be extremely durable, chemically, and thermally stable, while also providing various technologically important applications^[19]. Additional theoretical and historical background on MOF and COF materials is given in the following chapters. When it comes to porous thin films materials, several technological areas are centered on porosity because it represents the critical parameter that drives the efficiency and suitability of the thin films for the

specific application. In catalysis, porosity determines the number of active sites available for the reactants, meaning that the catalytic activity is a function of pore sizes. The operating characteristics of sensors are also affected by porosity. From these examples and many others, we can see that porous thin films are of high scientific and technological interest due to their ability to either interact with or selectively exclude, different species like ions, atoms, and molecules (both in the solution and in the gas phase).

1.1.4 Metal-organic frameworks

MOFs are hybrid materials composed of inorganic metal ions or clusters and organic linkers. One of the earliest reports of MOF-like structures came from the 1989 publication by Hoskins and Bernard^[20] where they express the thought of possible joining of tetrahedral and octahedral metal cores through organic bridging joints to generate well-ordered cavities. Their research gave a basis for believing that the acquired MOF-like materials “may show interesting molecular sieve or ion exchange properties, have unusual mechanical and electrical properties, but also may provide tailor-made materials for heterogeneous catalysis.” At that time, the structures we now refer to as MOF’s were called coordination polymers.

In another article by Shah et al.^[21], MOF’s were also defined as coordination polymers, where organic linkers act as Lewis bases donating two electrons to the metallic tetrahedra, or Lewis acids, forming covalent coordination bonds. What is interesting about MOF’s is their permanent porosity and impressively high surface areas. Further interest in MOFs arose based on the possibility of exchanging metallic constituents - also known as secondary building units (SBU), or the organic linkers, thus being able to create entirely new MOF materials that can be tailored to meet the needs of a given application. These SBU’s are used as simplifications, making it easier to classify MOFs (Figure 2).

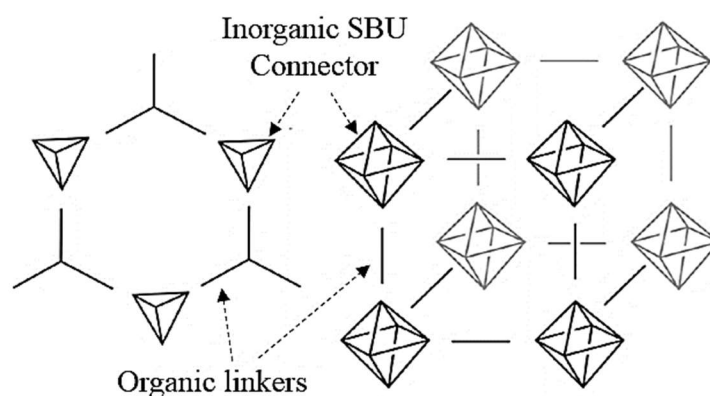


Figure 2: An overview of general MOF structure composed of inorganic SBU and organic linkers.

The MOF materials truly gained attention with the publication of an article on MOF-5 (Figure 3a) structure by Yaghi et al.^[22] in 1999. They showed a stable MOF structure after the removal of the solvent, which was previously only proved to be the case for zeolites. Since then, through the substitution of the organic linkers but also SBUs, the field has expanded to countless different conformations of MOF materials and now encompasses more than 60000 different structures^[23]. Some of these structures are HKUST-1 developed at Hong Kong University for Science and Technology (HKUST), ZIF-8 (ZIF- Zeolitic imidazolate framework) and UiO-66 developed at the University of Oslo (UiO), shown respectively in Figure 3b) – d).

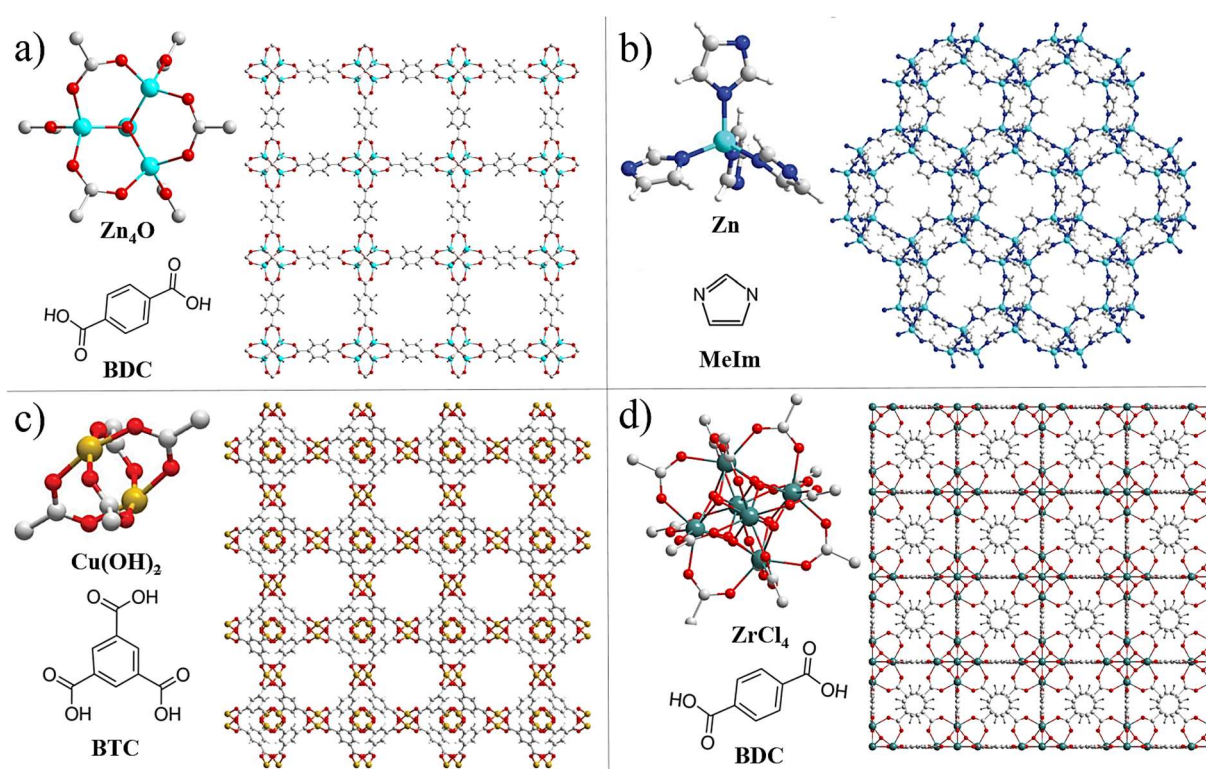


Figure 3: The overview of the first stable MOF structure a) MOF-5 composed of Zn_4O ions and 1,4-benzenedicarboxylic acid linkers b) ZIF-8 composed of Zn atom bound to four imidazolate rings c) HKUST-1 made of copper hydroxide and 1,3,5-benzenetricarboxylic acid and d) UiO-66 composed of $ZrCl_4$ and terephthalic acid. The structures were made based on CIF-files from Lock et al.^[24], Karagiari et al.^[25], Yakovenko et al.^[26], and Øien et al.^[27], respectively.

1.1.4.1 Thin films of metal-organic frameworks

In the first review article on the topic of MOF thin films, Zacher et al. discuss that one of the challenges in MOF research is growing MOF thin films on substrates, ideally in a dense, homogeneous and oriented fashion^[28]. The interest in MOF thin films has mainly been initiated due to the increasing demand in adjusting the optical, electrical, or mechanical properties of surfaces and interfaces^[29]. Since then, different methods were developed, and solvo- or hydrothermal methods are the most prominent ones^[30]. In these methods, reactions are carried out in solvents (such as water) at

high temperatures in closed vessels using templating agents^[31-33]. There are now other interesting methods documented as alternatives striving to correct for long reaction times, high temperatures, and reactant concentrations. These include layer-by-layer growth^[34], electrochemical^[35], sol-gel growth^[36], spray coating^[37] and now even MLD growth^[38, 39]. In the layer-by-layer growth developed by the scientific groups led by Woll and Fischer, a sample is sequentially added into three solutions: a solution containing a metal salt, a washing solution to remove excess metal precursor and a solution containing the organic linker.

The first example of the electrochemical growth of MOF thin films was the synthesis of HKUST-1 (Figure 3c) reported by researchers at BASF^[40]. Here, the metal source serves as an electrode and is placed in a solution containing both linker and an electrolyte. When a specific voltage is applied, the metal dissolves and releases ions that are located near the surface of the electrode. These ions react with the linkers so that a MOF structure is built as a result. The microwave-induced method is a method where MOF nanocrystals are grown on carbon-coated porous Al₂O₃ surfaces. In the report by Yoo et al., this rapid synthesis route of producing MOF-5 thin films (Figure 3a) gives nearly full surface coverage.

The advantage of all of these and many other solvent-based synthesis routes is their simplicity. However, the drawbacks of using solvents often involve surface-tension related issues like incomplete wetting or even deformation (or contamination) of the substrate where the films are formed^[41]. This is not desirable for future implementation of MOF structures in, for instance, electronic devices. That is why the recently developed all-gas phase methods of synthesizing MOFs have gained attention. The vapor phase routes allow precise control of the thickness of the obtained films, selection of properties, while also providing an overall better film quality.

The first attempt at MLD growth of MOF films was reported in 2013 by Salmi et al.^[42]. These films were deposited by MLD at 250 °C using zinc acetate and 1,4-benzenedicarboxylic acid (BDC) as precursors. The as-deposited films were amorphous and non-porous but could be crystallized by exposure to humidity and an autoclave treatment in DMF. After this, the MOF-5 crystalline structure was identified by XRD, and the presence of micropores was found by ellipsometry. Unfortunately, film homogeneity was lost during the autoclave treatment as a result of dissolution and other issues due to the high mobility of the intermediates in the solvent. This article nevertheless showed that autoclave treatments for crystallization of amorphous films could be used as a strategy for MOF all-gas phase depositions.

In another article in 2016, copper-2,2,6,6-tetramethyl-3,5-heptanedionate and BDC were used as precursors for MLD growth of a Cu-based MOF structure^[43]. Here, a narrow MLD temperature window was observed – from 180 to 190 °C. It was also investigated if crystalline films of this MOF structure could be obtained. Similarly, thin films of stable UiO-66 MOFs (Figure 3d) were synthesized using MLD and published in an article by Lausund and Nilsen^[38]. Alternating reactions of ZrCl₄ and BDC produced amorphous hybrid film structures that were subsequently crystallized to the UiO-66 structure using an autoclave treatment with acetic acid. A follow-up article demonstrates thin film deposition of functionalized UiO-66 using amino-functionalized linkers that gave rise to a more straightforward crystallization process^[39].

MOF or hybrid thin films based on boron or boronic acids have not previously been mentioned in the scientific community. However, a DFT investigation was done by Gao et al.^[44] predicts boron aryls being linked together by isocyanides forming structures they referred to as Boronic Organic Frameworks (BOFs). In these structures, the boron acts as a metal center forming bonds with the cyanide linkers. Even though it is just a prediction, the unusual bonding in BOFs gives rise to exciting semimetal and narrow band-gap features that are unique for MOF's and COF's.

Before crystalline MOF thin films were realized by MLD, the technique was used to create hybrid thin films or so-called metalcones. The way these structures are constructed is that the organic part is usually alcohol combined with an inorganic component^[45]. The procedure was introduced by Nilsen^[46] in 2003, and many structures have since then been made. It has been reported on the use of carboxylic acids, alcohols, and amines in combination with metal-organic compounds such as trimethylaluminum (TMA) and diethyl zinc (DEZ), but also metal-halides such as titanium(IV)chloride (TiCl₄).

Klepper et al.^[47] have used various amino acids and carboxylic acids as a functional group in combination with TMA. The films were grown in the temperature range of 200–350 °C and have shown growth rates as high as 20 Å per cycle. Growth using a range of other organic linkers, such as hydroquinone (benzene-1,4-diol), has also been documented, resulting in the films growth rate of 3.5 Å per cycle between 150 and 400 °C^[13]. Similar depositions were done with linkers having three –OH groups instead of two (phloroglucinol)^[12], while the use of a benzene ring with six –OH groups as in 1,2,3,4,5,6-benzenhexol (BH) has not been reported used before in MLD reactions. However, BH has been used as a linker to make a conductive copper-based MOF structure^[48]. In this article by Park et al., hydrothermal synthesis route yields a 2D MOF with a bandgap of about 1 eV and a temperature dependent conductivity.

1.1.5 Covalent organic frameworks

COF structures have entered the scientific scene in the last ten year. Unlike MOFs, they do not contain metal ions and consist entirely of light elements such as carbon, boron, and oxygen and are held together by strong covalent bonds. The modular nature of these materials allows the integration of different molecules with π -systems into highly ordered polymers with very low densities and high thermal stabilities. These polymers extend periodically in 2D or 3D depending on the shape of the monomer. The building principle is best illustrated in Figure 4, where the extended structures are comprised of linkers (building units) and linkages^[49].

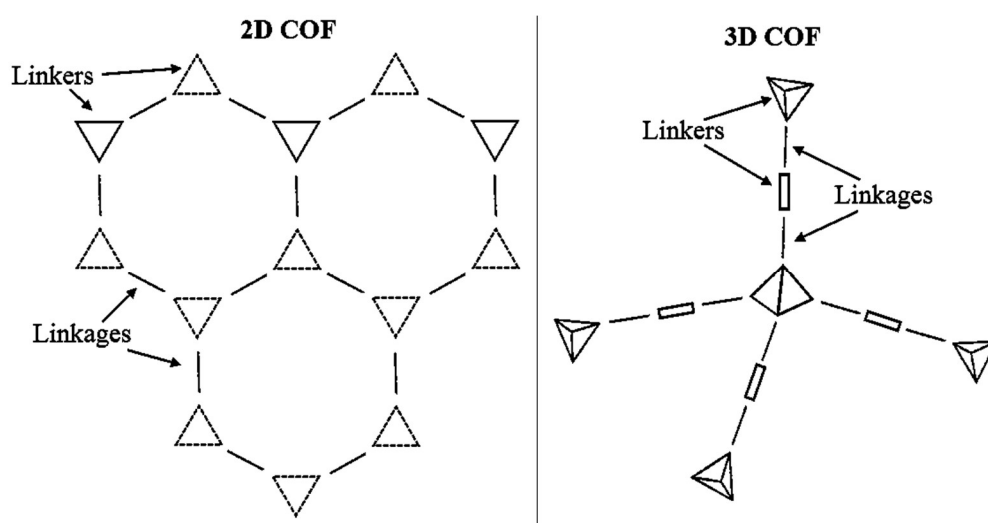


Figure 4: An overview of 2D square lattice based on square planar and linear monomers and a 3D net structure based on tetrahedral and linear monomers. Both based on two main components: linkages and linkers.

The fundamental concept of making COF structures came initially from the 1916 paper by Gilbert N. Lewis. The idea of covalently bonding atoms to form molecules has been the cornerstone for all of organic chemistry and has been used to make very complex molecules. The organic chemistry was for a long time limited to a zero-dimensionality, but the obstacles were overcome by the first documentation of 2D COF in 2005 by Cote and Yaghi^[50].

Their paper presented the synthesis of highly robust and thermally stable and porous COF-1 and COF-5 based on dehydration reactions between benzene-1,4-diboronic acid (BDBA) and 2,3,6,7,10,11-hexahydroxytriphenylene (HHTP). The structures are presented in Figure 5. The condensation of the BDBA first gives rise to a planar six-membered ring of boroxine (B_3O_3) and the elimination of three water molecules to obtain COF-1 while BDBA is copolymerized with HHTP to produce a boronated ester structure and COF-5.

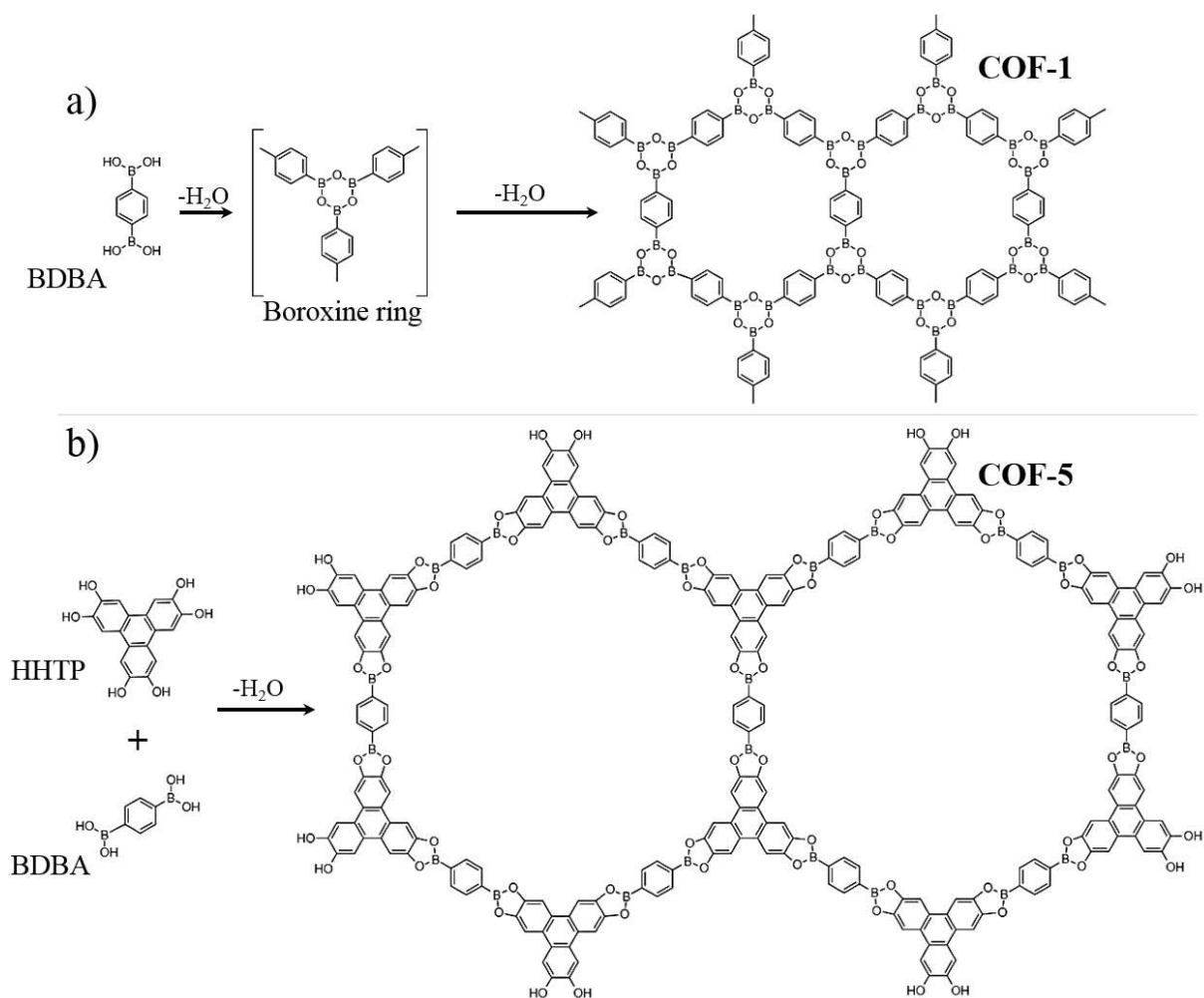


Figure 5: Reaction schemes for the self-condensation reaction forming a boroxine ring and the COF-1 structure (a) and the co-condensation reaction with vicinal diols in HHTP forming a boronated ester and the COF-5 structure (b).

1.1.5.1 Thin films of covalent organic frameworks

The interest in 2D-COF thin films has arisen because of the stability of covalent bonds, the diversity of available monomers and the exciting properties of COFs, such as their porosity, that exceeds even zeolites^[51]. There are now several ways to grow films of these structures. Just as mentioned for MOF's, quite many of these are based on solvo- or hydrothermal routes. In all of the cases, the mixture of different building blocks is heated for several days, after which the solid is extracted, washed with specific organic solvents and finally dried using a flow of N₂.

Formation of COF-1 and COF-5 thin films, for example, was reported already on substrates such as single-layered graphene^[52] and metal oxide surfaces such as indium doped tin oxide^[53]. In both cases, the fabricated films were mentioned as promising in the field of electrocatalysis and as potential parts of energy storage devices. Smith et al.^[54] invented another similar method, reporting on freestanding porous COF-5 films after a solvent cast modulation of the colloidal COF-5 particles.

According to their findings, the obtained films may be excellent in protein immobilization and therefore suitable for use in bio sensing or catalysis. However, these methods do not give possibilities of effective control of the thickness or homogeneous coverage of the films. Wanting to solve this problem, an article by Evans et al.^[55] reports on using a seeded growth method, where COF-5 films are grown by slowly adding BDBA and HHTP to preformed nanoparticle seeds. More recently, thin films of 2D COF were grown using interfacial methods^[56]. Feldblyum et al.^[57] attempted to synthesize COF-5 (among others) at a liquid/air interface, which was believed to be an excellent interface for control of COF nucleation and thickness. In the experiment that took over several days, the acquired films showed too high roughness for integration into devices.

On the other hand, solvent-free methods were developed, such as the one reported by Spitzer et al.^[58] where monolayers of COF-1 were synthesized in a condensation reaction of boronic acids. The acids were deposited in an all gas-phase process, while water is used for equilibrium corrections. A similar approach was published by Zonneveld et al.^[59], where both COF-1 and COF-5 were thermally sublimated onto clear surfaces of Ag (111) in ultra-high vacuum. The sublimation temperature range was reported to be between 90 and 200 °C.

Considering the thermal instability of monomers that may be sensitive to the harsh conditions used in solvent-based methods, Bein et al.^[60] proposed a room temperature vapor-assisted conversion synthesis. COF-5 films were made to verify this strategy, a mixture of BDBA and HHTP, dry acetone and ethanol were first filtered through a syringe filter after ultra-sonication. Then, the obtained mixture of BDBA and HHTP was drop-casted on a glass substrate, followed by putting the substrate in a desiccator together with a small glass vessel loaded with mesitylene and dioxane. In their work, it was reported that the control of the thickness might be achieved by tailoring the volume of the droplets and the concentration. This method allows the construction of COF thin films with fragile precursors and on sensitive substrates, and may therefore leads to a broader range of applications.

In contrast to the conventional growth procedure, Dichtel et al.^[61] synthesized a COF thin film with a much smoother and denser surface under continuous flow conditions. Considering the poor control over the polymerization in the previous method, they modified the growth of the 2D COF thin films using a flow cell, which enabled the formation of the COF. To synthesize COF-5 in a flow cell, the monomers BDBA and HHTP were first reacted slowly at 25 °C, and then COF-5 formed after 2 min of induction period when the temperature rose to 90 °C. There are different techniques for growing thin films of 2D COF materials, however, the MLD technique is never mentioned in the literature.

1.2 Motivation

The focus of this master project is to attempt to synthesize 2D COF thin film using boronic acid precursors by MLD. If successful, it would be the first example where such growth is demonstrated using this technique. Similar porous framework thin films have already been synthesized successfully in our research group^[38, 39], so the motivation is to continue to extend the repertoire of what we can make with the MLD technique. Additionally, the intention is to expand the repertoire even further by using BH as a precursor to synthesize hybrid films. None of these precursors were previously used concerning the MLD, so, at first, the general focus of the project is the synthesis process and control of the growth mechanisms, in addition to the characterization of properties of the synthesized films. It is motivating to see that article by Pawlak et al.^[62], reports on BDBA sublimating in vacuum at around 130 °C, which we believe is a good starting point for the MLD technique with this compound.

The same arrangement of -OH groups as in COF structures are also present in glucose, and the well-known reversible interaction between boronic acids and 1,2-diols or 1,3-diols has led to the development of boronic acid-based saccharides sensors^[63, 64]. If making COF thin films with MLD is successful, it would also mean that making a single layer of boronic acid would be possible to do with this technique. This could be beneficial in developing tools that can quickly and with a precision monitor incurable conditions such as diabetes^[65] but also produced at a low cost. When it comes to COF materials, the primary focus has been to characterize COF films more efficiently, but also to understand mechanisms and optimal crystallization conditions. Another focus has been on developing routes to integrate COFs into devices (glucose sensors) but also making freestanding films.

2 Theory and methods

This chapter presents the theory behind the experimental techniques used in this thesis. Synthesis and control of the growth mechanisms of the thin films are the essential parts of this work, so a more thorough description of the deposition technique is given. Additionally, various characterization methods that are used in this thesis will also be described.

2.1 Molecular Layer Deposition

ALD is a vapor phase thin film deposition technique based on alternating self-limiting gas-to-surface reactions^[66]. This approach enables good control over the thickness of the films as well as their stoichiometry^[67]. A minimum of two reactants, called precursors, are required for a typical ALD deposition. An excellent example of a deposition is the synthesis of aluminum oxide using trimethylaluminum (TMA, $\text{Al}(\text{CH}_3)_3$) and water^[9]. However, instead of using water, ethylene glycol (EG, $\text{C}_2\text{H}_6\text{O}_2$), which contains two hydroxyl groups, may be used to produce aluminum alkoxide or alucone. This is an example of MLD growth, based on the same principles as ALD but differing from regular ALD in that it has an organic molecule as one of the precursors^[68]. In both examples, the method is divided into multiple steps that altogether constitute one cycle. Figure 6 shows an MLD cycle with two precursors illustrated stepwise from 1) to 4).

- 1) TMA enters the reaction chamber, initiating a gas-to-surface reaction with the substrate, while the byproduct CH_4 is formed. The first step ends when the surface of the substrate is saturated, and there is no room for additional TMA molecules.
- 2) The reaction chamber is then purged typically with an inert gas like N_2 , removing the excess of the physically adsorbed or unreacted precursor as well as byproducts, so that, after step 2, the process ends with a chemically bonded monolayer.
- 3) Pulsing of EG, the second precursor, so that it reacts with the new surface, done until this new surface is saturated. EG reacts with TMA and produces CH_4 at the same time as the remaining hydroxyl groups bind to the remaining alumina atoms.
- 4) The cycle is completed by the fourth step, where another purge removes the excess of the second precursor and byproducts. Usually, excess EG and CH_4 are evacuated with the same inert gas. In this way, a layer of alucone is produced on the surface of the substrate.

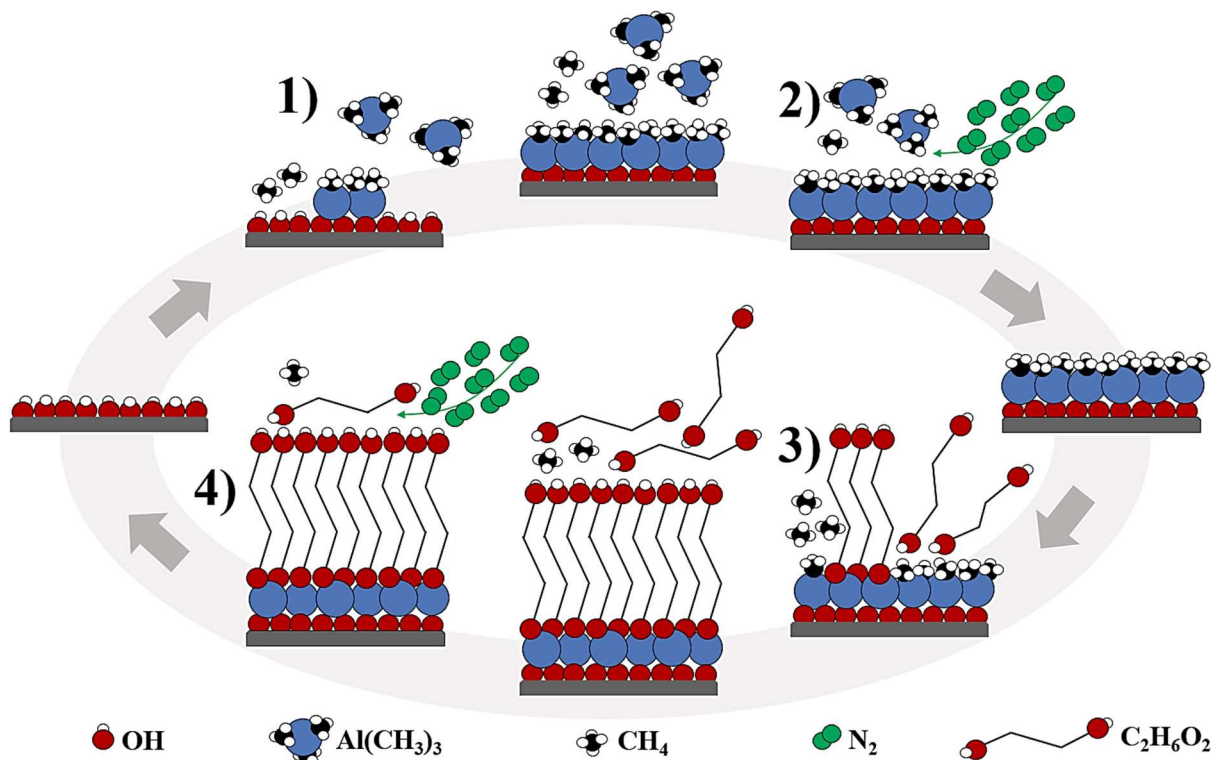


Figure 6: A simplified illustration of one cycle of an MLD of aluminum alkoxide using sequential pulsing of TMA and EG separated by an inert gas that is purging. After one cycle is over, the starting -OH terminated group is recreated, which allows for a repetition of another cycle to build up a thin film with a near monolayer precision. Under controlled pulsing and purging, the self-saturated reactions allow the MLD film to be formed with very high conformity.

2.1.1 Parameters affecting growth rate

The growth rate of deposited thin films such as the one described above is quantified by the amount of film deposited with each cycle^[69]. The variations in growth rates can give information about the reactivity of the precursor and the conditions that lead to optimal growth. The three main parameters that affect the growth rate most are the pulse and purge lengths and the temperature at which the reactions occur. Both the precursors pulsing and purging lengths should be sufficiently long to ensure feasible self-limiting growth^[70].

Figure 7a) presents thickness per cycle growth rate as a function of pulse lengths, where the saturation point is located where additional pulsing of the precursor does not result in more growth^[71]. This saturation can occur either fast or slow (represented by the solid black curves). An indication of possible decomposition of the precursor would be if the saturation point is not reached, and the growth rate increases because of too high temperature (dotted black curve). However, a lower growth rate is usually an indicator that the precursor molecules are starting to etch the molecules that have already bonded to the surface of the substrate (dashed black curve)^[72, 73].

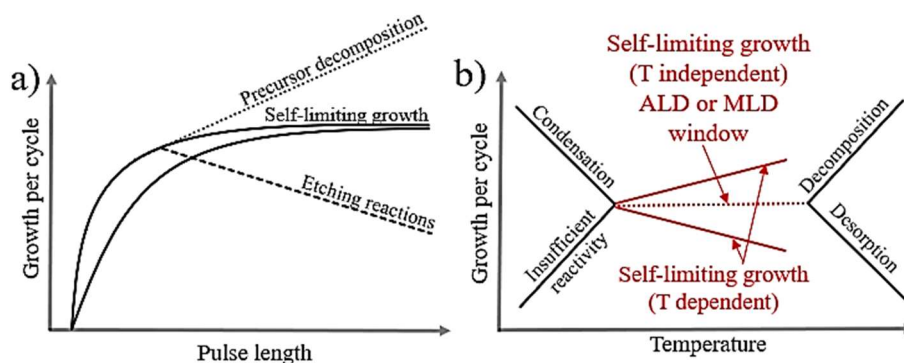


Figure 7: a) Different growth rates as a function of pulse lengths where the saturation is fast and slow (solid black curves), saturation followed by decomposition of the precursor (dotted black curve) and saturation followed by etching (dashed black curve). b) Schematic depiction of ALD (or MLD) window. Outside the window, condensation and decomposition of precursor lead to increase, while incomplete reaction and desorption or loss of surface species lead to a decrease in growth per cycle.

Purge times, on the other hand, should not be too short because it could result in insufficient removal of the excess precursor molecules^[73]. Unwanted reactions can occur in the gas phase, creating a CVD-type growth. Large thickness gradients and an increased growth rate are usually good indicators of such reactions. Very long purge lengths, on the other hand, may provoke the inert gas to evacuate the chemisorbed precursor molecules from the film, resulting in a much lower growth rate^[74]. The effect of temperature on the growth per cycle value is described by a concept known as the ALD (or MLD) window, where thin-film growth proceeds in a self-limiting manner. It is represented by a dotted red line in Figure 7b). This is the most optimal temperature interval, where precursors do not condensate in the reaction chamber (due to low temperature), where there are no kinetic and bond decomposition or desorption of the precursors.

Outside of the window, the growth can be either lower or higher^[9, 71]. At lower temperatures, the precursors or the generated by-products from the previous pulse may condensate (or adsorb to the surface) leading to a CVD type growth^[73] or the surface reactions do not have enough thermal energy to reach completion leading to a lower growth rate. On the other hand, at higher temperatures, the precursors may decompose and provoke additional adsorption^[75]. The functional groups on the surface of the substrate may also desorb at higher temperatures being lost from further reactions^[76]. A deposition cycle may not always lead to a complete monolayer of the deposited material. The reason for this is that precursor molecules of a certain size can block some of the reactive sites on the surface of the substrate. This is called steric hindrance and is dependent on the density of these reactive sites and the flexibility and size of the precursors^[77].

2.2 Precursors

A central part of the development of new materials is to investigate and find precursors that can be used in MLD. Precursors can be elementary, inorganic, organic, organometallic, but at the same time, either gases, liquids, or solids^[7, 73]. Vapor pressure, for example, becomes extremely important as a property of controlling the saturation of surfaces in the shortest possible time^[78]. Solid precursors usually have lower vapor pressures than the liquids. Smaller molecules are often more volatile than larger ones. Monomers are more volatile than dimers, while polymers are not volatile at all. Puurunen et al.^[69] list the following precursor properties as a must requirement:

- Sufficient volatility
- Aggressive and complete reactions
- Thermal stability (in other words no self-decomposition)
- No etching of the film or substrate
- No dissolution into the substrate
- Necessary purity of the compound

2.2.1 Precursor tester

To test some of the properties of potential precursors, a unit for characterizing the thermal properties of precursors has been developed at the Department of Chemistry. This setup is based on the use of a thermocouple, and a quartz crystal microbalance (QCM) (Chapter 3.4) that combined gives the possibility of characterizing the temperature interval where the chosen chemical sublimates or decomposes. A QCM unit is set directly above or to the side of the sample holder to detect the increase in mass due to condensation of the sublimed precursor. The temperature of the sample holder increases following a pre-determined profile, and it is registered as a function of time. The setup is illustrated in Figure 8, while the whole process is typically monitored with a time-lapse camera.

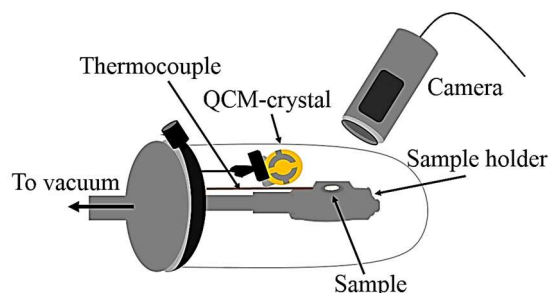


Figure 8: A schematic setup of the homemade precursor tester. The chosen precursor is placed in the alumina-based sample holder. The temperature is monitored using the thermocouple connected to the sample holder. A QCM unit is set directly above or to the side of the sample holder to detect an increase in mass due to condensation of the sublimated precursor.

2.2.2 Thermogravimetric analysis

Thermogravimetric analysis (TGA) is a similar technique in which the mass of a sample is monitored as a function of temperature (or time) as the sample is subjected to a controlled temperature profile in a controlled atmosphere. It consists of a small sample holder that is supported by a balance mechanism. The sample holder is residing in a furnace while heated or cooled during the experiment. The samples mass is monitored while a purge gas controls the sample environment. This carrier gas is usually an inert gas, like N₂ or Ar. This is displayed in Figure 9.

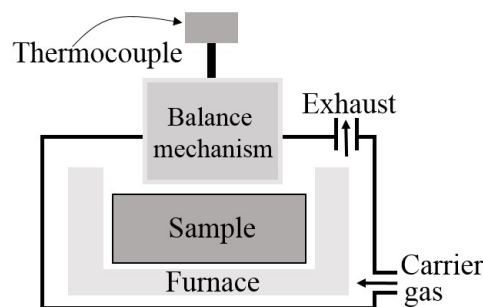


Figure 9: A schematic illustration of the thermogravimetric instrument and setup where the continuous weighing of the sample is possible as a function of temperature in an inert gas environment.

Being able to quantify the mass loss concerning time and temperature, one can deduce if the chosen sample sublimates or decomposes and to estimate the minimum temperature where it can be used as a precursor for MLD. The samples should be homogenous powders that are distributed equally in the sample holder, typically made of Al₂O₃, Al, Pt, or SiO₂^[79, 80]. It is important that these do not react with the sample, that they tolerate the maximum temperature of the temperature profile, but also the atmosphere of the analysis^[81]. The maximum and minimum heating and cooling protocols can vary between different instruments, but it is dependent on what the aim of the analysis is. For instance, when testing sublimation temperatures for a substance, it may be desirable to have a heating rate of 1 °C/min (1-20 °C/min is typical) and the end temperature of 300 °C, similar as in the precursor tester.

2.3 Characterization of thin films

2.3.1 In-situ quartz crystal microbalance

An interesting property of piezoelectric materials such as quartz is that they can generate electrical voltage upon mechanical stress. Based on this, the piezoelectric materials can either shrink or expand, depending on the alternating electrical field applied to them^[82]. Whenever mass is deposited on such crystal (like inside an ALD reactor), the frequency of the crystal changes.

This property can be used to analyze film growth and reaction properties. Figure 10 is an illustration of a QCM unit^[83].

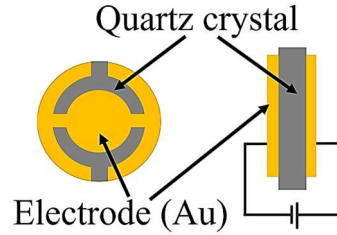


Figure 10: A piezoelectric QCM-unit with gold electrodes. a) Seen from above b) from the side, with applied voltage. The voltage leads to a deformation of the Sears modulus in the crystal.

While the reaction is happening with the surface of the crystal, the frequency change can be monitored. This relationship is expressed mathematically through Sauerbrey's equation (Equation 1).

$$\Delta f = -\frac{2f_0^2 \Delta m}{A\sqrt{\mu\rho}} \quad (1)$$

where f_0 is the resonant frequency and Δf is the change in frequency from the original. A is the piezoelectrically active crystal area (area of the electrodes, cm^2), the deposited mass is denoted m , while μ and ρ are the Shear modulus and the density of the crystal, respectively. All of the elements on the right, apart from the mass, are constant, so the change in resonant frequency is proportional to the mass change^[70, 84]. The frequency change is converted to mass change using the measured values for density and growth rate of films deposited with the same deposition parameters such as the standard pulse and purge sequence in the QCM experiment. Normalization of the depositions with the response from these standard sequences corrects for the surface roughness on the crystal, and the Sauerbrey's formula is therefore used indirectly. The mass change is calculated using Equation 2.

$$\Delta m = -\frac{r_{growth} \cdot \rho}{\Delta f_{ref} \cdot t} \cdot \Delta f \quad (2)$$

where r_{growth} represents the growth rate of the deposited film as a reference, measured with spectroscopic ellipsometry and ρ is the density of the film, measured with XRR. The term Δf_{ref} is the measured change in frequency per second in the QCM-experiment and t is time. Δf is the observed change in frequency, which converts gradually as the frequency per cycle and Δm ends up with a unit $\frac{\text{ng}}{\text{cm}^2}$. The in-situ QCM is a very suitable method for analyzing the self-limiting growth (Figure 7a). It gives the possibility of determining the optimal pulse and purge parameters, but also the dynamics of the growth conditions. Since hybrid materials may be air sensitive, such in-situ method

can give a substantial amount of information without exposing the films for air. On the other hand, the method is very sensitive towards temperature variations, where the increase in temperatures gives the same signal as loss of mass^[85]. The quartz crystal must, therefore, be held at a constant deposition temperature, and a thermal equilibrium period of ca. 1 hour is added to the program before the deposition begins.

2.3.2 Spectroscopic ellipsometry

Spectroscopic ellipsometry (SE) is an optical measurement technique that characterizes light reflection (or transmission) from thin film samples. Electromagnetic radiation consists of both the electric and magnetic field positioned perpendicular to each other^[86]. To describe the theory behind this technique, it is enough to consider the contribution of the electric field in space, also known as polarization. Light from normal sources are usually not polarized but can be polarized when passing through a filter. Two light waves that have the same wavelength are in phase, and their product is therefore linearly polarized. However, introducing phase differences between them will result in an elliptical polarization^[87]. This is displayed in Figure 11.

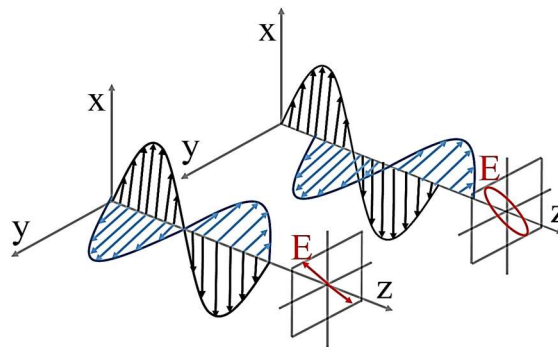


Figure 11: Two different types of polarization (left) linear, where the electric field wave is accompanied by a magnetic field wave as illustrated and (right) elliptical consisting of two perpendicular waves of unequal amplitude that differ in phase by 90° .

The key feature of SE is to measure the change in polarized light upon light reflection on a sample^[88, 89]. The name comes from the fact that linearly polarized light becomes elliptically polarized upon reflection^[87]. SE measures two values, the amplitude ratio and phase difference between light waves known as p- and s-polarized light waves. The spectrums of these values are measured by changing the wavelength of light and are eventually fitted to a mathematical model, providing information about the thin films thickness and refractive index^[90]. The incoming and the outgoing beam together with the normal vector of the surface constitute the plane of incidence. The amplitude of the electric field that is moving in the plane of incidence is denoted E_p .

Similarly, the amplitude moving orthogonally to the plane of incidence is denoted as E_s . Both are displayed in Figure 12. In ellipsometry, the s- and p-components of these electric fields are typically investigated concerning each other when the incoming beam is reflected^[89, 91].

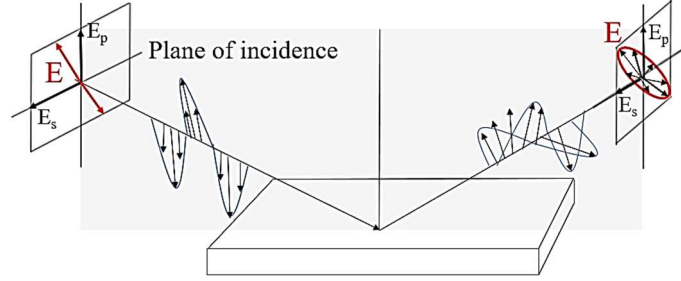


Figure 12: Schematic representation of the principle behind spectroscopic ellipsometry, where a linear polarized light is sent onto the sample. The elliptically polarized light is reflected and measured.

Before and after the reflection, the amplitude of the p-component and the s-component of the wave is changing, while the relationship between the incoming and the outgoing amplitudes is defined as the reflectance R ^[91]. The ratio between these two reflectances is ψ and mathematically expressed through Equation 3.

$$\tan \Psi = \frac{|R_p|}{|R_s|} \quad (3)$$

Similarly, the change in polarization is typically characterized as the change in phase of the p-component, and the s-component of the wave before reflection denoted δ_1 and after the reflection δ_2 . So, the parameter Δ is expressed by Equation 4.

$$\Delta = \delta_1 - \delta_2 \quad (4)$$

Finally, various mathematical methods are used to fit both Ψ and Δ . The models consist of variables such as thickness and other optical properties^[92]. For transparent samples, Cauchy's model is typically used by Equation 5.

$$n(\lambda) = A_0 + \frac{B_1}{\lambda^2} + \frac{C_2}{\lambda^4} \quad (5)$$

where n is the refractive index, A, B, and C are the Cauchy's coefficients, and λ denotes the wavelength of light^[93]. Agreement between the chosen mathematical method and the actual data can be determined by the mean square error (MSE)^[88, 92].

2.3.3 X-ray Diffraction

X-ray diffraction (XRD) methods are essential when it comes to determining crystal structures of materials^[94, 95]. When the incoming x-rays, generated from an x-ray tube, meet regularly spaced particles with a spacing comparable to the wavelength, diffraction occurs^[95]. The resulting interference pattern is dependent on the phases of the diffracted waves. X-rays have short wavelengths and high energy, so when these interact with a solid material, some of the waves are scattered in all directions by the electrons of the atoms that make up the solid^[96], assuming a crystal with parallel planes A and B, as shown in Figure 13. The spacing between the planes is given by d_{hkl} , where h, k, and l are the Miller indices of the plane. A monochromatic beam of x-rays with wavelength λ hits these planes at an angle θ . Imagine two waves are scattered by the atoms P and Q and leave the crystal under at the same angle θ ^[97].

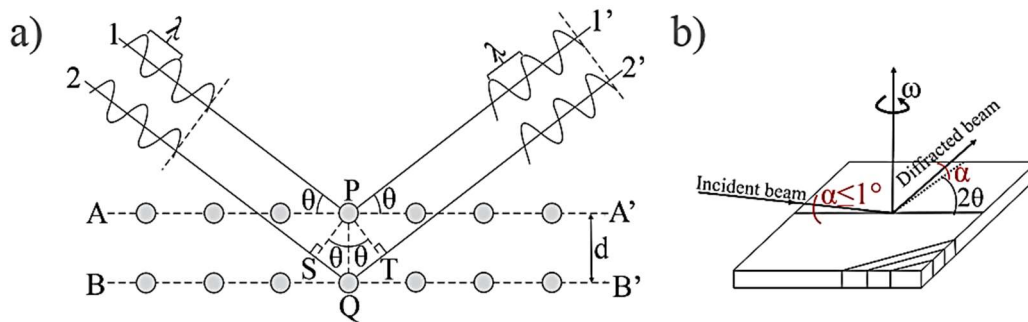


Figure 13: a) Bragg diffraction by crystal planes. The path difference between beams 1 and 2 is $SQ+QT = 2PQ\sin\theta$. b) Schematics of the symmetric GI-XRD geometry. a) taken from [97].

Constructive interference occurs when the diffracted waves are in phase. Thus, the path difference between waves $1 + 1'$ and $2 + 2'$ should be equal to exactly one (or many) wavelengths. The path difference is $|SQ| + |QT|$ equal to $2d_{hkl} \cdot \sin(\theta)$ using Pythagoras theorem. This results in Bragg's law (Equation 6), where n is an integer^[94, 97].

$$n\lambda = 2d\sin\theta \quad (6)$$

The diffracted beams enter a detector that measures the intensity of these as a function of θ (constructively interfering beams having much higher signals). In the case of thin films, the analysis is best performed if the incoming x-ray is limited to the surface of the sample. This is usually done using Grazing-incidence x-ray diffraction (GIXRD)^[98]. In such experiments, the x-ray penetrates the surface of a thin film at an angle $\alpha = 1^\circ$ or less^[98, 99]. GIXRD data can be collected using a $\theta/2\theta$ or a ω scan. Using $\theta/2\theta$ scan both the film and the detector are scanned at a speed of 1:2 to record the diffraction along a fixed direction on the substrate. In the ω scan, the detector does not move, and it is a fixed

angle 2θ , while the film rotates about its surface to record in-plane diffraction from lattice planes, which have the fixed value of d spacing^[99]. Both cases are shown in Figure 13b), and in our group, we have the possibility of collecting data in both ways.

2.3.4 X-ray Reflectometry

Where XRD measurements are used to obtain crystallographic information about structures, x-ray reflectometry (XRR) instead gives information on parameters such as thickness, density, and surface or interface roughness. This is done by analyzing the x-ray reflection intensity curves from grazing incident x-ray beam^[95, 100]. The reflection of the x-rays is based on the transition between the air and the thin film and between the thin film and its substrate. If the angle α from for the incident beam in Figure 13b) is lower than the so-called critical angle for the material, we get total reflectance^[94]. For larger angles, the incident beam penetrates through the surface and into the film. This critical angle is directly proportional to the density of the film material.

The refracted x-ray will also be reflected off the interface between the film and the substrate and will cause either destructive or constructive interference with the reflected x-ray from the film surface, giving rise to Kiessig fringes^[101]. The oscillation frequencies of these fringes can be used to determine the thickness of the films. The denser the maximum of these oscillations, the thicker the film^[102]. The roughness of the samples can be determined by increasing α and investigating the amplitude of these oscillations and variations in the slope of the signal with θ . To measure the density, roughness, and thickness for the desired film from the XRR data, a mathematical model needs to be employed, which is made from the collected information about the sample^[103].

2.3.5 Fourier-transformed infrared spectroscopy

In contrast to XRD and XRR, which are based on interactions between materials and x-rays, Fourier transformed infrared spectroscopy (FTIR) examine vibrations of chemical bonds as a result of excitation by infrared light. FTIR takes advantage of the fact that nearly all compounds with covalent bonds, either organic or inorganic, absorb certain wavelengths in the IR region and that the degree of this absorption is proportional to the molecular concentration. The wavelength region of infrared is from about 780 nm to 1000 μm ^[82, 104]. The absorbing frequencies of some atom groups are not very dependent on the whole structure at hand.

Using FTIR, these can serve as characteristic bands for the atom groups. The absorption or transmission of the IR radiation is typically measured as the function of the wavenumber. The wavenumber is inversely proportional to the wavelength and is expressed with the unit cm^{-1} ^[105]. The

most commonly scanned wavenumbers are from 4000 to 400 cm^{-1} , which constitutes the region of most of the inorganic materials and organic functional groups absorb^[106]. Aside from the conventional IR spectroscopy measuring light transmitted through a sample, reflection IR spectroscopy is also possible using a combination of infrared spectroscopy with reflection theories^[106, 107].

It can be a beneficial mode for measurement of thin films^[108, 109]. Reflectance examination techniques refer to methods for obtaining an infrared spectrum by reflecting IR radiation from a solid (it can be liquid as well). There are three main types of reflectance technique: specular, diffuse, and reflection-absorption, as displayed in Figure 14^[110].

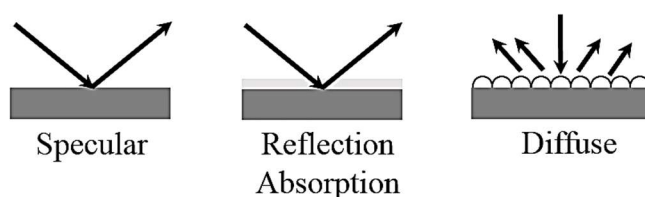


Figure 14: Reflectance types in FTIR spectroscopy.

Specular reflectance is applied to samples with smooth and polished surface, like electropolished steel substrates for deposition of thin films^[111]. The other two types diffuse reflectance, and reflection absorption applies for samples with somewhat rougher surfaces and IR-transparent films on opaque substrates, respectively^[112].

In this master project, reflection mode is used, and it is reflectance that occurs when an incident IR beam hits a smooth surface of a solid sample. The angle of reflectance is equal to the angle of incidence during the measurement. The way the measurement is set is schematically illustrated in Figure 15^[112].

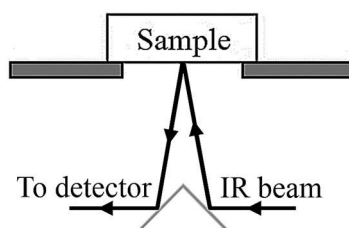


Figure 15: The optical illustration of a simple specular reflectance mount for an FTIR instrument.

This type of reflectance is based on using two flat mirrors and a platform with a hole inside. The sample is placed over that hole, while the background spectrum is obtained by placing a smooth reflecting surface of the sample.

2.3.6 X-ray photoelectron spectroscopy

An electron is referred to as photoelectron when it is ejected from the electron shell of an atom that is irradiated by photons such as x-rays^[113]. This is illustrated in Figure 16. An incoming photon may have enough energy ($h\nu$) to eject an inner-shell electron so that the ejected photoelectron has a kinetic energy (E_k)^[114]. By measuring the value of E_k , one can determine the binding energy (E_B) of the electron based on Equation 7.

$$E_B = h\nu - E_k - \Phi \quad (7)$$

where Φ is the energy required by the electron to be removed from the surface of the material, h is the Planck's constant, and the ν is the frequency of the light.

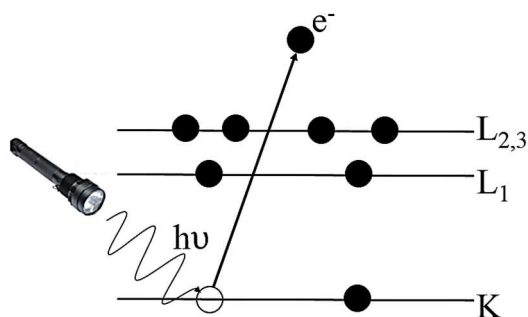


Figure 16: Schematic illustration of the photoemission process. The x-ray photons stick to the surface of a sample resulting in the emission of a 1s photoelectron^[115].

The value of Φ depends on the materials composition and the instrument. XPS is, therefore, a method for identifying chemical elements from the binding energy spectra of their electrons. Since the kinetic energy of these photoelectrons is very low, it is essential that the outgoing photoelectron is not disturbed before it reaches the detector^[116]. The ultrahigh vacuum is therefore required, usually on the order of about 10^{-12} mbar^[117].

2.3.7 Ultraviolet and visible light spectroscopy

Ultraviolet-visible spectroscopy (UV-Vis) is a technique that measures absorption or reflection in the ultraviolet and visible range^[112, 118]. When light interacts with a material, some of its energy may be absorbed, and thus increase the energy of that material. Typically, the total potential energy of such material mathematically expressed as the sum of its electronic, vibrational, and rotational energies, just as expressed in Equation 8^[119, 120].

$$E_{total} = E_{electronic} + E_{vibrational} + E_{rotational} \quad (8)$$

The amount of energy is quantified by the series of the discrete energy levels or states, while the difference in energy among the states is classified in the following order^[120].

$$E_{electronic} > E_{vibrational} > E_{rotational}$$

In terms of electronic energy levels, both the UV photons and the visible light have the possibility of initiating transitions internally. In organic molecules, the majority of absorptions occur in the UV area by the electrons that move into the antibonding orbital π^* like in Figure 17, where an example of electronic transitions in formaldehyde is presented^[120, 121].

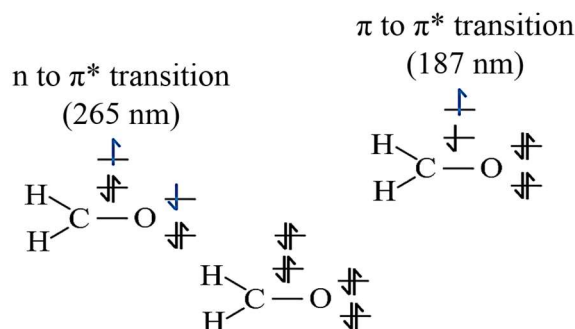


Figure 17: The electronic transition in formaldehyde^[121].

The molecules that contain a π bond are often called chromophores, and when inserted in a hydrocarbon, like in the example in Figure 17, a compound is produced with an absorption between 200 and 1000 nm. The generated absorbance band often confirms the resulting chromophore from the transitions at a particular wavelength^[122].

2.3.8 Atomic force microscopy

Atomic force microscopy (AFM) has been used for characterization of the topography of the deposited films. A cantilever with a tip is used to scan a surface, and the deflection of the tip is monitored and used to build a map of topography^[97, 123]. The deflection is registered as a change in position of a laser beam reflecting off the cantilever surface, as illustrated in Figure 18a) below^[97].

Two most important operational modes in AFM are contact mode and non-contact mode, presented in Figure 18b). The non-contact mode is used throughout this master project. The probe oscillates above the sample surface but does not touch the sample. The deflection is due to attraction from weaker van der Waals forces. The topography can be measured by using a feedback loop to monitor changes in the

amplitude due to attractive forces^[124]. Disadvantages of this mode are that it generally provides lower resolution than contact mode, but it is the best mode when it comes to avoiding damage on the probe and sample.

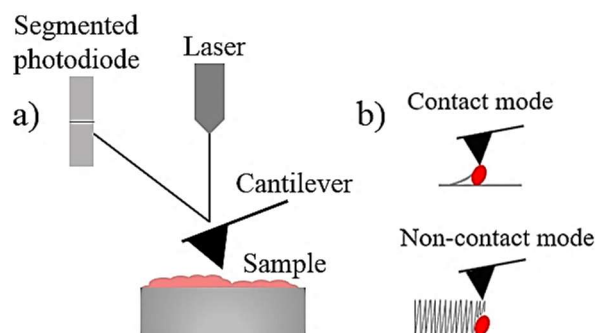


Figure 18: a) Schematic illustration of AFM and working principle. As a tip is scanned across the sample surface, topographical features cause a deflection of the cantilever. This deflection is registered as a change in the position of the reflected beam. The positional change is related to the magnitude of the cantilever deflection. b) The most important operational modes in AFM.

3 Experimental

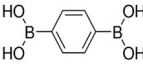
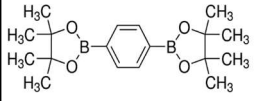
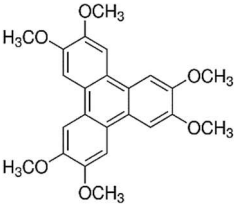
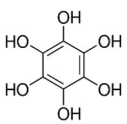
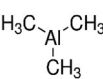
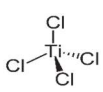
This chapter is mainly concerned with the description of the type of equipment and chemicals used for each of the techniques. The techniques used are also explained together with a brief description of experimental parameters.

3.1 Precursors

As mentioned, the precursor tester is an instrument developed at the Chemistry Department of the University of Oslo. A schematic overview of the setup is presented in Figure 8 (Page 16). An AT-cut 6 MHz QCM unit produced by Inficon and a microscope of the type DinoLite was used. The microscope is placed in a time-lapse mode where images are recorded every 30 seconds. During the experiment, a small amount of the precursor powder is placed in the aluminum-based sample holder that is directly connected to a thermocouple. The sample is gradually heated while DinoLite logs visual changes, and the Colnatec LTE registers possible deposition on the QCM unit. The heating rate was 1 °C per minute for BDBA, whereas the rate was 5 °C per minute for BDBA-BPE, HMTP, and BH.

Thermogravimetric analysis was used in combination with precursor tester in the determination of the sublimation temperatures. The analysis was employed on a Netzch 209 G1 Libra where temperature interval investigated was between 30 and 300 °C. For BDBA, the heating rate was 1 °C per minute, whereas the rate was 10 °C per minute for BDBA-BPE and HMTP. The precursors investigated with their state of aggregation and structure formulas are listed in Table 1.

Table 1: Precursors used in the present work with their state of aggregation, color, and structural formulas.

Precursor	Appearance	Structure	Purity	Producer	CAS
Benzene-1,4-diboronic acid (BDBA)	White powder		>98 %	Sigma Aldrich	4612-26-4
Benzene-1,4-diboronic acid bis (pinacol) ester (BDBA-BPE)	White powder		>98 %	Sigma Aldrich	99770-93-1
2,3,6,7,10,11-Hexamethoxy triphenylene (HMTP)	Purple powder		>98 %	Sigma Aldrich	808-57-1
1,2,3,4,5,6-Benzenehexol (BH)	Dark purple powder		>98 %	Sigma Aldrich	608-80-0
Trimethylaluminum (TMA)	Colorless liquid		>98 %	Sigma Aldrich	75-24-1
Titanium(IV)chloride (TiCl4)	Yellow liquid		<99 %	Sigma Aldrich	7550-45-0

3.2 Depositions

The MLD depositions were performed in a gas-phase reactor of the type F-120 (ASM Microchemistry Ltd). It is a hot-wall type of reactor with six precursor tubes divided into four temperature zones for the precursors. There are in total eight temperature zones. The temperatures of the different zones are set in such a manner that there is an increasing gradient from the first zone until the seventh zone, where the reaction chamber is located. This is to avoid any condensation of precursor along with its flow.

The N₂ flow (Praxair 500743 Nitrogen 5.0 Ultra) through the reaction chamber was kept at 300 sccm (standard cubic cm per minute), and the flow in the outer chamber was maintained at 100 sccm. A pump kept the pressure between 6 and 7 mbar throughout the experiments. A schematic illustration of the F-120 reactor is presented in Figure 19, showing where different types of precursors are located in the reactor and where the reaction chamber needs to be during depositions.

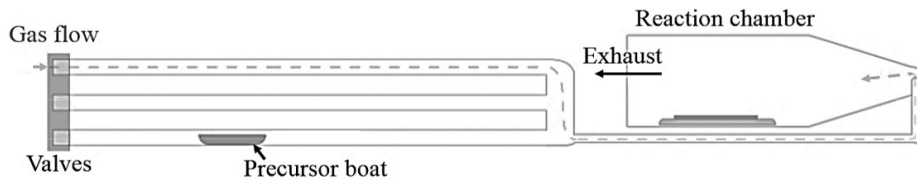


Figure 19: Vertical cross-section of the flow system in the F-120 reactor used in this work. The figure shows one of the two sets of the precursor chambers. Temperature increases from left to right. The gray precursor boat is in the precursor tube while the dashed gray arrow represents the nitrogen gas flow, and it goes from left to right.

Powder precursors are placed in precursor boats and precursor tubes and are heated to achieve sufficient vapor pressure. Precursors such as TMA and TiCl_4 that have adequate vapor pressure at room temperature are used as external precursors outside of the reactor. Vapors of such precursors are transferred to the reactor by a valve on the bubbler. The reaction chamber is a glass tube with separated inlets for the cation and anion type of precursors used. The diameter of the tube is 5.5 cm. During each deposition, either three or five substrates were placed on a glass plate on top of an aluminum plate. The glass plate with dimension $50 \times 76 \times 1 \text{ mm}^3$ is produced by Glaswarenfabrik Karl Hecht KG, while the aluminum plate is adapted to fit the reaction chamber. Before MLD, this glass plate is cleaned with ethanol. Figure 20 shows the orientation of the substrates in both cases and their names used later in Chapter 4.

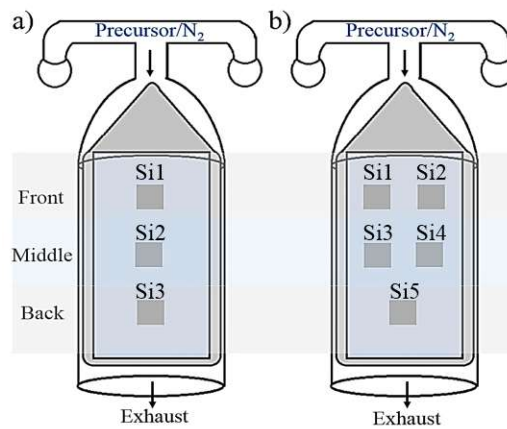


Figure 20: a) Illustration of a reaction chamber where three substrates are in front, middle and backside of the glass substrate marked with blue color b) Illustration of the reaction chamber where five substrates are used. Two in front, two in the middle and one in the back of the glass substrate. In some deposition only, Si(100) were used, but the combination of substrates mentioned in Table 2 was also used in some depositions.

3.3 Substrates

Generally, the substrates used in this thesis were the monocrystalline boron-doped silicon (100) $1 \times 1 \text{ cm}^2$ made from a larger silicon wafer. Wafers typically have a ca. 2 nm layer of a native SiO_2 on their surface. The thickness of the SiO_2 layer on the silicon substrate is nevertheless measured before every deposition by SE. Before doing MLD, the substrates are also cleaned using dry wipes and

blowgun. Table 2 gives an overview of substrates used and their dimensions as well as the type of measurements performed.

Table 2: Types of substrates used in during depositions with corresponding dimensions and overview of what type of measurement was done with each substrate.

Substrate type	Dimension	Type of measurement
Si(100)	1x1 cm ²	SE, GIXRD, XRR, AFM, XPS
Electropolished steel	1x1 cm ²	FTIR reflection mode
Si(100) etched backside	1x1 cm ²	FTIR transmission mode
Silica(001)	1x1 cm ²	UV-Vis
QCM unit	d = 25 mm	Growth rate experiments, FTIR reflection mode

3.4 Characterization of films

3.4.1 Spectroscopic ellipsometry

The type of ellipsometer used is Alpha SE J.A.Woollam Co (Figure 21). In combination with a computer software CompleteEase, thickness, and refractive index for all the films deposited on the Si(100) substrates were determined.



Figure 21: An image of the ellipsometer Alpha SE J.A.Woollam Co[88].

The instrument used wavelengths between 380 – 890 nm with an incidence angle of 70°. Measurements are typically performed within 15 minutes after deposition, but also after different times after deposition on three different places on the substrate to investigate for possible thickness gradients and stability in the air as a function of time. Thickness values, together with the refractive index for the middle part, are noted down. The acquired data are fitted with a mathematical model to determine the optical parameters. Throughout this master project, the Cauchy model was used as the standard adaptation. The refractive index is provided at $\lambda = 632.8$ nm.

3.4.2 Quartz crystal microbalance characterization

In-situ QCM characterization was done by using two AT-cut crystal 6 MHz with gold-electrodes. In the reaction chamber, these QCM units were separated by 5 cm and placed in a home-built holder, presented in Figure 22. Raw data are registered with a Maxtek data logger and the program LabView. The thickness monitor used is produced by Colnatec of the type EON-LT.

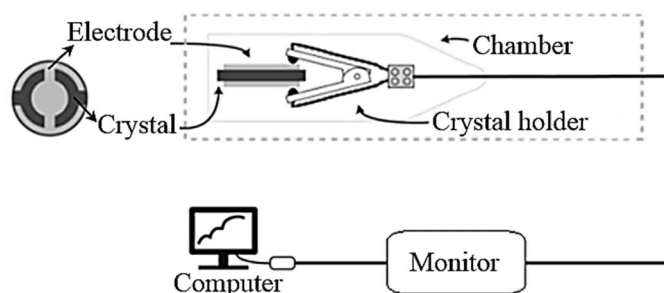


Figure 22: An illustration of a typical QCM characterization setup consisting of a reaction chamber that sits in the reactor, a thickness monitor, and a PC. Reaction chamber used for a QCM characterization setup consists of two QCM units separated by 5 cm from each other.

The first material system investigated by QCM was based on BDBA and HMTP. Along with the QCM response of this reaction, the response of the reaction between TMA and HMTP, BDBA and water were investigated, to compare the frequency slopes. Table 3 presents the different reactions tested during this experiment, the locations of the precursors and their sublimation temperature (RT stands for room temperature) in the reactor, along with the respective pulse and purge parameters. The TMA and water sequences were only performed with 30 cycles while 100 cycles were used for the rest. This experiment was done at 250 °C.

Table 3: Pulse and purge parameters for the QCM characterization for the material system based on precursors BDBA and HMTP. Other systems, like TMA+HMTP, TMA+BDBA, and reference TMA+H₂O, were investigated. The table presents the location of the precursors in the reactor during depositions as well as the duration of these depositions.

Systems	Precursor	Valve	Reactor location	Pulse (s)	Purge (s)	Number of cycles
TMA + H ₂ O	TMA	1	External (RT)	0.3	3	30
	H ₂ O	6	External (RT)	0.3	3	
BDBA + HMTP	BDBA	4	Zone 2 (150 °C)	15	5	100
	HMTP	2	Zone 4 (215 °C)	20	5	
TMA + HMTP	TMA	1	External (RT)	0.3	3	100
	HMTP	2	Zone 4 (215 °C)	15	5	
TMA + BDBA	TMA	1	External (RT)	0.3	3	100
	BDBA	4	Zone 2 (150 °C)	15	5	
TMA + H ₂ O	TMA	1	External (RT)	0.3	3	30
	H ₂ O	6	External (RT)	0.3	3	

The following QCM experiment (Table 4) was performed to investigate the reaction between TMA and HMTP further. It starts with a TMA and water sequence, then precursors TMA and HMTP individually to inspect the reactor for any CVD-type growth or technical issues and finish the experiment by performing the test of the TMA and HMTP. All of the tests were performed with 30 cycles. The deposition was done at 250 °C.

Table 4: Pulse and purge parameters for the QCM characterization for the system based on TMA and HMTP. Empty sequences with only TMA and only HMTP are investigated. A reference TMA+H₂O and TMA+HMTP are added to the end. The table presents the location of the precursors in the reactor during depositions as well as the duration of these depositions.

Systems	Precursor	Valve	Reactor location	Pulse (s)	Purge (s)	Number of cycles
TMA + H ₂ O	TMA	1	External (RT)	0.3	3	30
	H ₂ O	6	External (RT)	0.3	3	
Only TMA	TMA	1	External (RT)	0.3	3	30
	Empty					
Only HMTP	HMTP	4	Zone 2 (215 °C)	15	5	30
	Empty					
TMA + HMTP	TMA	1	External (RT)	0.3	3	30
	HMTP	4	Zone 2 (215 °C)	15	5	

Deposition parameters of the next QCM experiment investigating most optimal pulse and purge parameters for precursors TMA and BDBA are presented in Table 5. Deposition temperature was 200 °C, while the characterization starts with a standard pulse and purge lengths based on findings from the experiment described in Table 3. Starting with the test of TMA pulse, there are 7 different pulse lengths for TMA that are substituted with the standard value 0.4 s, which gives 7 different mini tests repeated 10 times. Further on, there are 6 different pulse lengths of BDBA that are substituted with 20 s, and in this way, the QCM experiment is built for all of the tests in the second column. When all of the possible combinations were done with 10 cycles, the same combinations were repeated 20 times as well.

Table 5: QCM experiment for a system based on TMA and BDBA, where we investigate the most optimal pulses and purges for each precursor. The table displays the duration of each of these pulse and purge tests.

Duration	Testing	Length (s)						
		0.6	0.5	0.4	0.3	0.2	0.1	0
10 cycles	TMA pulse	0.6	0.5	0.4	0.3	0.2	0.1	0
	BDBA pulse	45	15	5	2.5	1	0	
	BDBA purge	15	10	7.5	5	2	0.5	
	TMA purge	3	1	0.75	0.5	0.4	0.25	
20 cycles	TMA pulse	0.6	0.5	0.4	0.3	0.2	0.1	0
	BDBA pulse	45	15	5	2.5	1	0	
	BDBA purge	15	10	7.5	5	2	0.5	
	TMA purge	3	1	0.75	0.5	0.4	0.25	

The deposition parameters of the QCM experiment 200 °C for TiCl₄ and BDBA are presented in Table 6. The standard pulse and purge sequence, in this case, was 0.5s/1s/20s/8s.

Table 6: Investigation of the most optimal deposition parameters for a system based on TiCl₄ and BDBA via a QCM experiment. The table displays the duration of each of these pulse and purge tests.

Duration	Testing	Length (s)						
10 cycles	TiCl ₄ pulse	3.75	2	1	0.75	0.25	0	
	BDBA pulse	60	45	20	7.5	2.5	1	0
	BDBA purge	15	7.5	5	2.5	0.5		
	TiCl ₄ purge	3.5	1	0.75	0.5			
20 cycles	TiCl ₄ pulse	3.75	2	1	0.75	0.25	0	
	BDBA pulse	60	45	20	7.5	2.5	1	0
	BDBA purge	15	7.5	5	2.5	0.5		
	TiCl ₄ purge	3.5	1	0.75	0.5			

A QCM response experiment was also performed for the reaction between TMA and BDBA-BPE along with a reference TMA and water that were repeated ten times. The aim was to compare their frequency slopes and determine if a material system based on BDBA-BPE should be investigated further. Deposition parameters are presented in Table 7. Two other reactions were investigated by QCM. The first experiment tested reactions between BDBA and BH and the second TMA and BH. Like in the other QCM experiments, reference TMA and water sequences were added for comparison. Table 8 presents the deposition parameters of the QCM experiment.

Table 7: Standard pulse and purge sequence for the QCM characterization of the system based on TMA and BDBA-BPE. Pulses and purges tested for each precursor are also presented. The table presents the duration of these tests.

Systems	Precursor	Valve	Reactor location	Pulse (s)	Purge (s)	Number of cycles
TMA + H ₂ O	TMA	2	External (RT)	0.4	1	10
	H ₂ O	6	External (RT)	0.3	3	
TMA + BDBA-BPE	TMA	2	External (RT)	0.3	3	10
	BDBA-BPE	4	Zone 2 (80 °C)	60	5	

Table 8: Pulse and purge parameters of the QCM characterization when of the system based on precursors BDBA and BH. BDBA+BH and TMA+BH systems are also investigated together with the Reference sequences TMA+H₂O. The table presents the location of the precursors in the reactor during depositions as well as the duration of these depositions.

Systems	Precursor	Valve	Reactor location	Pulse (s)	Purge (s)	Number of cycles
TMA + H ₂ O	TMA	2	External (RT)	0.4	1	10
	H ₂ O	6	External (RT)	0.3	3	
BDBA + BH	BDBA	4	Zone 4 (150 °C)	20	8	10
	BH	3	Zone 2 (125 °C)	10	5	
TMA+ BH	TMA	2	External (RT)	0.5	1	10
	BH	3	Zone 2 (125 °C)	90	8	
TMA + H ₂ O	TMA	2	External (RT)	0.4	1	10
	H ₂ O	6	External (RT)	0.3	3	

Lastly, the investigation of the optimal pulse and purge parameters was done for TMA and BH (Figure 9). Due to limited amounts of BH precursor, the QCM experiment performed lasted much shorter than other QCM experiments. Deposition temperature was 200 °C, and the standard pulse and purge sequence was 0.4s/1s/40s/8s.

Table 9: Standard pulse and purge sequence for the QCM characterization of systems based on BH and BDBA and TMA and BH. Pulses and purges tested for each precursor are also presented. Each of the tests runs in 10 cycles.

Duration	Testing	Length (s)				
		10 cycles	TMA pulse	0.6	0.4	0.2
	BH pulse	70	20	7.5	1.5	0
	BH purge	15	7.5	3	1	
	TMA purge	2	1	0.5	0.1	

3.4.3 Fourier-transformed infrared spectroscopy

The chemical state of the deposited films was investigated using Vertex 70 FTIR spectrometer. As mentioned in Table 2, the substrates used for these measurements were the Si (100) substrates with etched backside in transmission mode and the electropolished steel substrates in the reflection mode. As also bands originating from these substrates can be seen in the measured spectra, subtraction of a clean Si (100) substrate and an uncoated electropolished steel substrate spectrum from the spectra for the samples was necessary. This was done automatically in the OPUS software used throughout these measurements.

3.4.4 Ultraviolet and visible range spectroscopy

Absorption spectroscopy was performed in the UV and visible range to determine the transmission for various films deposited in this work. It was also utilized for the identification of aromatic units in the films. The UV-vis spectrometer is based on a light source, sample holder, and a detector. A simple sketch of the setup is presented in Figure 23.

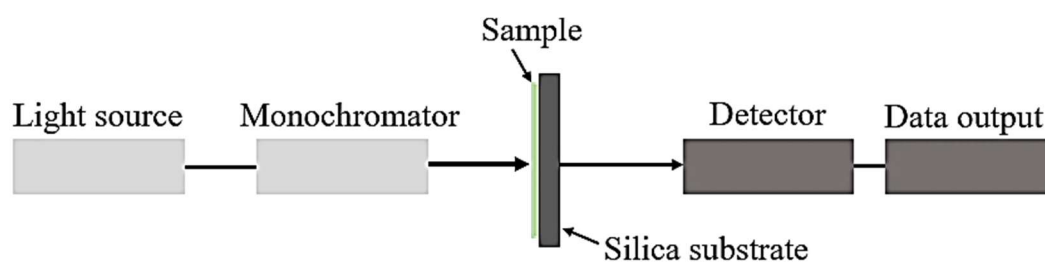


Figure 23: Schematic illustration of the UV-vis measurement setup consisting of a light source, sample, detector, and a computer to analyze the data.

The light source in the schematic is a DH-2000 UV-VIS-NIR Light source from Mikropack, while for the detection of the signals the Ocean optics Inc fiber optic spectrometer was used USB2000+. Region of detection is 200-900 nm. Data analysis was performed on a PC software called OOIBase32 v2.0.

3.4.5 Diffraction techniques

All of the film deposited in this work were characterized by GIXRD and XRR. These measurements were carried out on PANalytical Empyrean. The instrument utilizes Cu K α irradiation source that is driven by 45kV/40mA ($\lambda = 1.5406 \text{ \AA}$), a parallel wave (x-ray mirror) and a proportional point detector (PW 3011/20). GIXRD is a method that uses a relatively low incident angle for the x-rays, so they reflect more from the surface of the film and less from the substrate. An incidence angle of 0.3° was used in this study, and the range for 2θ was typically $0 - 40^\circ$, sometimes even $0 - 70^\circ$. The data is used to determine the crystallinity and composition of thin films or if the film is amorphous.

For XRR measurements, the angle of incidence was fixed at 0.3° , and the 2θ was scanned from $0.08^\circ - 6^\circ$. The X'Pert Reflectivity program was used for thin film thickness analysis where data fitting is performed by considering different material layers.

3.4.6 Atomic force microscopy

For AFM imaging, a Park Systems XE-70 microscope was used. The whole instrument is located in an anechoic box to reduce background vibrations, and samples are placed onto an anti-vibration holder. The experiments were performed in non-contact mode using a noncontact high-resolution tip from Park Systems. The AFM is controlled by XEP software, and data processing was performed using Gwyddion.

3.4.7 X-ray photoelectron spectroscopy

Analysis of the chemical composition was done by XPS. The experiments were carried out at MiNaLab using a Thermo Scientific Theta Probe Angle-Resolved Photoelectron Spectrometer. The instrument is equipped with an ultrahigh vacuum stage, where both the sample and x-ray source Al K α -anode are located. Pass energy used for the general survey scans was set to 100 eV and 60 eV for the high-resolution scans. Data analysis was done by Casa XPS. The measurements were performed by Kristian Weiby. Substrates involved with XPS analysis in this work were the Si(100) but also the glass plates supporting them under depositions (Figure 20).

3.5 Material systems investigated

The overview of the different material systems and deposition conditions such as temperature and the pulse and purge parameters are given in Table 10.

Table 10: Pulse and purge parameters for the precursors used in this master thesis.

Structure	Material	Deposition temperature	Valve	Reactor location	Pulse (s)	Purge (s)
Organic	BDBA	200 °C	4	Zone 2 (150 °C)	20	5
Organic	BDBA + HMTP	250 °C	4	Zone 2 (150 °C)	15	5
			1	Zone 4 (215 °C)	15	5
Hybrid	TMA + BDBA	180 – 340 °C	2	External (RT)	0.4	1
			4	Zone 2 (150 °C)	20	8
Hybrid	TMA + BDBA-BPE	200 °C	2	External (RT)	0.4	1
			4	Zone 2 (150 °C)	60	8
Hybrid	TiCl ₄ + BDBA	200 -300 °C	2	External (RT)	0.5	1
			4	Zone 4 (215 °C)	40	8
Organic	BH + BDBA	200 °C	2	Zone 2 (150 °C)	20	8
			4	Zone 4 (215 °C)	10	5
Hybrid	TMA + BH	200 °C	2	External (RT)	0.4	1
			4	Zone 2 (150 °C)	90	8

4 Results

In this chapter, the results from the experiments described in Chapter 3 are presented. This includes the investigation of the thermal properties of the precursors, the test depositions, and the results of the characterization techniques used.

4.1 Precursors and their thermal properties

Before material synthesis and characterization, the thermal stability of the precursors was analyzed using TGA (Chapter 2.3) and the precursor tester (Chapter 2.2). TGA (Figure 24) shows the mass losses as functions of the temperature in an interval between 30 and 300 °C for BDBA, HMTP, and BDBA-BPE. For BDBA, the heating was done at a rate of 1 °C per minute, whereas the rate was 10 °C per minute for BDBA-BPE and HMTP.

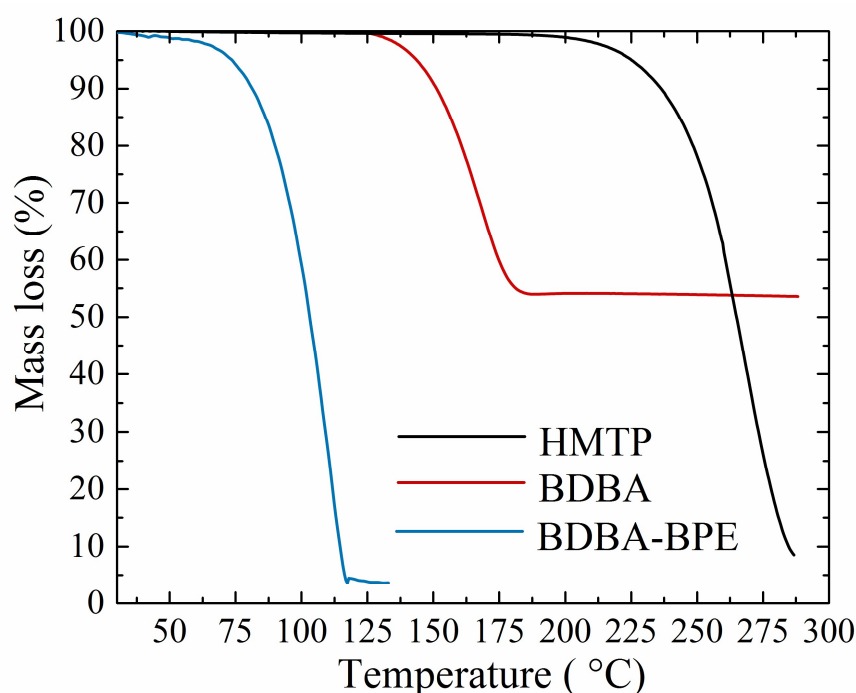


Figure 24: TGA used to determine the sublimation temperatures for BDBA-BPE (blue), BDBA (red) and HMTP (black). Mass loss is plotted as a function of temperature between 30 to 300 °C, with heating rates of 1 °C/min for BDBA and 10 °C/min for BDBA-BPE and HMTP.

As seen in Figure 24, all three compounds exhibit different thermal behavior. BDBA-BPE seems to sublimate at 75 °C and is neither decomposing nor having any residual mass. For BDBA, even though there is a residual mass of about 55% at higher temperatures, the curve shows sublimation with an onset at around 140 °C. The remaining mass could be an indication of a possible decomposition or polymerization. HMTP sublimes at a much higher temperature, at around 200 °C having a residual

mass of between 5 and 10% after the experiment. Figure 25 shows the change in the resonance frequency of the quartz crystal as a function of temperature for respectively BDBA-BPE, BH, HMTP, and BDBA. The heat rate for the latter was 1 °C/min, while the rest used a rate of 5 °C/min.

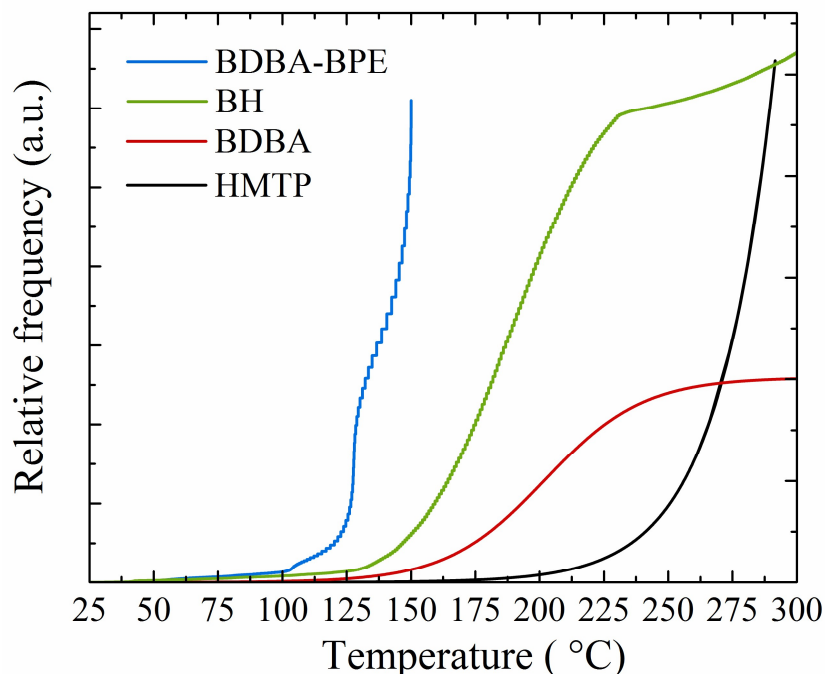


Figure 25: Frequency changes of the quartz crystal used to investigate the thermal stability for BDBA-BPE (blue), BH (green), BDBA (red) and HMTP (black) as functions of the temperature of the sample. The change in relative frequency is reversely proportional to mass deposited on the quartz crystal. The heating rate for BDBA-BPE, BH, and HMTP was 5 °C/min whereas for BDBA it was 1 °C/min.

BDBA shows a change in frequency due to the mass increase of the quartz crystal indicating sublimation at ca. 130 °C and a deflection of the curve at higher temperatures. Similar deflection is observed for BH, but the compound sublimates at a lower temperature, at around 125 °C. The two remaining precursors, BDBA-BPE and HMTP, sublime at 80 and 200 °C respectively but exhibit no deflection of the curve at higher temperatures. This corresponds well with the low residual mass observed from TGA done for these precursors.

An alternative approach to judge the applicability of the precursors is to visually observe how the precursors change with temperature using in-situ time-lapse photography during the process. All of the images on the left in Figure 26 marked a) illustrate the situation just before the sublimation starts, as compared to the images in the middle Figure 26b) taken 30 seconds later. On the right side, the structural formulas of the precursors are presented along with the temperature at which images marked a) were recorded.

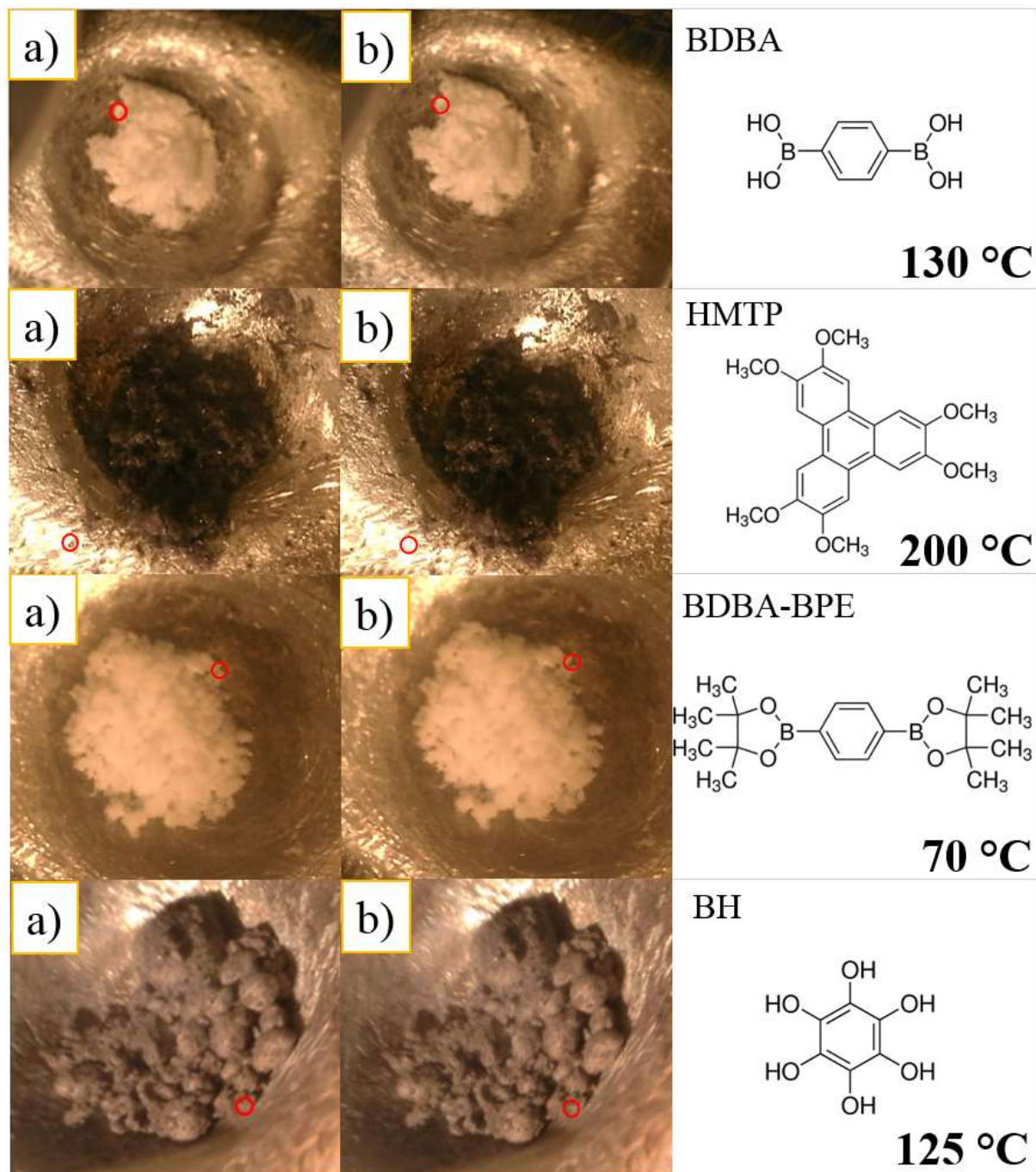


Figure 26: Evidence of the first visible changes occurring for all of the four organic precursors marked with red circles. Images a) were taken 30 seconds before images b). The temperatures at which images a) were taken are displayed under the structural formulas of all of the precursors located on the right side of this figure. The heating rate for BDBA was 1 °C/min while the heating rates for the rest of the precursors was 5 °C/min in a temperature range from 30 to 300 °C.

The first frequency change for BH occurs at around 125 °C, which corresponds well with the result obtained from the precursor tester (Figure 25). The shift in color started at the edges of the sample, and a minimal sample loss was observed. The temperature at which the holder is empty is around 225 °C, which explains the sudden frequency change for BH we observe in Figure 25. The sample holder becomes gradually empty for BDBA-BPE at around 90 °C, which is documented by the rapid frequency increase in Figure 25.

Additionally, BH sublimation was confirmed using the crystal unit from precursor tester and was analyzed with FTIR reflectometry (Figure 27). If the removal of the content of BH were due to sublimation, specific peaks defining the various bonds in the BH molecule would show up in the reflectometry spectrum. The indexed areas represent the most notable stretches. The ones occurring between 3340 and 3400 cm^{-1} are attributed to the O-H bond^[125], while the large distinctive reflection feature at around 1600 cm^{-1} corresponds to the C=C stretching mode of the aromatic ring^[125]. The small stretch at 1531 cm^{-1} corresponds to aromatic C-C stretch^[126]. All of the stretching vibrations do match well the structure of BH molecules^[109].

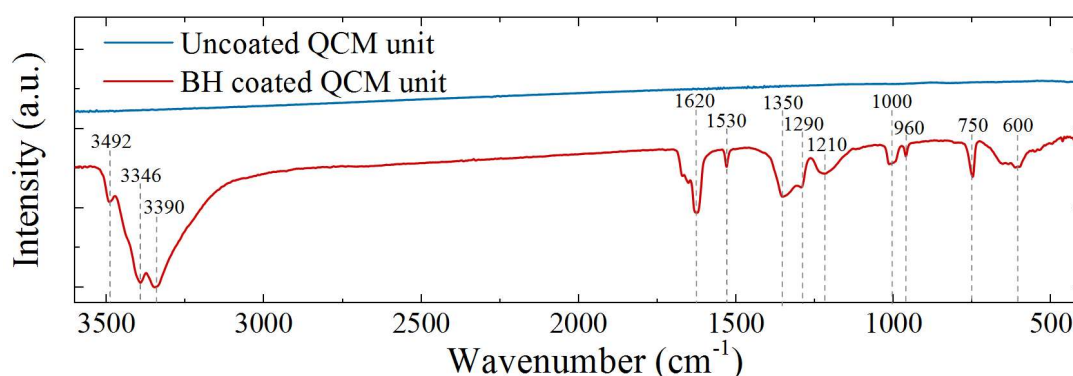


Figure 27: The full FTIR reflectometry spectra of the QCM unit used in the precursor tester for determination of sublimation temperature of BH (red) and the reflectometry spectrum for an uncoated QCM unit (blue). Dashed gray lines indicate the most notable peaks of the coated crystal unit.

Based on the results from the TGA, precursor tester and the FTIR reflectometry sublimation temperatures for BDBA, HMTP, BDBA-BPE, and BH was set to be 130 °C, 200 °C, and 80 °C, 125 °C, respectively. For BDBA and HMTP this appeared not to be optimal temperatures as the recrystallization of precursors (indicating the suitable flow of precursor into the reaction chamber) was not observed in the precursor tube in the reactor. Test depositions with these precursors were done increasing the deposition temperatures by 5 °C for every deposition until 150 °C for BDBA and 215 °C for HMTP, where acceptable recrystallization was observed for both precursors.

4.2 The reaction of BDBA with itself

The initial idea was to synthesize thin films of the COF-1 structure (Figure 5a). Reacting BDBA with itself in the ALD reactor requiring a minimum of two precursors (Chapter 2.1, Page 12) would mean that we want to obtain COF-1 in a CVD growth process. The deposition program written beforehand had to, therefore, contain another “precursor” to satisfy the operating conditions of the ALD reactor. 20s/5s was used as the pulse and purge lengths for BDBA while 0.3s/1s were used for the empty valve in the reactor. The result of this deposition using 100 cycles at 200 °C is displayed in Table 11. This pulse and purge lengths for BDBA were proposed based on the previous experience with ALD in our group.

Table 11: Thickness before and after using BDBA as a single precursor in the reactor to grow COF-1 thin films. Ellipsometry measurement was done right after the deposition. The positions of the substrates Si1, Si2, and Si3 in the reactor chamber is illustrated in Figure 20a)

BDBA with itself	Thickness (nm) (The standard deviation: 0.0394 nm)		
Substrate number	Si1	Si2	Si3
Before deposition	2.31	2.36	4.86
After deposition	3.42	3.38	4.48

Assuming enough BDBA is supplied through the reactor and the fact that we observe no film growth on any of the substrates may indicate that this type of reaction is too slow for it to occur on the silicon substrates.

4.3 The BDBA and HMTP system

Additional efforts were made to grow thin films of the COF-5 structure using BDBA and HMTP. Table 12 gives an overview of measured thicknesses before and after the deposition of films with BDBA and HMTP using 100 cycles at 250 °C. The pulse and purge sequence used in this deposition was 15s/5s/15s/5s starting first with the pulsing of BDBA. The pulse and purge sequence are only proposed values based on our experience in the research group, as more detailed characterization is required to estimate optimal pulse and purge lengths if there is a reaction between these two precursors.

Table 12: Thickness measured before and after deposition of BDBA and HMTP attempting to grow COF-5. Deposition temperature is 250 °C. The positions of the substrates Si1, Si2, and Si3 in the reactor chamber are illustrated in Figure 20a)

BDBA and HMTP	Thickness (nm) (The standard deviation: 0.0394 nm)		
Substrate number	Si1	Si2	Si3
Before deposition	3.16	2.9	2.58
After deposition	2.96	2.81	4.72

According to Table 12, the added thickness on the third substrate Si3 being closest to the exhaust was measured to around 2 nm, after subtracting the thickness of the silicon substrate before deposition. This indicates a possible reaction between BDBA and HMTP on the surface of the substrate. The possibility that a reaction occurs here is, however, questionable since only the last substrate appeared to have changed, and almost insignificantly. A QCM response test could help determine if the acquired film comes from a reaction between BDBA and HMTP.

Two QCM units marked in Figures 28 as A and B were used for this experiment. The experiment was done at the same temperature as the initial deposition, while the parameters used are described in Table 4. In addition to the reaction between BDBA and HMTP, QCM responses for the reactions between TMA and HMTP and BDBA were investigated to identify possible growth systems. The reaction between TMA and water was used as a reference. Focusing on the sequence containing BDBA and HMTP, Figure 28 shows no significant growth, as there is almost no frequency increase. However, the sequence with TMA and HMTP shows sign of possible growth, so further QCM analysis was performed to verify these observations.

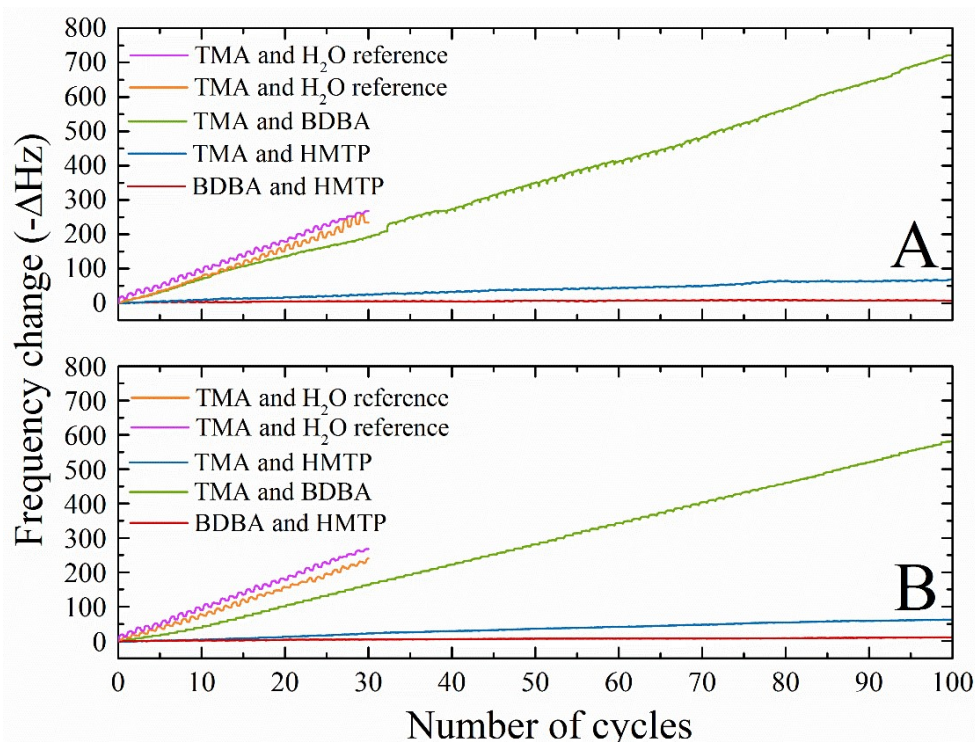


Figure 28: QCM response for various combinations of reactants to identify possible growth systems. A reference TMA and water sequence were added at the start (magenta) and the end (orange) of the experiment. These were repeated 30 times. Reactions between BDBA and HMTP (red), TMA and HMTP (blue) and TMA and BDBA (green) were done 100 times. The locations of the QCM units in the reaction chamber during the characterization are marked A (front) and B (back).

An additional QCM characterization was done introducing TMA and HMTP individually to the reaction chamber to inspect if any of the signals could be due to CVD growth or faults with the reactor. The pulse and purge parameters of this experiment are described in Table 5, while the results are displayed in Figure 29.

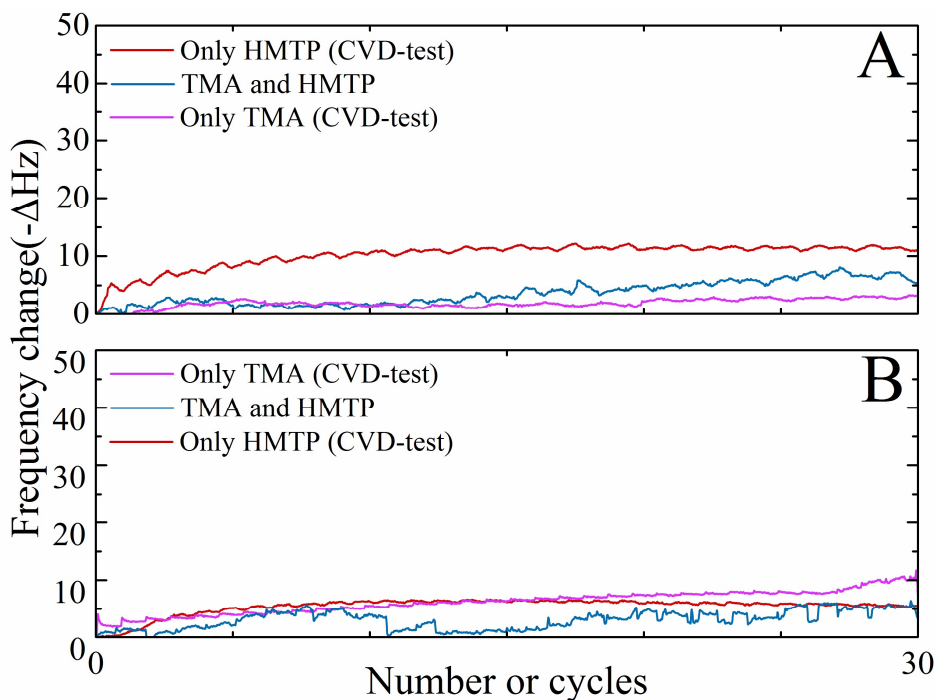


Figure 29: A QCM experiment consisting of a CVD-growth test with a single precursor HMTP (red), a test of the reaction between TMA and HMTP (blue) and another CVD-growth test with TMA (magenta). The experiment was conducted at 225 °C, while other deposition parameters are described in Table 5.

The frequency changes for all of the tests are below 10Hz, indicating no growth. The order of magnitudes of the frequency curves for the TMA and HMTP sequences are nearly the same, standing at around 60 Hz after 100 cycles in Figure 28 and around 11 Hz after 30 cycles in Figure 29. The results from Figure 28 and 29 verifies, therefore, no MLD growth of film based on the BDBA and HMTP. On a similar note, there is no significant MLD growth of films based on TMA and HMTP, as displayed in Figure 29. The material system based on TMA and BDBA shows quite a stable film growth, which is something that needs to be investigated further (Chapter 4.4). The growth rate appears very similar to the TMA, and H₂O references, so more dedicated techniques are necessary to differentiate between these two reactions.

One such technique is XPS analysis for detection of boron in the sample from a test deposition presented in Table 12. A general overview of the concentrations of each of the element found on the surface is obtained (Figure 30). The relative atomic percentages of these areas, but also the location of these expressed in eV are displayed in Table 13.

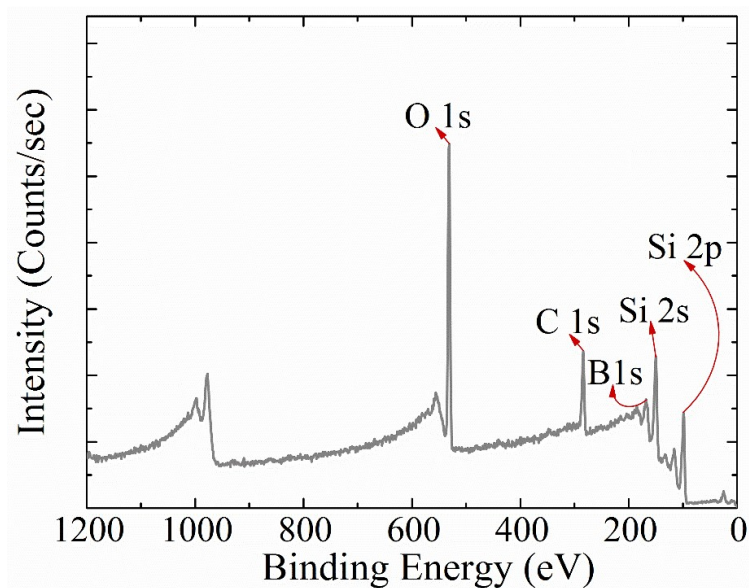


Figure 30: The general survey XPS scan with only B 1s, O 1s, and C 1s signals being resolved. High-resolution scans around these were also performed.

Table 13: Overview of the content of the sample with BDBA and HMTP in the three different areas of the survey scan.

Name	Peak (eV)	FWHM (eV)	Area (CPS vs. eV)	Atomic %
O1s Scan A	531	4.2	3247.7	29.7
C1s Scan A	284	4.6	994.1	26.7
B1s Scan A	185	0.9	14.8	0.8

The full survey-scan spectrum of the BDBA and HMTP film has prominent O 1s at 531 eV and a C 1s signal at 284 eV. The scan also confirms an almost insignificant content of boron in the film ca. (0.8 %, Table 13), which may originate from the silicon substrate itself.

4.4 The TMA and BDBA system

A vital prerequisite with the MLD technique is the self-limiting growth between the precursors and the functional groups on the surface of the substrates. A QCM characterization was therefore performed to investigate growth rate as a function of various pulse and purge lengths. The parameters of a proposed standard pulse and purge sequence 0.4s/1s/20s/8s (either pulse or purge) were changed one parameter at the time, while the others were kept constant. The deposition temperature was 200 °C. The results are presented in Figure 31. It seems that a 0.4 s long TMA pulse results in saturation of the surface. No decrease of mass occurs with the following purge step of TMA. This pulse length of 0.4 s was therefore chosen as a standard and 1 s as a standard purge length. BDBA, on the other hand, uses more than 20 s to obtain saturation. 20 s is therefore attempted as a standard pulse length, while a longer purge for BDBA may be required and was in this case eventually chosen to be 8 s.

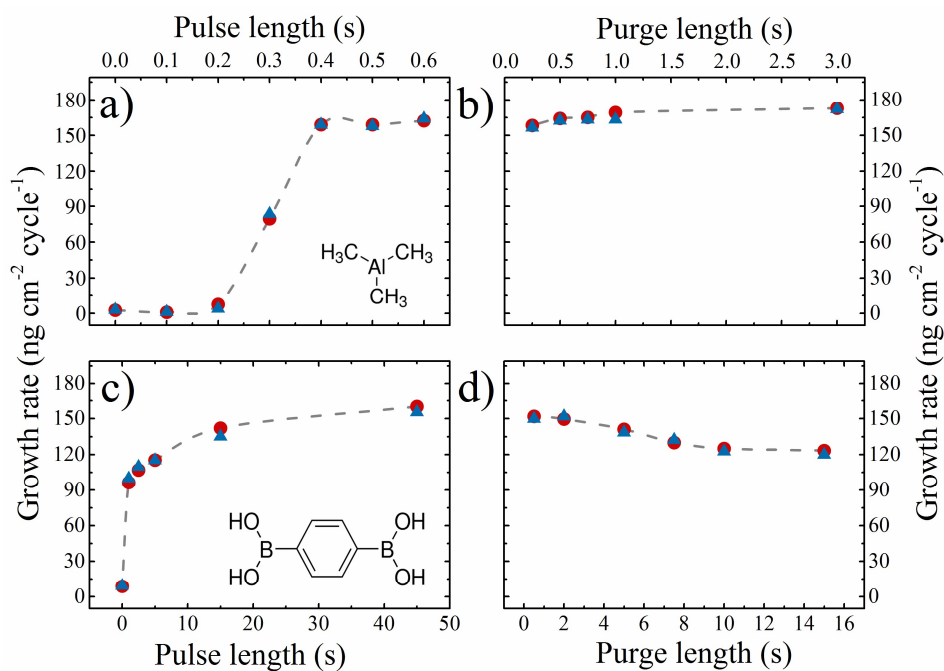


Figure 31: The growth rate of the hybrid TMA and BDBA system as a function of a) TMA pulse b) TMA purge c) BDBA pulse and d) BDBA purge as measured by QCM. Two QCM units were used, placed approximately 5 cm apart, one positioned in the front of the reaction chamber (blue triangles) and one in the back (red circles).

In contrast to the investigation of the growth rate as a function of pulse and purge lengths done in Figure 31, Figure 32 shows the mass increase as a function of time of two whole cycles.

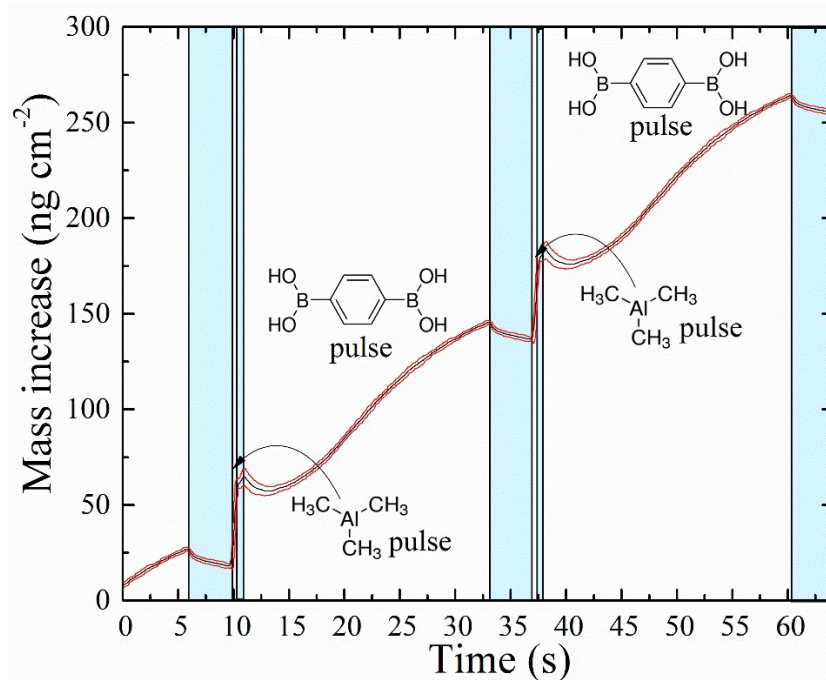


Figure 32: QCM measurement for hybrid TMA and BDBA system using pulse and purge sequence 0.4s/1s/20s/8s. The experiment was done at 200 °C, while the figure shows the mass increase (and loss) as the precursors TMA and BDBA are pulsed and purged. The red line shows the standard deviations of the QCM data, while the cyan areas indicate purging.

The two cycles represent the statistical average over 20 consecutive cycles along with their standard deviation (red). From Figure 32, we can see that the deposition has an ALD-type growth with the pulsing of TMA. The same saturated mass increase is not the case with the BDBA pulse, which may be due to the size of BDBA. There is almost no mass loss during TMA purge, while some mass is lost with the BDBA purge.

The pulse and purge sequence after these QCM experiments was set to be 0.4s/1s/20s/8s. Using these pulse and purge lengths, the growth rate of the system was investigated at different temperatures. SE was used to measure thicknesses of films of TMA and BDBA immediately after each deposition. The values measured were used to plot the growth rate as a function of deposition temperatures. The result of this experiment is displayed in Figure 33. All of the depositions were performed with 100 cycles in a temperature interval between 180 and 340 °C. The growth rate is relatively stable from around 1.6 Å/cycle at 180 °C to 1.3 Å/cycle at 240 °C. At the same time, the refractive index decreases as the deposition temperatures increases. Deposition at a higher temperature, starting above 280 °C leads to a possible second MLD-window. As seen in Figure 33, it starts from 280 to 340 °C with a growth rate at around 0.6 Å/cycle.

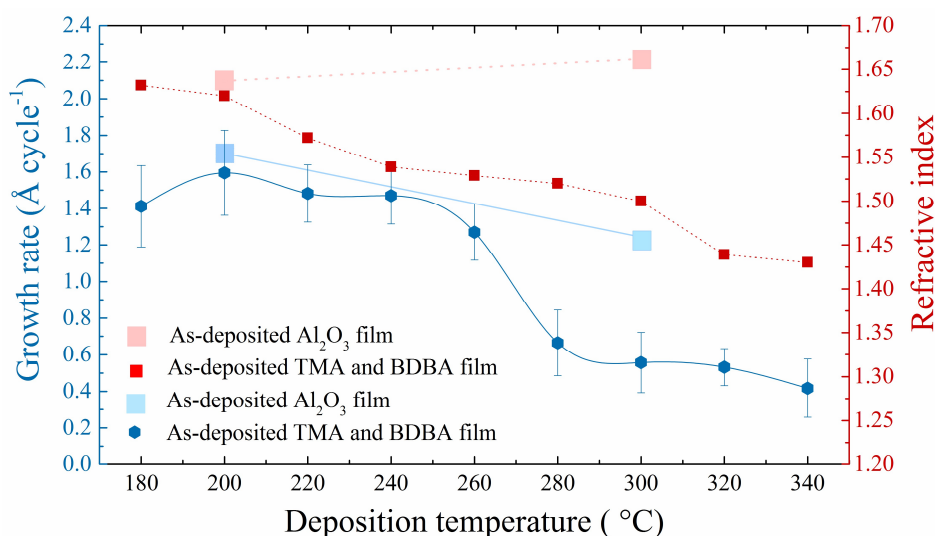


Figure 33: Growth rate (blue) and the refractive index (red) of the hybrid TMA and BDBA system as a function of deposition temperatures. The growth rates and refractive indices of Al₂O₃ films deposited at both 200 and 300 °C were added for comparison.

The highest growth rate based on Figure 33 occurs at 200 °C, the same temperature used for the QCM characterization of the TMA and BDBA system (within the first proposed MLD-window). Based on these findings, we kept the deposition temperature of 200 °C as standard temperature for producing samples for materials characterization. Films of TMA and BDBA were also deposited at 300 °C, to investigate the properties within the possible second narrow MLD window. The growth rates and refractive indices of Al₂O₃ films deposited at both 200 and 300 °C were added to Figure 33

for comparison. The growth rate of Al₂O₃ films slightly decreases with deposition temperature according to the figure, while the refractive index increases with increasing temperature. All the TMA and BDBA films presented in Figure 33 were investigated for their stability in air. This was done by monitoring the thickness of the films at different times after deposition. The films thickness is measured with SE first as deposited and then at different periods after depositions. The thickness of the films varies on the front, middle, and back substrates in the reaction chamber and the mean values based on these three thicknesses are presented in Figure 34.

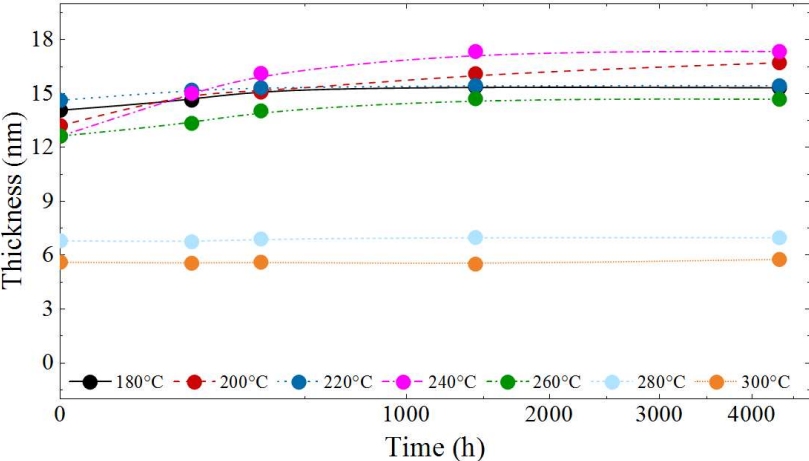


Figure 34: Air stability experiment investigating thickness as a function of time with a square root dependency on the time scale for samples deposited in a temperature interval between 180 and 300 °C.

There is an apparent increase in thickness in the beginning until about 1500h for all films deposited below 280 °C. There was no difference in film thickness for films deposited above 300 °C. Frequently, hybrid MLD films are seen to react with moisture due to unreacted precursors or even weak bond between the metal and the functional group from the organic linker or the metal to oxygen bond. The sensitivity to humidity was also tested on one of these TMA and BDBA films deposited at 200 °C using 100 cycles (represented by the red circle in Figure 34). Putting a drop of water on one of the substrates and then removing shortly after by absorbing it into a Kleenex tissue seemed not to cause any change in thickness. The following Table 14 presents the result of the experiment.

Table 14: Measured thickness of the film deposited at 200 °C right after deposition and after water treatments (VP3126). The standard deviation for the thickness values is 0.0394 nm.

Time	As deposited	Right after the water drop	24h after the water drop	3 months after the water drop
Thickness	18.51nm	18.67 nm	18.59 nm	18.74 nm

The crystallinity of the films from both predicted MLD-windows was investigated by GIXRD. The as deposited films at both 200 °C (700 cycles, ca. 90 nm) and 300 °C (1500 cycles, ca. 100 nm) show amorphous character, most likely due to their hybrid nature. Two thicker Al₂O₃ deposited at both

temperatures for purposes of comparing their GIXRD data are included in Figure 35a) together with GIXRD data for the films deposited with TMA and BDBA. All four of the measurements were done in the 2θ region between 2 - 40°. The thicknesses of the Al_2O_3 film were around 150 and 220 nm respectively. An XRR measurement is also performed in combination with an AFM analysis of the TMA and BDBA films deposited at both 200 and 300 °C, and the results are shown in Figure 35b) and c), respectively.

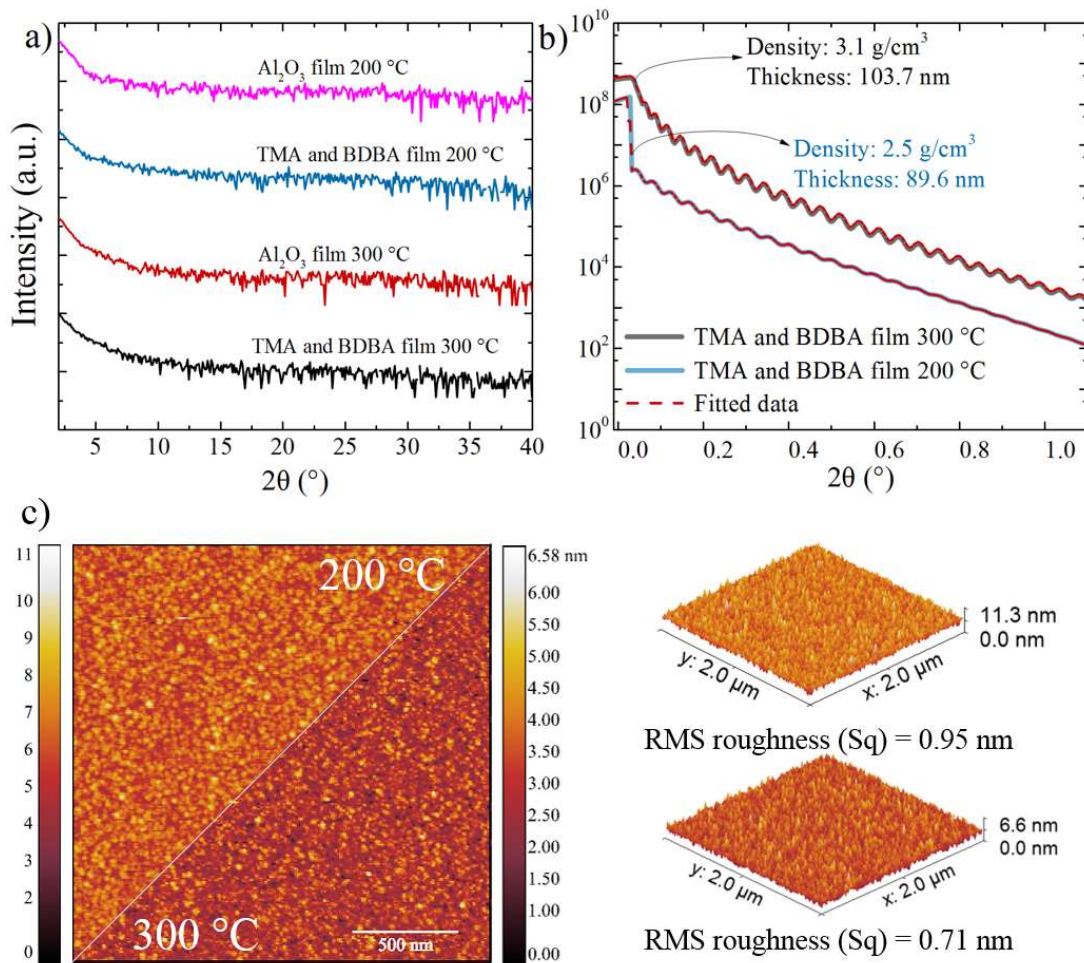


Figure 35: a) Diffractogram of four as deposited samples, including a ca. 150 nm Al_2O_3 film deposited at 200 °C (magenta), a ca. 100 nm TMA and BDBA film at 300 °C (black), a ca. 90 nm TMA and BDBA film deposited at 200 °C (blue) and a ca. 200 nm Al_2O_3 film deposited at 300 °C (red). b) XRR patterns of TMA and BDBA films deposited at 300 °C (black), 200 °C (blue) with data fitting (red). c) AFM analysis of the TMA and BDBA films deposited at 200 °C in 700 cycles and 300 °C in 1500 cycles. Image area in each panel is 2 x 2 μm² as seen in 3D images on the right side.

Simulation of the XRR pattern for the sample deposited at 200 °C produced a good fit with the measurement and revealed film density of around 2.5 g/cm³. For the sample deposited at 300 °C, the density was fitted to 3.1 g/cm³. The higher density of this sample corresponds well with the lower growth rate value shown in Figure 33 for the sample deposited at around 300 °C. The surface roughness was measured with AFM in non-contact mode and showed a decrease of root mean square

(RMS) roughness with increasing temperature. RMS roughness the film deposited at 200 °C is 0.95 nm while the film deposited at 300 °C is 0.71 nm. Such low values and smoothness are typical for amorphous materials.

The chemical bonding of the same samples was investigated by UV-Vis transmission spectroscopy. Figure 36 presents the transmittance of a roughly 100 nm thick hybrid sample deposited at 300 °C (red) and approximately 60 nm thick film deposited at 200 °C (blue). The black curve illustrates the background, which in this case was an uncoated silica crystal used for comparison with the two others as deposited. In addition, transmission spectra of thicker Al₂O₃ films deposited at 200 °C (dark blue, 220 nm) and 300°C (magenta, 150 nm) are added to Figure 36.

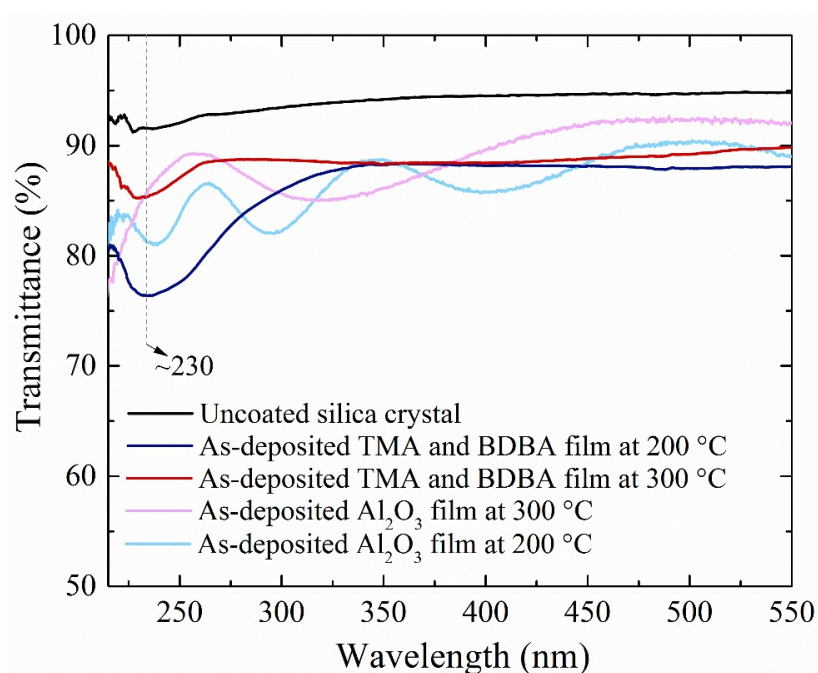


Figure 36: UV-Vis spectrum of an uncoated silica substrate (black), a ca. 80 nm thick hybrid TMA and BDBA film deposited at 200 °C (dark blue), a ca. 90 nm hybrid TMA and BDBA film deposited at 300 °C (red) and a ca. 145 nm thick Al₂O₃ film deposited at 300°C (sky blue). Finally, a ca. 290 nm thick Al₂O₃ film deposited at 200 °C (light purple).

Figure 36 shows a clear difference between the two sets of samples. The first set of films deposited with TMA and BDBA at 200 and 300 °C show signs of absorbance between 230 and 250 nm. The absorbance is slightly higher for the sample deposited at 200 °C. This could indicate the presence of aromatic bonds, or the presence of a benzene ring originating from the BDBA structure. This may also be the case for the sample deposited at 300 °C. The second set of much thicker Al₂O₃ films show seemingly high transmittance with oscillating interference patterns that may originate from the thickness of the film.

FTIR in reflection mode was also used to identify differences between the Al_2O_3 film and the films deposited with TMA and BDBA. Figure 37 displays the reflectometry results of four samples: An Al_2O_3 film deposited at 300 °C using pulse and purge sequence 0.4s/1s/0.3s/3s of TMA and H_2O , a TMA and BDBA film deposited at both 200 and 300 °C using the standard pulse and purge sequence. The fourth sample is an Al_2O_3 film deposited at 200 °C using pulse and purge sequence 0.4s/1s/0.3s/3s.

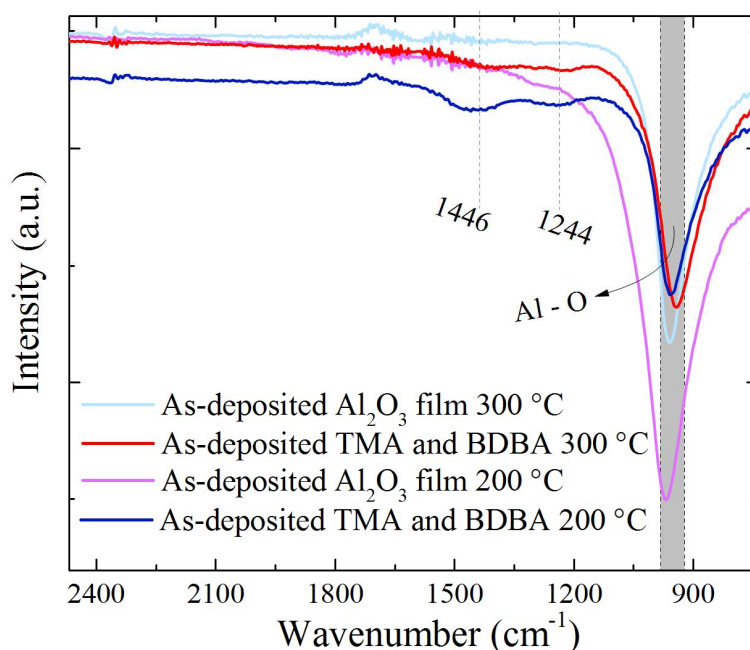


Figure 37: Spectra obtained after FTIR measurement in reflection mode. A ca. 145 nm thick Al_2O_3 film deposited at 300 °C (sky blue), a ca. 100 nm thick hybrid TMA and BDBA film deposited at 300 °C (red), a ca. 90 nm thick hybrid TMA and BDBA film deposited at 200 °C (light purple) and a 290 nm thick Al_2O_3 film deposited at 200 °C (dark blue). Indexed areas in the figure represent the area display the most eminent reflection.

The most significant difference between the films with Al_2O_3 and those with BDBA is two peaks located at 1446 and 1244 cm^{-1} . These occur only for the film deposited at 200 °C (most optimal growth temperature as seen in Figure 33) and may correspond to C-C stretch in the aromatic ring and the B-O or C-H bonds respectively. The reflectometry curve for the TMA and BDBA film deposited at 300 °C contain much less of these vibrations, but it is still not identical to the reflectometry curve of Al_2O_3 film deposited at the same temperature. In all four samples, the high-intensity dip of reflection or the stretch between 940 and 960 cm^{-1} is most probably from the Al-O bond. However, the stretches for TMA and BDBA films in this area are slightly shifted to the right.

An overview of the concentrations of each of the element found on the surface of the film deposited at 200 °C was obtained using XPS. The film was deposited using 0.4s/1s/20s/8s as pulse and purge parameters. The general survey scan is presented along with high-resolution spectra from the regions

of interest in Figure 38. The relative atomic percentages of these regions and the location the peaks expressed in eV are displayed in Table 15.

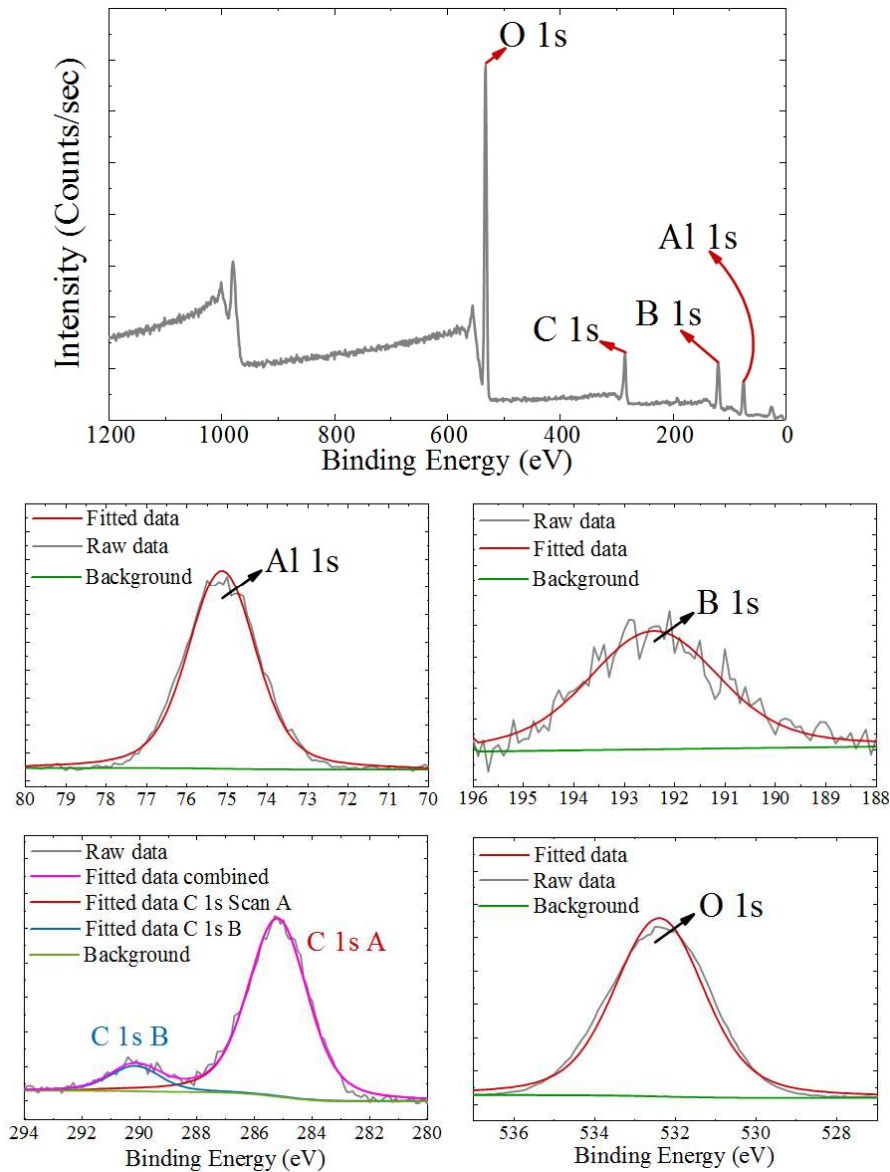


Figure 38: A general survey scan of the sample deposited using TMA and BDBA 200 °C (top). Together with the survey scan, high-resolution scans around B 1s, O 1s, C 1s, and Al 1s signals are resolved and presented on the right side with peak fitting performed for each of the signals (down). The green line under the raw data and the peak fitting represents the background.

Table 15: Overview of the contents of the different elements on the surface of the sample deposited with TMA and BDBA. Peak locations are also presented as well as FWHM and integrated area.

Name	Peak BE	FWHM (eV)	Area (P) CPS vs eV	Atomic (%)
Al 1s	75.1	2.1	1623.2	22.2
C 1s Scan A	285.2	2.5	2107.8	17.2
C 1s Scan B	290.1	2.7	347.4	7.3
B 1s	192.4	3.3	345.4	7.3
O 1s	532.4	2.9	16197.5	50.5

The general survey showed the presence of a B 1s signal at around 192 eV, C 1s at 285 eV (Scan A) and 290 eV (Scan B) and O 1s at 532 eV. The high-resolution scan for boron is fitted with only one component in Figure 38 and Table 15 reveals both a much higher signal for boron than it would be for an uncoated silicon substrate. The boron content is ca. 7.3%. The one component fitting may correspond to one environment where B is connected to C (from the aromatic unit) and B to O (from B-OH). The prominent O 1s peak at around 532 eV seen in the high-resolution scan indicates that oxygen is present in also one environment. There are two C 1s peaks present on the surface, perhaps representing either B-C or Al-C bonds from unreacted TMA. Aluminum and oxygen content was at 22.2 and 50.5 % respectively, indicating an Al-O ratio of little over 1 to 2.

4.5 The TiCl₄ and BDBA system

The reaction between TiCl₄ and BDBA was investigated by first attempting to deposit a film at 200 °C using 100 cycles of a 0.5s/1s/20s/8s pulse and purge sequence. The results of this deposition are displayed in the following Table 16.

Table 16: Thicknesses before and after deposition of BDBA with TiCl₄. Ellipsometry measurement was done right after the deposition.

TiCl₄ with BDBA	Thickness (nm) The standard deviation: 0.0394 nm		
Substrate number	Si1	Si2	Si3
Before deposition	3.10	4.10	4.82
After deposition	39.48	37.16	34.84

As seen in Table 16, some form of reaction has occurred, resulting in approximately 30 nm film after subtracting the thickness of the silicon substrate before deposition. After this deposition, an additional CVD test was done using a single precursor (TiCl₄), and the result of this deposition was no film growth. This indicates that the acquired film from the initial deposition is not TiO₂, but instead a film that may contain boronic acid. However, more conclusive evidence is required to differentiate the acquired films from one another.

A QCM characterization was performed for this material system. This time only the data of one QCM unit was used due to technical difficulties. The deposition parameters are 0.5s/1s/20s/5s for TiCl₄ and BDBA. It is worth noting that the pulse and purge sequence for depositing TiO₂ is much shorter than the sequence for TiCl₄ and BDBA film. The result of this QCM experiment is presented in Figure 39. A mass increase is seen in both cases during the TiCl₄ pulse, but it is most notable for the TiCl₄ and water sequence. During the TiCl₄ purge in the case of TiCl₄ and BDBA, the mass drops quite rapidly, and we are unsure why, but it may be due to the removal of physisorbed material. The following

BDBA shows signs of saturation, and it is clear that the reaction between TiCl_4 and BDBA has occurred. This system is, therefore investigated further.

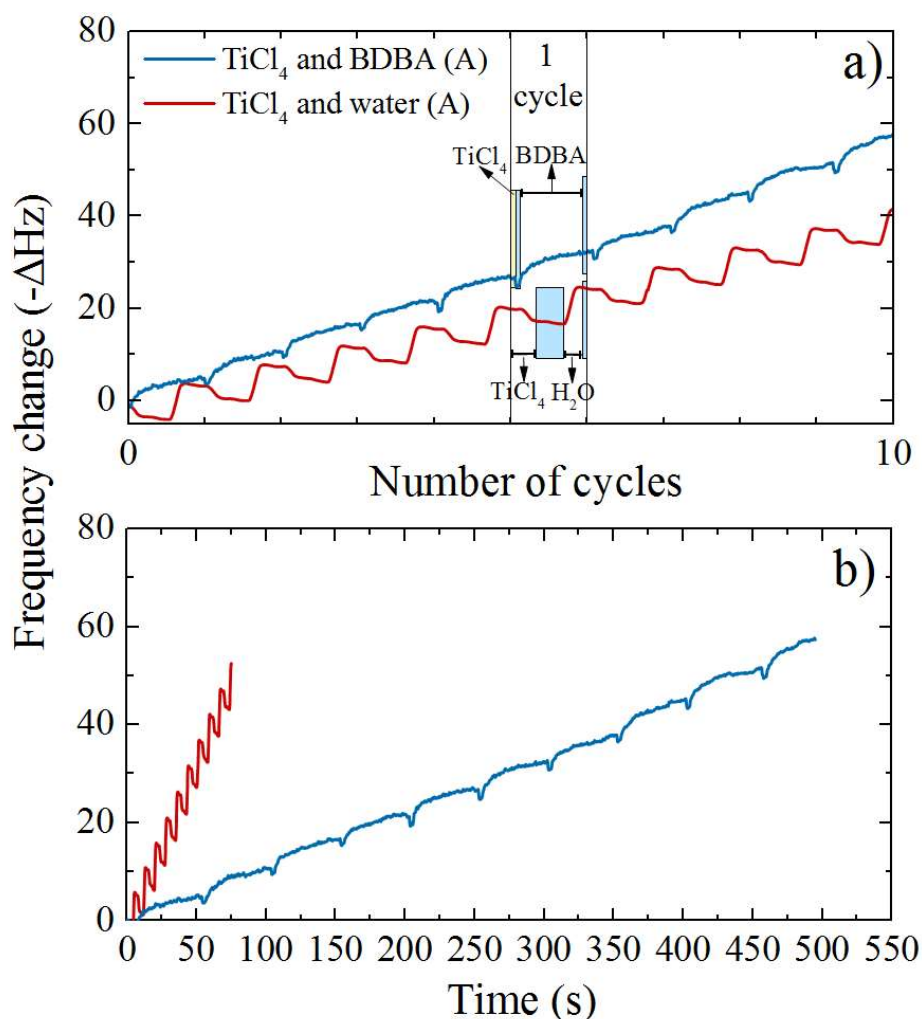


Figure 39: QCM signal response for the TiCl_4 and water (red) and TiCl_4 and BDBA (blue) systems as a function of cycle numbers (a) and time (b). Deposition parameters are described in Table 7. Due to technical difficulties, only the data registered by the front QCM unit is used in this figure. The blue boxes in a) represent purging while the yellow one indicates the TiCl_4 pulse.

By changing individual pulses and purges from the standard pulse and purge sequence 0.5s/1s/20s/8s, as displayed in Figure 40, we could study the growth rate of the system and find the most optimal deposition parameters. We observe that 1 s pulse of TiCl_4 is sufficient to reach saturation, while the following TiCl_4 purge step results in a slow decrease of mass. BDBA, on the other hand, requires approximately 40 s to reach saturation, with a mass slightly decreasing (followed by an increase) with the following purge. 40 s is therefore used as a standard pulse length for BDBA, while 8 s seems to be enough for the purge length.

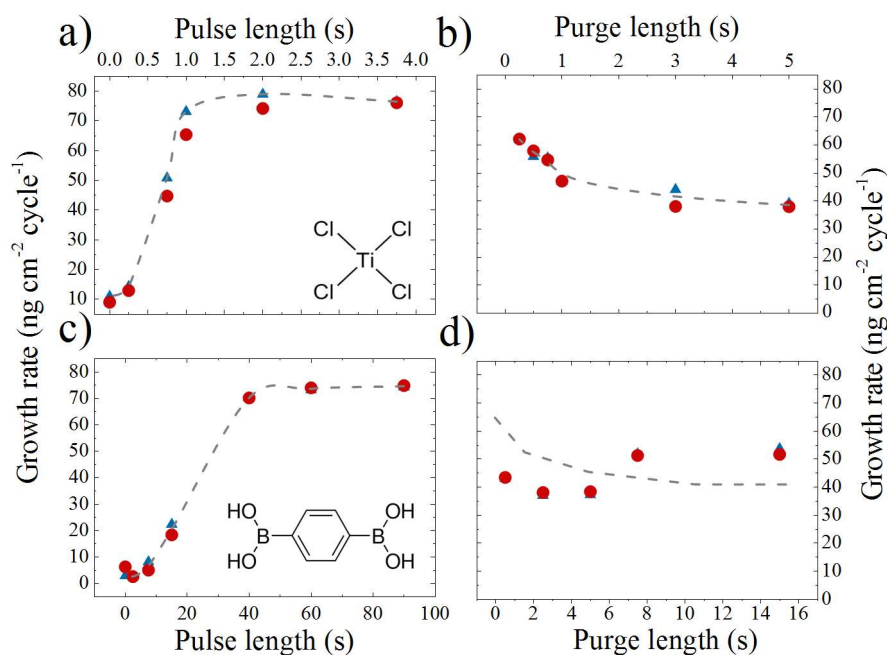


Figure 40: The growth rate of the hybrid TiCl₄ and BDBA system as a function of a) TiCl₄ pulse b) TiCl₄ purge c) BDBA pulse and d) BDBA purge as measured by QCM. Two QCM units were used, placed approximately 5 cm from each other, one positioned in the front of the reaction chamber (black triangles) and one in the back (red circles).

Figure 41 shows the frequency change as a function of time for one cycle for the TiCl₄ and BDBA system, deposited at 200 °C. This measurement shows saturation of the TiCl₄ after around 1 s, while around 40 s pulse for BDBA is seemingly required to reach saturation.

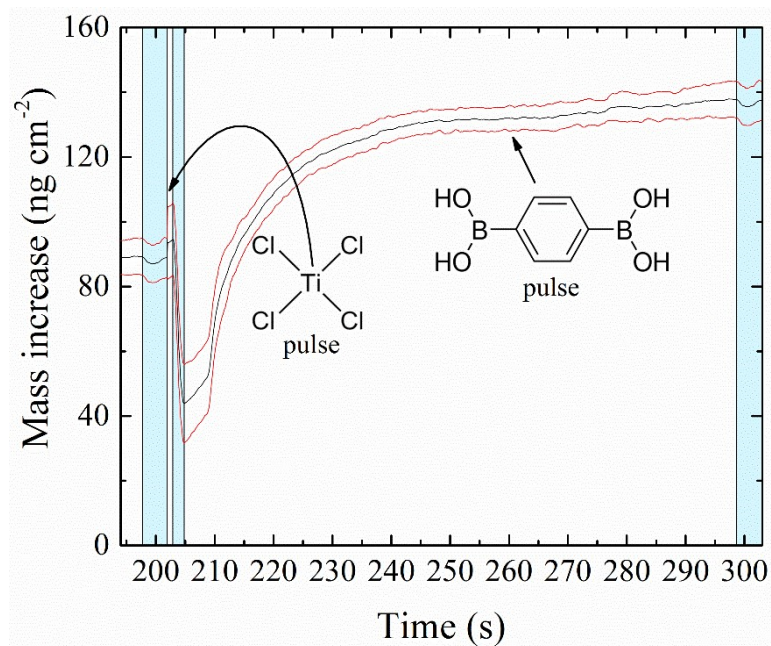


Figure 41: QCM measurement for hybrid TiCl₄ and BDBA system using deposition parameters described in Table 7. The experiment is done at 200 °C, while the figure shows the mass increase (and loss) as the precursors TiCl₄ and BDBA are pulsed and purged. The black line represents the statistical average over 20 consecutive cycles along with their standard deviation, presented in red.

Like for the material system with TMA and BDBA, the growth rate was investigated for TiCl₄ and BDBA system at various deposition temperatures. The proposed pulse and purge lengths based on Figure 40 was 1.5s/1s/40s/8s. The thickness of the samples was measured directly after depositions. The highest growth rates of 1.3 Å/cycle and 1.2 Å/cycle were obtained at 230 and 260 °C respectively, indicating an MLD window, between these temperatures. The results of this investigation are displayed in Figure 42. The refractive index is lowest at 230 and 260 °C. The transparent blue data points in Figure 42 represents the thicknesses of TiO₂ films deposited using pulse and purge sequence 0.5s/3s/0.5s/3s and are presented as a comparison to the thicknesses of TiCl₄ and BDBA films. The growth rate seems to increase from 0.8 Å/cycle to 1.4 Å/cycle with increasing deposition temperature. The refractive indices of these oxide films decrease slightly with deposition temperature, but, compared to hybrid films, have much higher values.

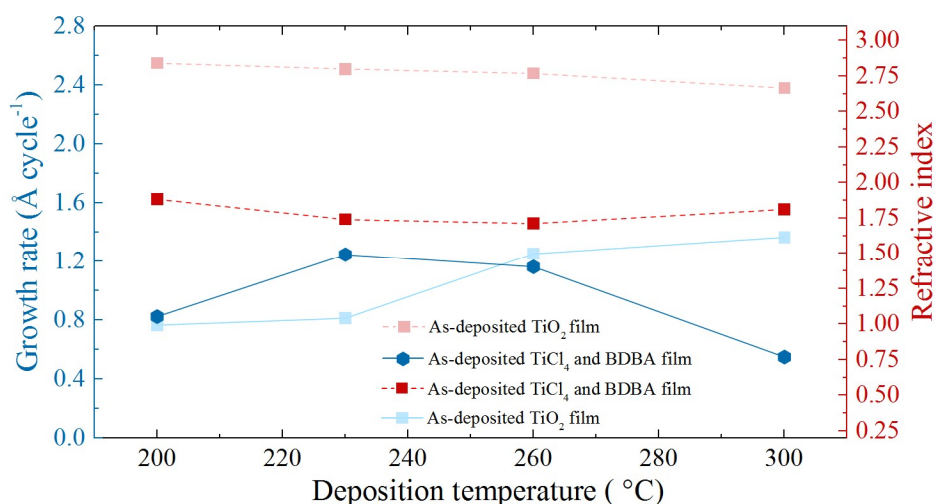


Figure 42: Growth rate and the refractive index of the hybrid TiCl₄ and BDBA system as a function of deposition temperatures. The growth rate of one TiO₂ is also added to the figure represented by the light blue color.

Like in the TMA and BDBA system, the sensitivity to humidity was tested on one of these TiCl₄ and BDBA films deposited at 260 °C using 1000 cycles. Putting a drop of water on the substrate that was in front (in the reaction chamber) during the deposition and then removed it shortly after by absorbing it into a Kleenex tissue did not cause changes in thickness. The following Table 17 presents the result of the experiment.

Table 17: Measured thickness of the TiCl₄ and BDBA film deposited at 260 °C right after deposition and after water treatments (VP3161). The standard deviation of the thickness values is 0.0394 nm.

Time	As deposited	Right after the water drop	24h after the water drop	1 week after the water drop
Thickness	42.90 nm	43.12 nm	43.09 nm	43.42 nm

GIXRD was used to investigate the crystallinity of the films from the predicted MLD-window. The as deposited films at both 230 °C (1000 cycles, ca. 70 nm) and 260 °C (1000 cycles, ca. 45 nm) are x-ray amorphous for a 2θ range 2 - 40 ° (Figure 43a). An XRR measurement was also performed in combination with an AFM analysis for these hybrid films deposited at 230 and 260 °C in Figure 43b) and c), respectively. The densities of the hybrid films were found to be rather low in comparison to the films of the corresponding titanium oxide. The densities of TiCl_4 and BDBA films deposited at both 230 and 260 °C were estimated to be 1.4 g/cm³ and 1.8 g/cm³ respectively as seen in Figure 43b), whereas the TiO_2 films deposited later at both temperatures have densities between 3.2 and 3.7 g/cm³.

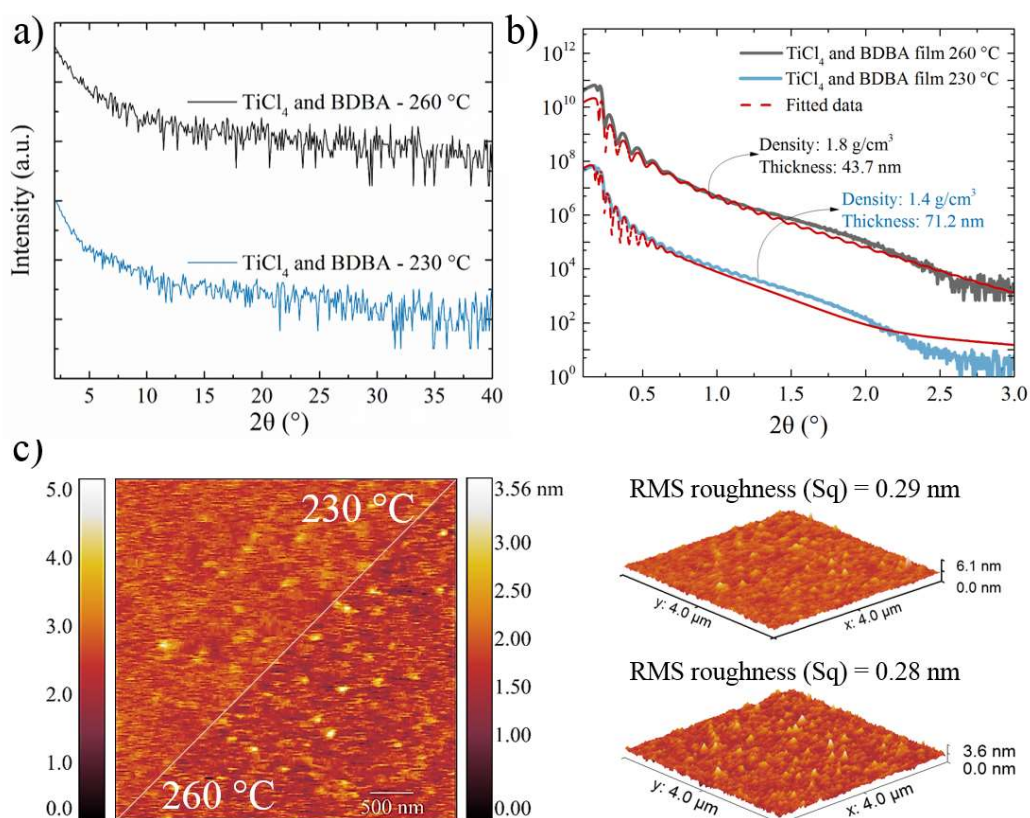


Figure 43: a) A diffractogram of a ca. 45 nm TiCl_4 and BDBA film deposited at 260 °C (black), and a ca. 70 nm TiCl_4 and BDBA film deposited at the 260 °C (blue). b) XRR patterns of TiCl_4 and BDBA films deposited at 260°C (black), 230°C (blue) with data fitting (red). c) The topography of the TiCl_4 and BDBA films deposited at 230 and 260 °C with 1000 cycles are presented on the left. Image area in each panel is 4 μm x 4 μm as seen in 3D images on the right.

The transmittance in the UV and the visible area was investigated using UV-Vis spectroscopy for samples deposited using TiCl_4 and BDBA at 230 and 260 °C. Also, the transmittance of a TiO_2 film deposited at 200 °C is presented in Figure 44, along with the uncoated substrate. The uncoated silica substrate and the TiO_2 film has relatively high transparency in both the UV and the visible range, while the films containing BDBA absorb light with a wavelength of ca. 240 nm.

The absorbance in the visible range increases with increasing deposition temperature. On the other hand, the TiO₂ film deposited at 200 °C seems to have much lower absorbance in the UV range and some in the visible range.

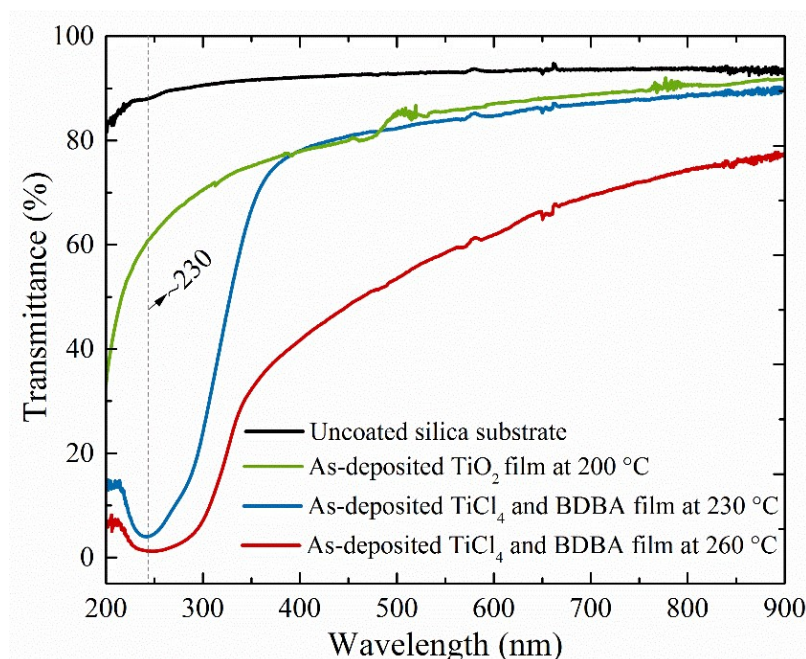


Figure 44: UV-vis spectroscopic analysis of thin films deposited using TiCl₄ and BDBA at 230 °C (blue), at 260 °C (red). The green curve presents the transmittance spectra of TiO₂ film deposited at 200 °C.

The FTIR in the transmission mode of both the hybrid TiCl₄ and BDBA and the TiO₂ films were recorded, and results are shown in Figure 45. The TiO₂ film was deposited by TiCl₄ and H₂O at 230 °C using pulse and purge sequence 0.5s/1s/0.3s/3s. The TiCl₄ and BDBA films were deposited at both 230 and 260 °C using the standard pulse and purge sequence chosen after QCM experiments. Like in the case with TMA and BDBA, Figure 45 contains the FTIR spectrum of both the oxide and hybrid films to try to verify the formation of the hybrid film. There are both differences and similarities between the oxide and the hybrid films FTIR spectra.

The most visible difference is the area between 2900 and 3400 cm⁻¹ attributed the -OH bond, which may indicate the presence of moisture or represents the addition of water molecules to TiCl₄. No such bonds are present for the hybrid films indicating that the hydroxyl groups of BDBA have possibly reacted in the depositions. The area under 500 cm⁻¹ represent the Ti-O, but like in the case with TMA and BDBA, the Ti-O peak is slightly shifted towards higher wavenumber. The stretches at 1419 cm⁻¹ may correspond to the C-C stretching within the aromatic ring (from BDBA).

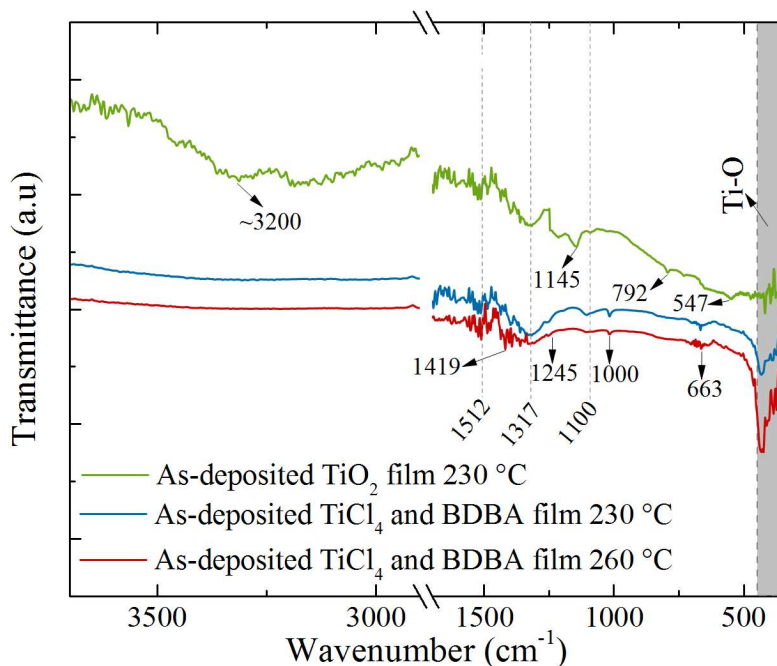


Figure 45: FTIR spectra in transmission mode for a ca. 60 nm thick TiO₂ film deposited at 230 °C (sky blue), a 40 nm thick TiCl₄ and BDBA film deposited at 230 °C (dark blue) and a ca 70 nm thick TiCl₄, and BDBA film deposited at 260 °C (red).

An XPS analysis of the sample from Table 16 deposited with TiCl₄ and BDBA was performed. In Figure 46, the general survey scan is presented on the top along with four high-resolution spectra under, used for the study of the chemical stoichiometry of the surface. The relative atomic percentages of these areas, but also the location of these expressed in eV are displayed in Table 18.

Table 18: XPS spectra of TiCl₄ and BDBA sample from Table 3 at 200°C using 100 cycles.

Name	Peak BE	FWHM (eV)	Area (P) CPS vs. eV	Atomic (%)
B 1s	191.6	1.6	503.2	13.4
C 1s Scan A	284.4	1.5	2418.3	21.9
C 1s Scan B	284.8	2.1	1769.2	18.3
O 1s Scan A	532.9	1.9	5282.6	20.8
O 1s Scan B	530.8	1.9	3999.5	15.7
Ti 2p ³	459.1	1.9	2714.2	9.8

The high-resolution scan for boron is fitted with only one component in Figure 46 and Table 18 reveals both a much higher signal for boron than it would be for an undeposited silicon substrate and the atomic percentage of 13.40%. The prominent O 1s peaks at around 530 eV and 533 eV seen in the high-resolution scan may indicate oxygen present in two different environments, one bonded to titanium and possibly one to boron or even an environment as an OH group. Based on these results, it may be that BDBA is present in the film. On the other hand, due to the spin-orbit splitting of approximately 5.8 eV, Ti 2p level is split into two peaks Ti 2p^{3/2}, and Ti 2p^{1/2} and these two are at 457.0 and 462.0 eV, possibly representing Ti-O bonds.

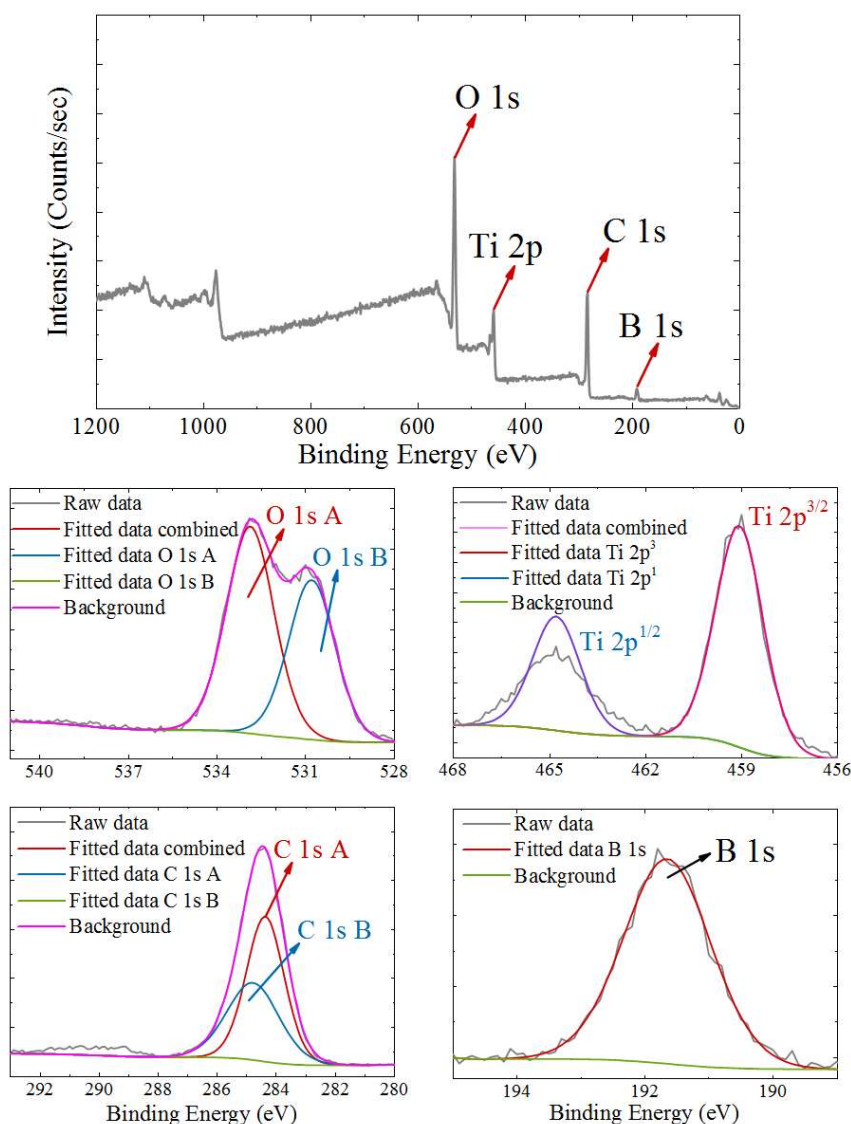


Figure 46: A general survey scan is presented with O 1s, Ti 2p, C 1s, and B 1s signals resolved (top). High-resolution scans around these signals peak fitting performed for each (down). The green line under the raw data and the peak fitting represents the background.

4.6 The TMA and BDBA-BPE system

Substituting BDBA with BDBA-BPE and doing a similar QCM experiment offers the possibility of testing another unknown reaction concerning ALD. Before this, test depositions of TMA and BDBA-BPE films were first attempted to examine the reactivity of BDBA-BPE towards TMA as well as getting a little estimate of possible pulse and purge lengths. The deposition was done at 200 °C in 100 cycles of a 0.4s/1s/60s/8s/ pulse and purge sequence. The result of this deposition is displayed in the following Table 19.

Table 19: Thicknesses before and after deposition of TMA and BDBA-BPE

TMA and BDBA-BPE	Thickness (nm) The standard deviation: 0.0394 nm		
Substrate number	Si1	Si2	Si3
Before deposition	3.12	3.10	3.19
After deposition	11.86	10.40	11.06

As seen in Table 19, the reaction between BDBA-BPE and TMA seems to have occurred. Clear recrystallization of BDBA-BPE was observed in the precursor tube, indicating suitable sublimation temperature of BDBA-BPE was reached. Additional CVD test done after this deposition using TMA seemingly showed no growth of Al_2O_3 . The acquired films could suggest a film with boron moieties inside, so the decision was to characterize the material system further using QCM. Deposition parameters are described in Section 3.1 and Table 8.

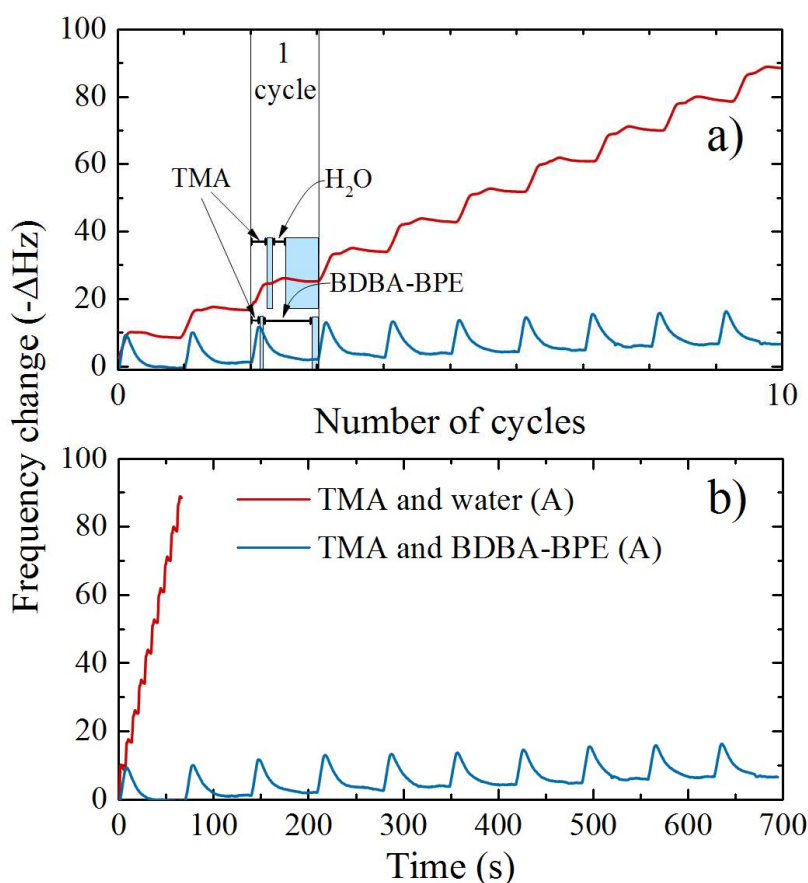


Figure 47: A QCM response test done for TMA and water (red) system and TMA and BDBA-BPE (blue) system. The deposition temperature was 200 °C using pulse and purge sequences 0.3s/3s/0.3s/3s and 0.4s/1s/60s/8s for TMA and water and TMA and BDBA systems, respectively. Only the signal of the front crystal A is considered.

The frequency changes registered at A crystal unit (front) for the reaction between TMA and BDBA-BPE are under 10 Hz, indicating no significant reaction between these two precursors. The frequency change increases only with the TMA pulses while we observe large mass loss with BDBA-BPE pulses. This may be due to the molar weight of BDBA-BPE. The frequency changes for the Al_2O_3

cycles are at least five times higher, indicating much higher growth. Even though there was measurable growth after the TMA and BDBA-BPE deposition and no growth with the following CVD test, it still might be that there were leaks in the reactor during the test deposition. Combined with the results of the QCM experiment where we observe no significant mass gain during BDBA-BPE pulse, the decision was not to continue characterizing this material system.

4.7 The BDBA and BH system

A QCM characterization was attempted for the material system BDBA and BH in the hope that reducing the size of the precursor and lowering sublimation temperature would result in a reaction between these two precursors. Deposition parameters are described in Table 9. The results of the characterization are presented in Figure 48. Figure 48a) shows the frequency change as a function of several cycles, while b) presents the same change as a function of time.

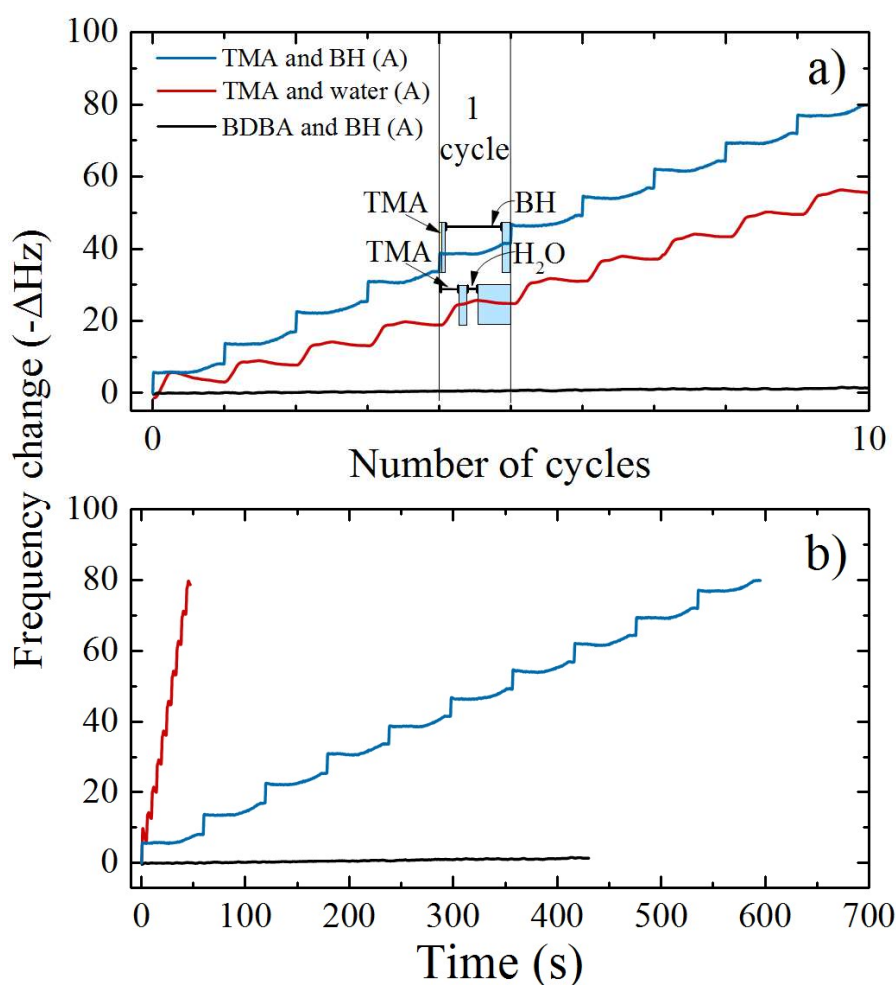


Figure 48: A QCM characterization done for TMA and BH (blue) system using pulse and purge sequence 0.5s/1s/50s/8s, for TMA and water system (red) using pulse and purge sequence 0.4s/1s/0.3s/3s and 20s/8s/10s/5s for BH and BDBA system (black). The experiment was done at 200 °C while the figure displays frequency change as a function of the number of cycles (a) and time in seconds (b). Only the signal of the front crystal A is considered.

Focusing on the sequence containing BH and BDBA, Figure 48a) shows no significant growth for this particular sequence, as there is no significant frequency increase. This may be due to geometric difficulties when first pulsing BH and then BDBA. Some signal is observed, but this is very low. When pulsing TMA first and then BH, a much higher frequency response is obtained. The references with TMA and water are shorter sequences and exhibit a different frequency response than the sequences with TMA and BH. This QCM characterization ultimately shows no MLD growth of film based on the BH and BDBA. However, there is some MLD growth of films based on TMA and BH. This material system is, therefore investigated further in the following chapter.

4.8 The TMA and BH system

Finally, the self-limiting growth of the TMA and BH system was investigated. As previously, this was performed concerning the change of one pulse or one purge lengths at a time of the proposed standard pulse and purge sequence of 0.4s/1s/40s/8s, as seen in Figure 49.

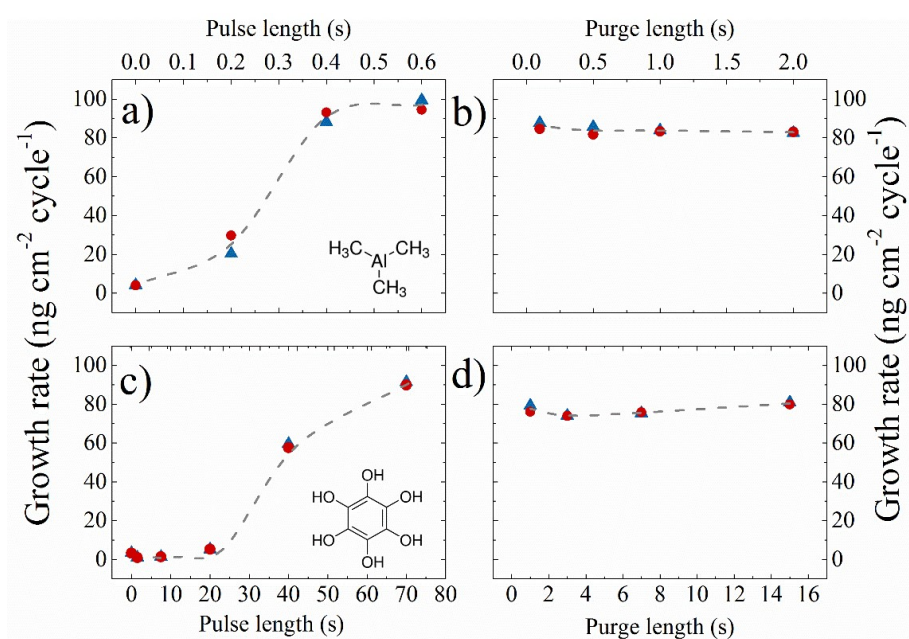


Figure 49: The growth rate of TMA and BH system as a function of a) TMA pulse b) TMA purge c) BH pulse and d) BH purge. Two sensors were used, placed approximately 5 cm from each other, one positioned in the front of the reaction chamber (black triangles) and one in the back (red circles)

Saturation of the surface by BH molecules is not achieved even after 70 seconds, according to Figure 49. This is most probably not due to lack of vapor pressure of the molecules, as BH recrystallizes in the precursor tube. The alternative is most probably slow kinetics. Only one cycle is presented in Figure 50 due to the length of both TMA and BH pulses 0.5s/1s/40s/8s. The red line represents the standard deviation of the QCM measurement. As shown, in Figure 50, the material system based on these two does not exhibit the most definite sign of self-limiting growth. The TMA

pulse shows a clear mass increase, while the mass decrease with following BH pulse and the eventual rise is not normal behavior. The mass gradually increases, but it does not seem to saturate the surface of the crystal due to short exposure of BH.

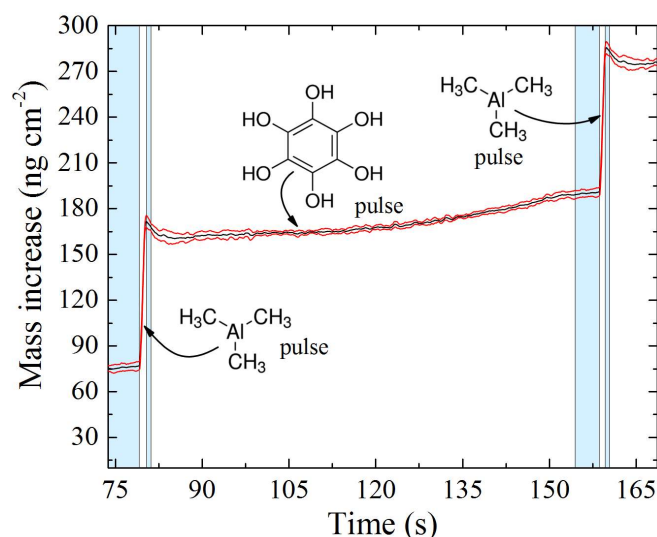


Figure 50: QCM measurement for hybrid TMA and BH system using pulse and purge sequence 0.5s/1s/40s/8s. The experiment is done at 200 °C. The red line shows the standard deviations of the QCM data, while the cyan areas indicate the nitrogen flow is purging the excess or unreacted precursors on the surface of the crystal units.

Due to limited amounts of BH precursor, the above hypothesis regarding the need of longer BH pulse was not possible to investigate further, so the plan became to do one last deposition with 90 s pulse placing different kinds of substrates to have the possibility of characterizing this hybrid system further using different methods. The films were investigated for their stability in air. This was done by monitoring the thickness and refractive index of the film right after and at different times after deposition, as displayed in Figure 51.

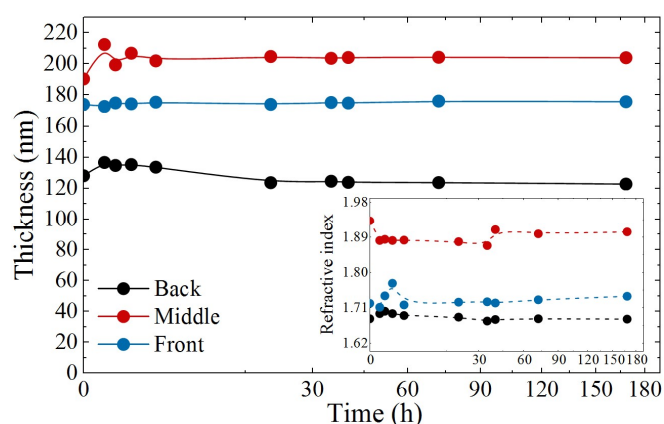


Figure 51: Air stability investigations by measuring thickness and refractive index as a function of time with a square root dependency on the time scale for the hybrid TMA and BH film deposited at 200 °C. Samples considered are front, middle and back substrates in the reaction chamber with thicknesses measured on three different places on each substrate. The mean values of these three are presented in the figure.

The values taken are the mean thickness values measured at three different places on each substrate in the reaction chamber. Hybrid films from this deposition show some increase of thickness and refractive index about 15 hours after the deposition. Afterward, these values seem to be stabilized, indicated by the trend line is quite flat compared to the beginning. The chemical mechanism of this increase is not very clear, but it may be an undesirable reaction between the hybrid film and moisture (and oxygen). Figure 52a) presents the results of GIXRD, while b) shows the AFM measurement.

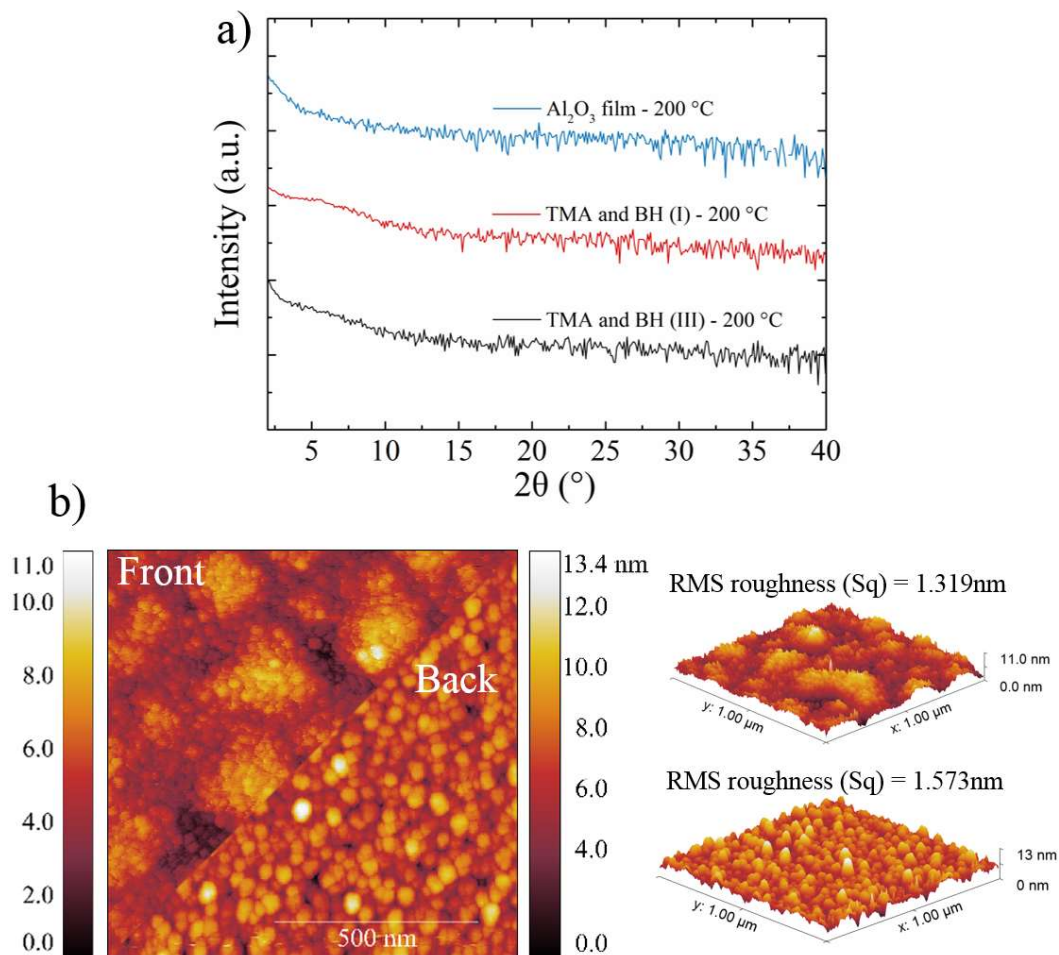


Figure 52: a) A diffractogram of three samples taken for characterization right after deposition. A ca. 150 nm thick TMA and BH film deposited at 200 $^\circ\text{C}$ (black), a TMA and BH film around 150 nm thick deposited at the 200 $^\circ\text{C}$ (red). Also, a diffractogram of 240 nm thick Al_2O_3 deposited at 200 $^\circ\text{C}$ is included (blue). b) The topography of the TMA and BH films deposited at 200 $^\circ\text{C}$ in 1500 cycles. Image area in each panel is 1 μm x 1 μm .

These as deposited hybrids as deposited films at 200 $^\circ\text{C}$ show amorphous character. The GIXRD patterns of two thick Al_2O_3 films deposited at 200 and 300 $^\circ\text{C}$ were considered, for comparison. Thicknesses of the film on the silicon substrate closest to the exhaust (III) and the one furthest away (I) was around 150 nm, while the Al_2O_3 film is about 240 nm. The same TMA and BH films deposited on Si(100) were investigated by AFM (in non-contact mode) to determine surface parameters such as roughness. The RMS roughness of these films compared to films based on BDBA and either TiCl_4 or

TMA are somewhat higher. Simulation of the XRR pattern could not give reliable information about the thickness of the film but revealed a density of 2.5 g/cm³.

UV-Vis measurements were done for an uncoated silica substrate, a TMA and BH film and two Al₂O₃ films both deposited at 200 and 300 °C. The results of these measurements are displayed in Figure 53, where we can confirm the presence of aromatic units present in the structure of TMA and BH film. For this film, the absorbance is quite high in the wavelength region between 200 and 250 nm, and the Al₂O₃ films exhibit no absorption in this region. Oscillating fringes due to high thickness is the same behavior seen in the TMA and BDBA system. The oxide films display almost the same transmittance as the uncoated silica substrate.

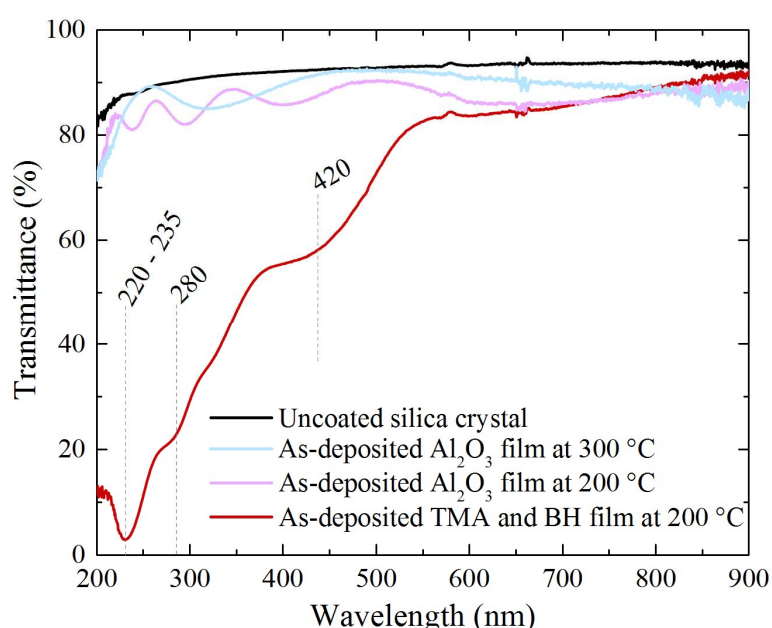


Figure 53: UV-vis spectroscopic analysis of an undeposited silica crystal (black) a thin film deposited using TMA and BH at 200 °C (red). The blue and magenta curve presents the transmittance spectra of Al₂O₃ film deposited at 200 and 300 °C respectively. The measurement is done in the range between 200 and 900 nm.

To verify further the presence of the intended organic units, Figure 54 displays the results of the FTIR reflectometry and transmittance measurements as a function of wavenumber for three samples. The flat and very straight black curve is the transmittance spectrum for an uncoated substrate, while a red represents spectra of TMA and BH film deposited at 200 °C using pulse and purge sequence 0.4s/1s/90s/8s, and the blue represents the Al₂O₃ film deposited at 200 °C using pulse and purge sequence 0.4s/1s/0.3s/1s.

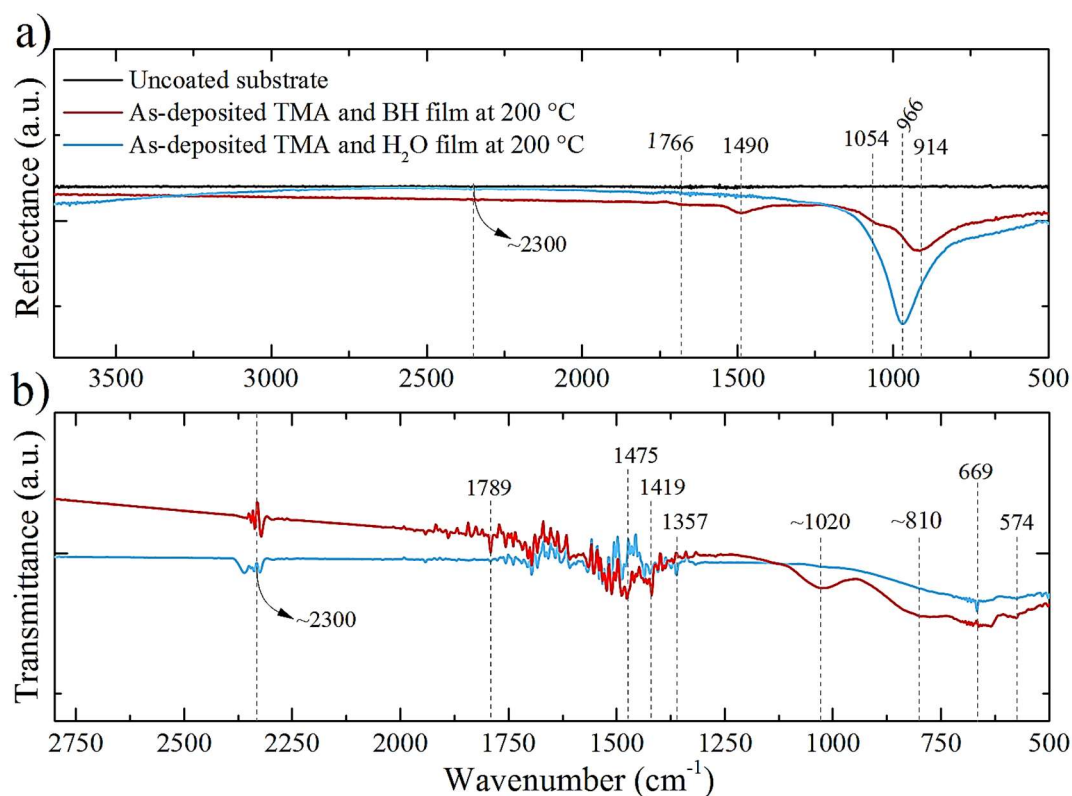


Figure 54: a) Reflectometry FTIR measurement of an uncoated steel substrate (black), of an as deposited TMA and BH film deposited at 200°C (blue) and an as deposited Al_2O_3 film (red). The thickness of the sample represented by the red curve is around 240 nm, while the sample represented by the blue curve has a thickness of around 150 nm. b) Transmittance FTIR spectra of an as deposited TMA and BH film deposited at 200°C (blue) and an as-deposited Al_2O_3 film (red). The thickness of the sample represented by the red curve is around 240 nm, while the sample represented by the blue curve has a thickness of about 150 nm.

5 Discussion

This chapter will first discuss the thermal properties of the precursors listed in Table 1 (Chapter 3). The discussion is then divided into three, where we first discuss the results obtained for the growth of COF-1 and COF-5. Two other parts are discussed through four categories, which are growth, optical properties, bonding, and composition of the obtained boron and lastly BH based hybrid films. All of the results are compared to each other and relevant literature.

5.1 Precursors and their thermal properties

At the beginning of the work, both the precursor tester and TGA were used to investigate the suitability of the precursors BDBA, HMTP, BDBA-BPE, and BH by characterizing their thermal stability. Both of the methods above were performed under conditions that emulated an actual ALD deposition as much as possible. The instruments operate under different pressures, so differences in the results obtained from TGA and precursor tester may originate from the pressure variations.

Generally, an ideal precursor should have a rapid mass drop (or a change in frequency) over a small temperature range correlating to volatilization of the precursor. Note that the volatilization should not be too rapid either, as it could lead to high consumption affecting the efficiency of a deposition process. The temperature at which the precursor is sublimating must be compatible with other parts of the process, as well as the equipment. Ideally as low as possible.

The sublimation temperature of BDBA was initially set to 130 °C based on the results gained from both the precursor tester and TGA. This is in accordance with the experience earlier reported by Pawlak et al.^[62], (130 °C) and Zwaneveld et al.^[59] (150 °C) who also show a similar mass loss process as the one recorded in this work (Figure 24). Based on all these findings and our practical experience, a sublimation temperature of 150 °C was used. Sublimation of HMTP occurs at about 200 °C, but the volatilization occurs very slowly, as it takes place over a much longer temperature range. The thermal properties of HMTP are not well researched, and we have only found one prior report mentioning that HMTP could “further be purified by sublimation at 185°C and 0.03 Torr”^[127]. This temperature is lower than our experience (Figure 24 and 25), which has resulted in the use of 215 °C as the sublimation temperature.

BDBA-BPE sublimates at around 80 °C without any residues as shown by the TGA and the precursor tester. No residual mass indicates that BDBA-BPE does not decompose into a high molecular weight solid, which may be the case for BDBA that had about 55 % remaining mass indicating possible polymerization process into a boroxine structure and eventually COF-1 (Figure 5a). Comparing this to the results obtained from the precursor tester, we no longer see a frequency change for BDBA after 240 °C (Figure 25), which may be related to the polymerization process also, unlike BDBA-BPE, which loses all of its mass after around 90 °C (as evidenced by very rapid frequency increase displayed in Figure 25). Sublimation temperature of BH was determined to be 125 °C using the precursor tester based on the observable first major frequency change in Figure 25. However, the whole sample elevates at one point of the experiment (around 225 °C), which is possibly due to a popcorn effect ejecting the sample (as seen in Figure 55).



Figure 55: One part of the sample BH is starting to elevate at around 225 °C and is removed from the sample holder during the last part of the temperature profile at around 250 °C. This elevation causes the change in the frequency slope in Figure 25 (green curve).

5.2 The reaction of BDBA with itself

In the CVD growth of polymeric materials, a vapor of a precursor must be transferred from one part of the ALD reactor to another to arrive at the surface substrate and adsorb, undergoing chemical polymerization. The overall rate of this process can be controlled by either the abovementioned transfer or the polymerization on the surface of the substrate^[8]. In CVD, growth might also occur in the gas phase, which can be a problem. The OH groups of the boronic acid moieties are efficient hydrogen bond donors and acceptors^[128, 129]. We know that BDBA tends to polymerize due to the irreversible character of the dehydration reactions, such as in Figure 5a).

Our idea was to investigate the polymerization of BDBA and test if it occurs on the surface of a silicon substrate in a CVD type process to make COF-1 structure. Since we dealt with such dehydration reactions as displayed in Figure 5a), the COF-1 inside the reactor would give water as a byproduct. We will return to this bi-product later when discussing the other growth systems where BDBA is involved. The outcome of the test deposition was no growth on the silicon substrates, which may indicate that the reaction occurred already in the gas-phase leading to no available monomers that could diffuse through the reactor onto the substrate and react or just that the reaction rate at which COF-1 would be created is too slow to occur.

5.3 The BDBA and HMTP system

5.3.1 The study of growth

The formation of COF-5 typically occurs as described in Figure 5b) in a polymerization reaction with BDBA and HHTP producing the boronated ester-linked framework^[50, 52, 53]. HHTP, as the building block in this reaction, is a polycyclic compound with the six-hydroxyl group. In terms of an MLD process, the volatility of a precursor is dictated by its intermolecular forces, such as its size and presence of functional groups capable of forming polar bonds. The effects of the functional groups can though be compensated by replacing them with less polarizing groups, such as replacing hydroxyls with methoxy groups. Our choice of precursor to HMTP was based on this latter part, in addition to challenges obtaining HHTP. The thermal properties of HHTP were therefore not tested in this work. As reported, test deposition with BDBA and HMTP did not result in convincing film growth.

This may be due to the decomposition of the HMTP molecule before vaporizing, which is supported by the range of volatilization of HMTP discussed earlier (quite long). Even though we observed the mass loss of HMTP during TGA, it may be that we do not obtain growth possibly due to molecular fragmentation of HMTP. Another explanation may be that reaction rate when using methoxy groups

on HMTP is simply too slow for this MLD process. When comparing the frequency slopes of the TMA and water and TMA and BDBA sequences in Figure 28 we observed same order of magnitude of the frequency change, so we prioritized to find out if BDBA is participating in the growth or if we are just growing oxides films with TMA and the byproduct. Figure 56 presents 3 cycles out of 30 cycles of the reference TMA and water sequence and 3 cycles of the 100 cycles of TMA and BDBA sequence (taken from Figure 28). This is to discuss differences and similarities between the two sequences.

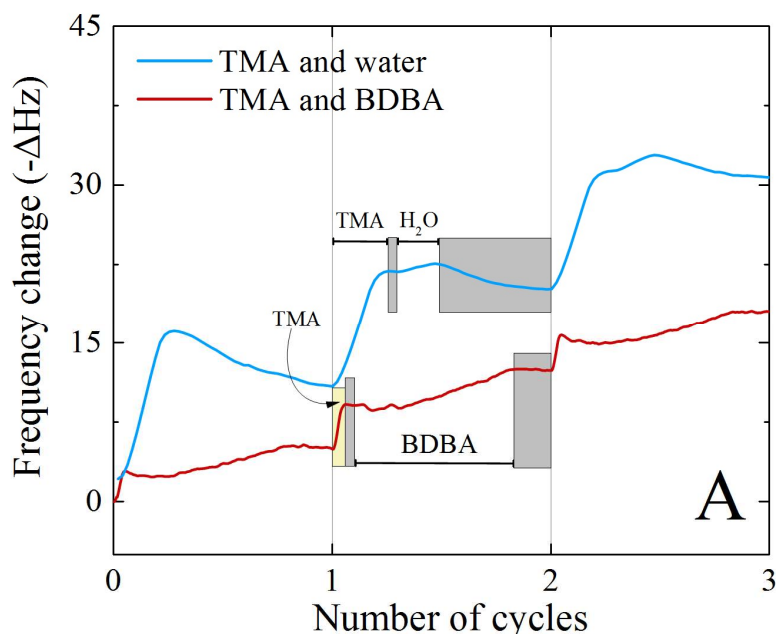


Figure 56: Three cycles of TMA and water reference sequence (blue) and three cycles of TMA and BDBA (red) extracted from Figure 28 to discuss differences and similarities between the two. The extraction is only done for the front crystal A. The box marked with yellow represents TMA pulse while all of the gray boxes represent purging.

We see that the TMA pulse in both cases saturates the surface after 0.4 s, while the following purge showed no significant mass reduction. The water pulse in the reference sequence show typical saturation after 0.3 s, which we would expect to reach with the BDBA pulse in the TMA and BDBA sequence if BDBA polymerized in the precursor boat and released water as a by-product. Instead, we see a mass gain, but unfortunately, the pulse length (15 s, as described in Table 3) is not long enough for BDBA to reach saturation.

Other than that, it was difficult to confirm if the reaction between TMA and HMTP occurred and that is why Figure 29 was used to verify the insignificance of the frequency changes by comparing the frequency slopes in the two experiments (Figure 28 and 29) for the TMA and HMTP sequences. In contrast to this result, the growth of TiCl_4 and HMTP was observed after test depositions did earlier in the project. It was interesting to observe that it did not occur on the silicon substrate but instead on the

glass plate supporting the Si substrate, indicating a possible selective growth. A red/orange color was observed on the glass, which was different from the color that TiO₂ films usually have^[130]. An image of a part of the glass plate is presented in Figure 57 b).

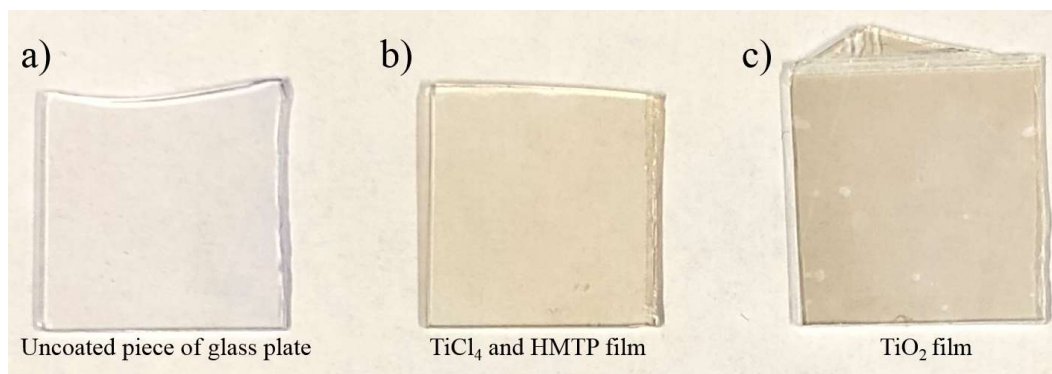


Figure 57: a) An image of an uncoated piece of the glass plate. b) A piece of a glass plate coated with TiCl₄ and HMTP at 300 °C, when the sublimation temperature of HMTP was 215 °C. Sufficient recrystallization was observed which indicated that a flow of precursor entered into the reaction chamber during deposition c) A piece of TiO₂ coated glass plate.

5.3.2 Chemical composition

The XPS analysis of a film deposited on another part of the same glass plate shown in Figure 56 gave a carbon and oxygen feature that did not correspond well with the atomic ratio in the HMTP molecule. We expected a 1:2 between the carbon and the oxygen, and obtained 1: 3.3. This may be due to additions of adventitious carbon^[131]. On the other hand, the Ti: O ratio is not in good agreements with TiO₂^[132] while the 1:1 ratio of C to O may be a sign of more oxygen in the sample than just plain HMTP (where the ratio should be 1:3). It was also interesting to observe a high amount of sodium present in the sample, which may explain the selectivity of the growth. It may be that the presence of such alkaline earth metal can actively influence the thin film growth.

The XPS investigation of the substrates involved in test deposition with BDBA and HMTP showed an atomic weight of boron of around 0.8%. Such low atomic weight of boron corresponds well with previous works done regarding the XPS analysis of SiO₂ surfaces and spectra of B 1s at around 250 °C. The presence of boron is most likely be due to doping of the silicon wafers^[133] and can in this case not be taken as an indication of the presence of BDBA. Note that it is sometimes difficult to detect and confirm the origin of boron due to strong Si 2s plasmon loss features typically overlapping the B 1s region^[134]. Only one carbon peak is observed at 284.5 eV, which is due to an adventitious carbon present in the film^[135].

5.4 The hybrid BDBA systems

5.4.1 The study of growth, optical and structural properties

As shown in Figure 31a) the TMA molecule was chemisorbed on the surface to form the methyl-Al terminated surface after 0.4 s, while the growth rate increased with increasing pulse length of BDBA (instead of reaching a saturation plateau). Similar behavior was acknowledged by Dr. Lausund^[136] in his Ph.D. dissertation experiencing delayed saturation when pulsing 2,6-naphthalenedicarboxylic acid (H₂- 2,6-NDC) which was later explained by the low vapor pressure of the molecule and the steric effects making reaction sites on the surface of the crystal being partially blocked. The vapor pressure problem of BDBA is most likely not a problem in this case since we had the right temperature in the reactor during experiments, but it is important not to use it at higher temperatures, since it may lead to polymerization or even decomposition.

For the hybrid TiCl₄ and BDBA system, the details of mass gain and loss introduced by each precursor in one whole cycle were presented in Figure 41, where we investigated the growth rate as a function of time. The initial mass gain was seemingly due to chemisorption of TiCl₄ to the surface of the QCM unit leading to an exchange reaction between two chlorines in TiCl₄ and the lighter hydroxyl groups from the BDBA molecule resulting in a mass increase (Figure 41). The byproduct of this exchange would be HCl. The course of the following purge step, however, is not as expected. Possible explanations of the quite large and rapid mass loss during the purge may be:

- 1) A temperature effect due to the exothermic reaction between the boronic acid moiety and TiCl₄

As the QCM unit is exposed to the deposition parameters, the deposited structure on the crystal causes the frequency to change as mentioned both in Chapter 2.4.1 (page 18) and in the Chapter 5.3.1. Generally, the primary source of measurement error for the crystal units is the temperature variations of the crystal (Chapter 2.4.1 page 19). For the growth of hybrid TiCl₄ and BDBA films, a possible exothermic reaction between the two precursors during TiCl₄ pulse may have given rise to a temperature increase of the QCM unit, causing a rapid change in frequency, which may be observed as a rapid mass loss during the following purge. It has been shown that such thermal effects occur in metal oxide deposition processes, such as Al₂O₃ processes and with molybdenum^[137]. It is unknown if the between TiCl₄ and BDBA is exothermic or endothermic.

- 2) Rapid mass loss during purge may be attributed to etching reactions that occur when removing the possibly created byproduct HCl, which may eliminate the already adsorbed BDBA molecules (with parts of TiCl₄).

Further, for both systems, the growth rate was investigated as a function of deposition temperatures (Figure 33 and 42). There were indications of two MLD windows between 180 and 340 °C for the system with TMA and BDBA. One is ranging from 180 to 260 °C and a narrower one between 280 and 340 °C. In an investigation done by Klepper et al.^[13] on hybrid thin films, comparable temperature windows were seen. In the case of the TMA and 1,2,4,5-benzene tetracarboxylic acid (1,2,4,5-btc) system, the first window seems to be from 210 to 240 °C and another one between 285 and 300 °C, however with much higher growth rate than TMA and BDBA system (ca. 10 Å/cycle). Still, our hybrid system shows growth rates higher than what Al₂O₃ system typically show (ca. 1 Å/cycle)^[83, 140, 141] at 200 °C. The decreasing growth rate with increasing deposition temperature might be due to increased movement of the precursor molecules allowing them to cover more surface, thus potentially blocking for other molecules to react. On the other hand, the observed MLD window for the TiCl₄ and BDBA system was between 230 and 260 °C with a growth rate of around 1.2 Å/cycle. This is lower than the reported growth rates of TiO₂ between 200 and 300 °C^[142, 143].

As seen in Figure 33, the refractive indices of Al₂O₃ increased with increasing temperature, which is the same trend reported by two other works^[140, 141]. The refractive indices of TiO₂ films show a slight decrease with increasing temperature, which is not in agreement with the work by Su^[142] for instance. Different values of the refractive indices and growth rates per cycle of the BDBA based films different from the corresponding oxides may, therefore, indicate that our structures made by pulsing BDBA have hybrid characters.

Inorganic thin films structures such as in Al₂O₃ or TiO₂ typically have fixed thickness values over time, in contrast to hybrid materials made by MLD that display thickness variations in response to external changes in temperature or air^[144]. Figure 34 was created to investigate the stability in the air for the hybrid TMA and BDBA films between 180 and 300 °C. The initial increase in thickness for all the films below 280 °C until 1500h can be due to the films restructuring to a less dense structure^[145]. This is further supported by the lower density values obtained from the XRR measurement for the amorphous film deposited at 200 °C and higher density value for the amorphous film deposited at 300 °C (Figure 35b). The same air stability test was, unfortunately, not conducted for the TiCl₄ and BDBA system.

The surface roughness of the hybrid films also differs from the reported roughness of corresponding aluminum or titanium oxide in literature^[132, 146]. The low RMS roughness values for TiCl₄ and BDBA films of almost 0.3 nm presented in Figure 43c) indicate extreme smoothness, independent of the deposition temperature. All hybrid films deposited at the observed MLD window temperatures showed GIXRD patterns typical of amorphous materials (Figure 35 and 43), and such patterns have been observed in works with hybrid films before^[12, 13]. This can be due to precursor molecules being bonded

to the surface, orienting themselves in all directions before the complete saturation. The hybrid films also showed significantly lower density values compared to the corresponding amorphous oxide films found in the literature^[147]. This may be due to the higher content of organic components in the hybrid films.

Lastly, an ester alternative to BDBA was paired up with TMA to investigate if such an ester can lead to more effective growth. It was previously reported that the presence of esters (or amide) moieties as ligands could act as cleavage points and hence enabled more effective growth^[148]. The QCM measurement in Figure 47 revealed, however, that the growth rate was precursor limited evidenced by quite slow mass gain with every BDBA-BPE pulse. It seems that too large pulse lengths are needed to obtain substantial growths. For comparison, the TMA and water sequence recorded much higher mass increase during ten cycles when pulsing of both precursors.

To compare, after ten cycles of TMA and BDBA in Figure 28, the frequency change was at about ten times higher, around 100 Hz, which may also be used as evidence when discussing the delay of the growth of TMA and BDBA-BPE. A possible explanation for the prolonged saturation can be a steric hindrance of the pinacol groups on the BDBA-BPE. During the first half-cycle with TMA, a -CH₃ terminated layer is made as presented in Figure 59a). The situation may be like shown in Figure 59b), where during the pulse, some BDBA-BPE molecules obstruct the system from having a proper growth leading to a much to much lower frequency change compared to the Al₂O₃ sequence. Based on no reproducible results that could be obtained after the test deposition and the quite low observed frequency change for the hybrid system with TMA and BDBA-BPE, this system was not explored further.

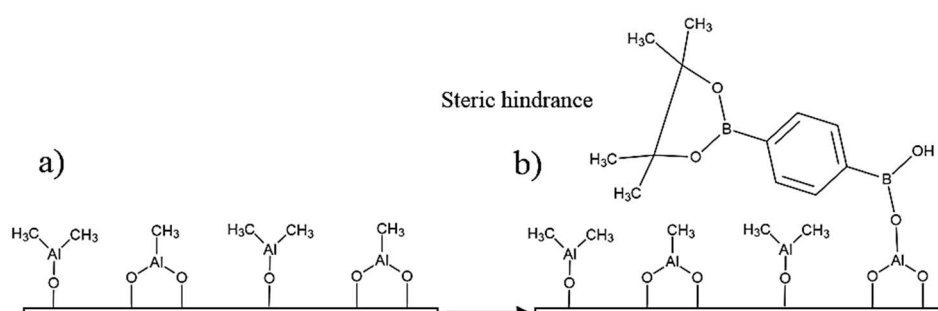


Figure 59: A schematic explanation of how steric hindrance may affect the growth and explain the quite low frequency change in Figure 47. The pinacol ligands and their possible obstruction may lead to fewer BDBA-BPE molecules deposited.

5.4.2 Chemical identity and bonding

The silica substrates are optically colorless in both Figure 36 and 44. When discussing aromaticity of the hybrid films, benzene (like the one present in the BDBA) may typically influence samples absorbance in the UV range, showing a peak at around 240 nm due to the $\pi \rightarrow \pi^*$ transition of the

aromatic unit^[149]. From Figure 36 and 44, it can be seen that in the hybrid samples deposited at the temperature inside the observed MLD windows that such absorbance is present (with varying strengths), increasing with decreasing temperature in the case of TMA and BDBA and increasing with increasing temperature for TiCl₄ and BDBA. The interference fringes that we observed in Figure 36 for Al₂O₃ have a slight fall from 250 nm to 450 nm and an increase in their oscillations with increasing thickness of the films. They may also occur due to partial reflection/transmission through two partially reflecting surfaces. Absorbing films usually show no fringes^[150]. Other UV-Vis spectra found for amorphous Al₂O₃ are in good agreement with what is found here, high transparency of around 85% in the air^[151]. On the other hand, the optical transparency of the TiO₂ film deposited at 200 °C (Figure 44) reduces significantly at the transmission onset (400 nm) which may be related to the low band gap of TiO₂ (around 3.0eV), that makes TiO₂ active in UV^[152].

When it comes to measurements done by FTIR spectroscopy, all spectra of films containing aromatic units with a C-C bond typically display stretches that are found between 1600 and 1585 cm⁻¹, 1500, and 1430 cm⁻¹ and 700 cm⁻¹ due to symmetry^[153]. Para-substituted aromatics usually have stretches at 1430 cm⁻¹^[154]. This value corresponds well with the observed stretch at 1446 cm⁻¹ for both of the TMA and BDBA hybrid films (deposited at 200 and 300 °C) indicating the presence of substituted aromatics in the film. The intensity of these stretches occurring at 1446 cm⁻¹ in Figure 37 seems to increase with lowering of deposition temperature, which may be due to the reduction of precursor content in the samples. The thickness of the samples was around 100 nm for the sample deposited at 200 °C and about 90 nm for the film deposited at 300 °C. The stretch at around 1419 cm⁻¹ in Figure 45 for TiCl₄ and BDBA films may represent the C=C bond from the ring structure, which is not seen for the corresponding oxide films. When it comes to boron bonded to an aromatic unit, the literature reports these stretches to occur between 1075 and 1450 cm⁻¹ meaning that the stretch occurring at around 1240 cm⁻¹ in Figure 37 may be attributed to that bond^[155]. Stretches at around 1000 cm⁻¹ in Figure 45 may also occur due to this interaction.

The strong transmittance intensity observed between 940 – 960 cm⁻¹ in Figure 37 corresponds to the Al-O bond in hybrid films, as documented by previous works^[156]. The observed stretch shift towards higher wavenumbers for the Al₂O₃ films is a behavior previously observed by Abdulagatov et al.^[157]. According to their work, the shift is consistent with the ionic character of Al₂O₃, so it may be that the vibrational features associated with the Al-O bond in the hybrid films are different from the Al-O in the Al₂O₃ structure. On the other hand, the peaks below 500 cm⁻¹ in Figure 45 are assigned to the Ti-O band in both the hybrid and oxide film. However, based on the apparent intensity of the peaks, it may be that there are differences in hybrid and oxide samples in terms of chemical composition. Analysis of the spectra suggests that depositing TiCl₄ and BDBA together results in films slightly different from a TiO₂ film. The presence of aromatic unit along with a Ti-O with much higher intensity may also

support this statement. This shift to higher wavenumbers may occur because of the higher mass of the created molecule is reduced^[158]. A possible hybrid structure with TMA and BDBA would have a much higher mass than an oxide structure because of the size and molecular weight of the aromatic unit. The O-H stretch is known to have wide transmittance ranges on metal oxides. The absence of the –OH stretches for the hybrid films with BDBA may indicate complete consumption of hydroxyl groups by TMA and TiCl₄ since theoretical calculations say all –OH stretching in boronic acid fall in the range between 3634 – 3629 cm⁻¹^[62]. Based on FTIR measurements, we can see that our TMA and TiCl₄ and BDBA films may contain aromatic units while the arrangement of peaks may suggest that the TMA (TiCl₄) and BDBA have reacted to form a structure different from the oxide structures.

5.4.3 Chemical composition

The XPS survey spectra (Figure 38 and 46) of the hybrid films identify boron, aluminum (and titanium), oxygen, and carbon contributions to the surface of the film. The aluminum peak is fitted as a single symmetric peak, and the measured binding energy is slightly above 75 eV, which does not correspond well with the formation of the Al₂O₃ phase^[159-161]. The high-resolution scan of the titanium 2p peak showed a doublet separation between the 2p^{1/2} and 2p^{3/2} peaks of ~6eV, which is indicative of a structure different from oxides (as in TiO₂), where such separation is at around 5.7 eV^[62]. When considering the Al₂O₃ structure, oxygen peak is often deconvoluted to at least two asymmetric peaks associated with Al-O bond usually found at 530 eV and the Al-O-H hydroxyl groups bond is found at 531.4 eV^[163, 164]. Here the oxygen was fitted with one component indicating that the reaction between TMA and the hydroxyl groups have occurred^[165]. The O:Al atomic ratio calculated and presented in Table 15 with the O 1s and Al 1s components is around 2.3, which is not in excellent agreement with the stoichiometry of Al₂O₃, where O:Al ratio is 1.5. The ratio calculated here fits better with a possible hybrid structure.

On the other hand, the O 1s peak in Figure 18 for titanium structure revealed an asymmetric peak with a broader tail on the high-energy side, which indicates the presence of two overlapping peaks. The binding energy of the larger peak is ~532eV corresponds well with the literature data for the oxygen from water. The binding energy of the smaller oxygen peak could be attributed to the O-B bond if compared to literature.

In addition, the deconvolution of the C 1s peaks revealed two distinct components in the TMA and BDBA films, the strongest peak located at 285 eV originating from the C-Al bond in TMA molecule. The other one at approximately 290 eV may originate from the boron acid moiety adsorbed during the MLD process or the B-C bond from the reaction with CO₂ (from the air). Such contaminations have been seen before when analyzing the C 1s region. Literature reports on similar peak arrangements when samples are exposed to ambient air, but this cannot verify that there is contamination in the film

as the C 1s core level is usually fitted with more than two peaks^[141]. So, when discussing the symmetric B 1s high-resolution spectrum fitted by one single chemical environment centered at 192 eV, it might be that the boron contribution comes from boron bonded to the benzene ring rather than the B-C from air^[166]. Unlike the system with BDBA and HMTP, the absence of Si peak in this film proves significant film thickness on the Si substrate.

On the other hand, it is worth mentioning that in Figure 46, chlorine was not detectable, indicating no residual chlorine embedded in the hybrid films. The absence of chlorine may also be related to the absence of residual byproducts of HCl that has absorbed in the film^[167]. As mentioned, no Ti-Cl bond peaks were seen in the transmission spectra of the hybrid films in Figure 44. Since the ratio of Ti and O was 1 to 4 and considering no chlorine in the structure, the bonding may look like the one presented in Figure 58, where Ti is bonded to BDBA on one side and has two oxygen bonds on the other.

5.5 The hybrid BH system

In the case of TMA and BH precursors, no test depositions were performed due to limited amounts of the BH. As shown in Figure 49 and 50 we observe that TMA saturates the surface in about 0.4 s. One TMA and BH cycle presented in Figure 50 does not represent a typical MLD growth. The delayed saturation of the BH may be due to the too short pulse length since we do not observe signs of saturation even after 70 s. There have been investigations of material systems and their optimal pulse length in our research group where saturation does not occur even after 1.5 minutes^[168].

The initial increase of thickness in Figure 51 after the last deposition up until 15h may originate from some unreacted BH molecules reacting with the environment and eventually settling for a structure after 15h, where we do not observe any thickness change. The refractive indices that these films exhibited were nearly the same values of films based on TMA and linkers hydroquinone and benzene-1,3,5-triol^[13], while these are slightly higher than the reported values of Al₂O₃ films^[141]. Compared to films deposited with BDBA where most of the as deposited films were relatively smooth and featureless, the films based on TMA and BH show much higher RMS roughness values obtained from AFM (Figure 52c) which may indicate that BH molecules are possibly better linkers.

The UV-Vis spectra of the TMA and BH deposited on silica clearly showed the presence of aromatic peaks, at around 235 nm and a form of a shoulder at around 280 nm, while it also absorbed light at around 420 nm, which was different from the Al₂O₃ films^[169]. The high transparency of the Al₂O₃ in both the UV and the visible range may support the idea that this hybrid film and oxide films do not have the same chemical bonding. This was also supported by the FTIR measurements in the reflection and transmission modes (Figure 54). In both cases, the broadening stretches at ca. 1055 and 1026 cm⁻¹ respectively originate from C-O bond vibrations. Because these two features appeared in the general

C-O region (typically around 1086 cm^{-1}), it is likely that the strong broadening is due to the troubled C-O bond rather than non-existent C-O like in a situation where Al is inserted into the O-H bond to form a C-O-Al species^[170, 171]. Aluminum alkoxides generally have C-O stretching modes in the region between 1000 and 1100 cm^{-1} were one example of structure such as $\text{Al}(\text{OC}_2\text{H}_5)_3$ exhibits a strong C-O stretching mode peak at 1059 cm^{-1} , just like in the case of these hybrid films^[172]. On the other hand, the abovementioned stretches were not observed for the aluminum oxide films here, which may be a piece of evidence that the TMA does not exclusively react with the water, but hydroxyl groups from a molecule like BH. Also, the higher carbon content of these hybrid TMA and BH films displaying skeletal C-C stretching vibrations within the ring at around 1490 and 1475 cm^{-1} respectively confirms the aromaticity of the films^[173].

The reaction involving the -OH groups from BH with Al from TMA to form an Al-O bond seemed to have occurred since there were no stretches between 3200 and 3700 cm^{-1} in neither Figure 54a) or Figure 54b)^[126]. The Al-O bond stretches are located at around 900 cm^{-1} ^[156] in Figure 54a) for both the hybrid and oxide film, with the only difference that the stretch presents itself at lower wavenumbers for the hybrid indicating different coordination. This was also seen in the TMA and BDBA system. The transmittance spectra for both hybrid and oxide film demonstrate a prominent peak at 574 cm^{-1} Figure 54a), which can be attributed to the Si-O bond^[174]. The same stretch was not observed for the films deposited on steel substrates in Figure 54b).

6 Conclusion

The initial goal of this master project was to grow thin films of COF-1 and COF-5 structures (Figure 5). This proved to be difficult, even though the precursors BDBA and HMTP showed proper sublimation (150 and $215\text{ }^\circ\text{C}$ respectively). No measurable growth of COF-1 was observed through a CVD type of reaction. This is seemingly due to very slow reactions or some form of reaction mechanism that is obstructing this CVD polymerization growth. Attempts of promoting MLD reactions between BDBA and HMTP also failed in the formation of COF-5 at $250\text{ }^\circ\text{C}$.

Combining BDBA with the inorganic precursors TMA and TiCl_4 proved the growth of films of a hybrid character. The QCM experiments showed well saturation behavior when the varying pulse of the inorganic precursors. When varying BDBA pulse lengths in the system with TMA, the saturation occurs slowly while the BDBA pulse saturated the surface thoroughly when used with TiCl_4 , but what we observed there was a significant amount of mass loss during the TiCl_4 purge (most likely due to etching reactions involving HCl). The films from both systems were nevertheless relatively reproducible. The growth rates of the amorphous films based on TMA and BDBA decreased with

increasing temperature (from 1.6 Å/cycle at 180 °C to 0.6 Å/cycle at 340 °C) with two observed MLD windows. The MLD window for the TiCl₄ and BDBA system was observed between 260 and 280 °C with a growth rate of about 1.2 Å/cycle.

QCM analysis of the TMA and BDBA-BPE system showed very slow saturation of BDBA-BPE and was not studied further. Finally, the compound BH was investigated as a new precursor and reacted with TMA. The BH sublimed at 125 °C and films were grown at 200 °C. It does not behave like a conventional MLD system based on the QCM experiment result since only the part of the process with TMA was self-limiting. The saturation of BH is very slow, requiring long pulses (ca. 90 s and maybe higher) for optimal growth. A ca. 150 nm film was grown and proved amorphous while still a high surface roughness compared to BDBA based films.

Properties of these hybrid films were investigated with a variety of characterization methods. Some of the most important results were the identification of aromatic units and the presence of boron in the hybrid films deposited at temperatures in the observed MLD windows for BDBA based films and the BH based film deposited at 200 °C. The $\pi \rightarrow \pi^*$ transition of the aromatic units at around 240 nm occurring was present in all of these (with varying strengths) when studying the UV-vis spectra, while XPS analysis showed significant amounts of boron present in BDBA based films, much more than what silicon substrates usually have (considering boron doping of silicon wafers). The fact that all of the carbons are accounted for in the films suggests the presence of BDBA molecules in both types of hybrid films.

FTIR spectroscopy was used to differentiate between the oxide and the boron-based hybrid films. The intensities of the aromatic C-C stretches exhibited by the hybrid films are perhaps slightly different, but they can confirm the aromaticity in all of them. In addition, the observation that the metal to oxygen bond stretch (Al based systems) are slightly shifted towards higher wavenumbers for oxides suggest different structure of the hybrid films. These hybrid films were also relatively stable in the presence of water after observing no significant thickness changes after the water drop experiments. For BH based hybrid films FTIR spectroscopy in both transmission and reflection mode verifies the aromaticity, along with the UV-Vis measurement. Absorption in both UV and visible light, in contrast to Al₂O₃ is a good indication of that. The oxide films instead showed interference fringes due to much thicker films, which are not features of absorbing films.

7 Future work

Concerning the COF-1 structure, further research should include analyzing the BDBA powder that was inside the precursor boat after CVD polymerization deposition (Table 11). By using the precursor tester on this powder, we can determine if the sample polymerizes already there. Other ways of promoting COF-1 growth in the ALD reactor might be to use precursors consisting of boronic acid moieties on one side and functional groups that bind easier to the silicon surface on the other, granted sufficient sublimation temperature. On the other hand, an interesting finding in this work was that HMTP grew on glass plates rather than silicon substrates during a test deposition, so it would be beneficial to investigate this selectivity further on and to understand why this occurs and how and if sodium influences the selectivity. This might be done through a TOF-ERDA or similar characterization technique that can investigate depth profiles of films with more accuracy than XPS.

Perhaps the growth COF-5 would be possible by considering a change of substrate. Also, if we were to acquire the actual building block of COF-5, which is the HHTP molecule (Figure 5), it would be interesting to first investigate thermal properties of it and then test the effect of having hydroxyl group instead of methoxy on the hydrocarbon. Finding exactly how these COF structures grow inside an ALD reactor might give rise to several different applications. Unlike MOF structures that are already successfully grown by MLD, COF thin films with completely organic metal-free building blocks would potentially rule out the unwanted metals in some application areas, and even better tunable porosity would enable loading guest or drug molecules more efficiently. As mentioned, there were limited amounts of the BH precursor. Future research should include growth rate investigation as a function of different deposition temperature, but also more in-depth QCM measurements and XPS.

8 Bibliography

1. Davidson, M.W., *Robert Hooke: Physics, Architecture, Astronomy, Paleontology, Biology*. Laboratory Medicine, 2010. **41**(3): p. 180-182.
2. Howie, A., J.E. Ffowcs Williams, and J.D. Mollon, *The origins of the concept of interference*. Philosophical Transactions of the Royal Society of London. Series A: Mathematical, Physical and Engineering Sciences, 2002. **360**(1794): p. 807-819.
3. Inaglory, B. *Soap bubble reflects the sky*. 2007 [cited 2019 23.04.]; Available from: https://commons.wikimedia.org/wiki/File:Soap_bubble_sky.jpg.
4. Ebbesen, B. *View of different photographic lenses*. 2010 [cited 2019 05.05]; Available from: https://commons.wikimedia.org/wiki/File:Photographic_lenses_front_view.jpg.
5. Richards, E.H., *Justus Von Liebig, His life and work*. Journal of the American Chemical Society, 1895. **17**(10): p. 833-834.
6. Mairoser, T., J.A. Mundy, A. Melville, D. Hodash, P. Cueva, R. Held, A. Glavic, J. Schubert, D.A. Muller, D.G. Schlom, and A. Schmehl, *High-quality EuO thin films the easy way via topotactic transformation*. Nature communications, 2015. **6**: p. 7716-7716.
7. Mattox, D.M., *Physical vapor deposition (PVD) processes*. Metal Finishing, 2002. **100**: p. 394-408.
8. Wang, M., X. Wang, P. Moni, A. Liu, D.H. Kim, W.J. Jo, H. Sojoudi, and K.K. Gleason, *CVD polymers for devices and device fabrication*. Advanced Materials, 2017. **29**(11): p. 1604606.
9. Leskelä, M. and M. Ritala, *Atomic layer deposition (ALD): from precursors to thin film structures*. Thin Solid Films, 2002. **409**(1): p. 138-146.
10. Malygin, A.A., V.E. Drozd, A.A. Malkov, and V.M. Smirnov, *From V. B. Aleskovskii's "Framework" Hypothesis to the Method of Molecular Layering/Atomic Layer Deposition* Chemical Vapor Deposition, 2015. **21**(10-11-12): p. 216-240.
11. Yoshimura, T., *Molecular Layer Deposition (MLD): Monomolecular-Step Growth of Polymers with Designated Sequences*. Macromolecular Symposia, 2016. **361**(1): p. 141-148.
12. Nilsen, O., K. Klepper, H. Nielsen, and H. Fjellvåg, *Deposition of organic-inorganic hybrid materials by atomic layer deposition*. Ecs Transactions, 2008. **16**(4): p. 3-14.
13. Klepper, K.B., O. Nilsen, and H. Fjellvåg, *Deposition of thin films of organic-inorganic hybrid materials based on aromatic carboxylic acids by atomic layer deposition*. Dalton Transactions, 2010. **39**(48): p. 11628-11635.
14. Klepper, K.B., O. Nilsen, P.-A. Hansen, and H. Fjellvåg, *Atomic layer deposition of organic-inorganic hybrid materials based on saturated linear carboxylic acids*. Dalton Transactions, 2011. **40**(17): p. 4636-4646.
15. Schubert, U. and H. Nicola, *Synthesis of inorganic materials*. 2012.
16. Wang, Z., H. Wang, A. Mitra, L. Huang, and Y. Yan, *Pure-silica zeolite low-k dielectric thin films*. Advanced Materials, 2001. **13**(10): p. 746-749.
17. Mintova, S. and T. Bein, *Nanosized zeolite films for vapor-sensing applications*. Microporous and Mesoporous Materials, 2001. **50**(2-3): p. 159-166.
18. Wu, J., F. Xu, S. Li, P. Ma, X. Zhang, Q. Liu, R. Fu, and D. Wu, *Porous Polymers as Multifunctional Material Platforms toward Task-Specific Applications*. Advanced Materials, 2019. **31**(4): p. 1802922.
19. Chedid, G. and A. Yassin, *Recent Trends in Covalent and Metal Organic Frameworks for Biomedical Applications*. Nanomaterials, 2018. **8**(11).
20. Hoskins, B.F. and R. Robson, *Infinite polymeric frameworks consisting of three dimensionally linked rod-like segments*. Journal of the American Chemical Society, 1989. **111**(15): p. 5962-5964.
21. Shekhah, O., J. Liu, R.A. Fischer, and C. Wöll, *MOF thin films: existing and future applications*. Chemical Society Reviews, 2011. **40**(2): p. 1081-1106.

22. Li, H., M. Eddaoudi, M. O'Keeffe, and O.M. Yaghi, *Design and synthesis of an exceptionally stable and highly porous metal-organic framework*. Nature, 1999. **402**: p. 276.
23. Moghadam, P.Z., A. Li, S.B. Wiggin, A. Tao, A.G. Maloney, P.A. Wood, S.C. Ward, and D. Fairen-Jimenez, *Development of a Cambridge Structural Database subset: a collection of metal-organic frameworks for past, present, and future*. Chemistry of Materials, 2017. **29**(7): p. 2618-2625.
24. Lock, N., Y. Wu, M. Christensen, L.J. Cameron, V.K. Peterson, A.J. Bridgeman, C.J. Kepert, and B.B. Iversen, *Elucidating Negative Thermal Expansion in MOF-5*. The Journal of Physical Chemistry C, 2010. **114**(39): p. 16181-16186.
25. Karagiari, O., M.B. Lalonde, W. Bury, A.A. Sarjeant, O.K. Farha, and J.T. Hupp, *Opening ZIF-8: A Catalytically Active Zeolitic Imidazolate Framework of Sodalite Topology with Unsubstituted Linkers*. Journal of the American Chemical Society, 2012. **134**(45): p. 18790-18796.
26. Yakovenko, A.A., J.H. Reibenspies, N. Bhuvanesh, and H.-C. Zhou, *Generation and applications of structure envelopes for porous metal-organic frameworks*. Journal of Applied Crystallography, 2013. **46**(2): p. 346-353.
27. Øien, S., D. Wragg, H. Reinsch, S. Svelle, S. Bordiga, C. Lamberti, and K.P. Lillerud, *Detailed Structure Analysis of Atomic Positions and Defects in Zirconium Metal-Organic Frameworks*. Crystal Growth & Design, 2014. **14**(11): p. 5370-5372.
28. Zacher, D., O. Shekhah, C. Wöll, and R.A. Fischer, *Thin films of metal-organic frameworks*. Chemical Society Reviews, 2009. **38**(5): p. 1418-1429.
29. Kaur, G., O.P. Pandey, and K. Singh, *Optical, structural, and mechanical properties of different valence-cation-doped bismuth vanadate oxides*. physica status solidi (a), 2012. **209**(7): p. 1231-1238.
30. Zacher, D., R. Schmid, C. Woell, and R.A. Fischer, *Surface chemistry of metal-organic frameworks at the liquid-solid interface*. Angewandte Chemie International Edition, 2011. **50**(1): p. 176-199.
31. Feng, X., W. Chen, and B. Xiang, *Hydrothermal Synthesis, Crystal Structure, and Luminescent Property of a Novel Zn (II)-Organic Framework With Tetranuclear [Zn₄(μ₃-OH)₂] Clusters Linked by an Unsymmetrical Pyridylbenzoate Ligand With Helical Chains*. Synthesis and Reactivity in Inorganic, Metal-Organic, and Nano-Metal Chemistry, 2016. **46**(3): p. 453-457.
32. McKinstry, C., R.J. Cathcart, E.J. Cussen, A.J. Fletcher, S.V. Patwardhan, and J. Sefcik, *Scalable continuous solvothermal synthesis of metal organic framework (MOF-5) crystals*. Chemical Engineering Journal, 2016. **285**: p. 718-725.
33. Darago, L.E., M.L. Aubrey, C.J. Yu, M.I. Gonzalez, and J.R. Long, *Electronic conductivity, ferrimagnetic ordering, and reductive insertion mediated by organic mixed-valence in a ferric semiquinoid metal-organic framework*. Journal of the American Chemical Society, 2015. **137**(50): p. 15703-15711.
34. So, M.C., S. Jin, H.-J. Son, G.P. Wiederrecht, O.K. Farha, and J.T. Hupp, *Layer-by-layer fabrication of oriented porous thin films based on porphyrin-containing metal-organic frameworks*. Journal of the American Chemical Society, 2013. **135**(42): p. 15698-15701.
35. Van de Voorde, B., R. Ameloot, I. Stassen, M. Everaert, D. De Vos, and J.-C. Tan, *Mechanical properties of electrochemically synthesised metal-organic framework thin films*. Journal of Materials Chemistry C, 2013. **1**(46): p. 7716-7724.
36. Buso, D., K.M. Nairn, M. Gimona, A.J. Hill, and P. Falcaro, *Fast synthesis of MOF-5 microcrystals using sol-gel SiO₂ nanoparticles*. Chemistry of materials, 2011. **23**(4): p. 929-934.
37. Bai, X.-j., D. Chen, L.-l. Li, L. Shao, W.-x. He, H. Chen, Y.-n. Li, X.-m. Zhang, L.-y. Zhang, T.-q. Wang, Y. Fu, and W. Qi, *Fabrication of MOF Thin Films at Miscible Liquid-Liquid Interface by Spray Method*. ACS Applied Materials & Interfaces, 2018. **10**(31): p. 25960-25966.

38. Lausund, K.B. and O. Nilsen, *All-gas-phase synthesis of UiO-66 through modulated atomic layer deposition*. Nature Communications, 2016. **7**: p. 13578.
39. Lausund, K.B., V. Petrovic, and O. Nilsen, *All-gas-phase synthesis of amino-functionalized UiO-66 thin films*. Dalton Transactions, 2017. **46**(48): p. 16983-16992.
40. Czaja, A.U., N. Trukhan, and U. Müller, *Industrial applications of metal–organic frameworks*. Chemical Society Reviews, 2009. **38**(5): p. 1284-1293.
41. Van Bui, H., F. Grillo, and J.R. van Ommen, *Atomic and molecular layer deposition: off the beaten track*. Chemical Communications, 2017. **53**(1): p. 45-71.
42. Salmi, L.D., M.J. Heikkilä, E. Puukilainen, T. Sajavaara, D. Grosso, and M. Ritala, *Studies on atomic layer deposition of MOF-5 thin films*. Microporous and Mesoporous Materials, 2013. **182**: p. 147-154.
43. Ahvenniemi, E. and M. Karppinen, *Atomic/molecular layer deposition: a direct gas-phase route to crystalline metal–organic framework thin films*. Chemical Communications, 2016. **52**(6): p. 1139-1142.
44. Gao, X. and X.J. Gao, *Metal-like Boronic–Organic Frameworks: A Design and Computation*. Inorganic Chemistry, 2017. **56**(5): p. 2490-2495.
45. George, S.M., B. H Lee, B. Yoon, A. Abdulagatov, and R. A Hall, *Metalcones: Hybrid Organic–Inorganic Films Fabricated Using Atomic and Molecular Layer Deposition Techniques*. Vol. 11. 2011. 7948-55.
46. Nilsen, O. and D. Scientiarium, *Growth of thin films of functional oxides with the ALCVD method*.
47. George, S.M., B. Yoon, and A.A. Dameron, *Surface Chemistry for Molecular Layer Deposition of Organic and Hybrid Organic–Inorganic Polymers*. Accounts of Chemical Research, 2009. **42**(4): p. 498-508.
48. Park, J., A.C. Hinckley, Z. Huang, D. Feng, A.A. Yakovenko, M. Lee, S. Chen, X. Zou, and Z. Bao, *Synthetic Routes for a 2D Semiconductive Copper Hexahydroxybenzene Metal–Organic Framework*. Journal of the American Chemical Society, 2018. **140**(44): p. 14533-14537.
49. Schoedel, A., M. Li, D. Li, M. O’Keeffe, and O.M. Yaghi, *Structures of Metal–Organic Frameworks with Rod Secondary Building Units*. Chemical Reviews, 2016. **116**(19): p. 12466-12535.
50. Cote, A.P., H.M. El-Kaderi, H. Furukawa, J.R. Hunt, and O.M. Yaghi, *Reticular synthesis of microporous and mesoporous 2D covalent organic frameworks*. Journal of the American Chemical Society, 2007. **129**(43): p. 12914-12915.
51. Guan, X., H. Li, Y. Ma, M. Xue, Q. Fang, Y. Yan, V. Valtchev, and S. Qiu, *Chemically stable polyarylether-based covalent organic frameworks*. Nature Chemistry, 2019. **11**(6): p. 587-594.
52. Colson, J.W., A.R. Woll, A. Mukherjee, M.P. Levendorf, E.L. Spitler, V.B. Shields, M.G. Spencer, J. Park, and W.R. Dichtel, *Oriented 2D Covalent Organic Framework Thin Films on Single-Layer Graphene*. Science, 2011. **332**(6026): p. 228-231.
53. Medina, D.D., V. Werner, F. Auras, R. Tautz, M. Dogru, J. Schuster, S. Linke, M. Döblinger, J. Feldmann, P. Knochel, and T. Bein, *Oriented thin films of a benzodithiophene covalent organic framework*. ACS nano, 2014. **8**(4): p. 4042-4052.
54. Smith, B.J., N. Hwang, A.D. Chavez, J.L. Novotney, and W.R. Dichtel, *Growth rates and water stability of 2D boronate ester covalent organic frameworks*. Chemical Communications, 2015. **51**(35): p. 7532-7535.
55. Evans, A.M., L.R. Parent, N.C. Flanders, R.P. Bisbey, E. Vitaku, M.S. Kirschner, R.D. Schaller, L.X. Chen, N.C. Gianneschi, and W.R. Dichtel, *Seeded growth of single-crystal two-dimensional covalent organic frameworks*. Science, 2018. **361**(6397): p. 52-57.
56. Becker, D., N. Heidary, M. Horch, U. Gernert, I. Zebger, J. Schmidt, A. Fischer, and A. Thomas, *Microporous polymer network films covalently bound to gold electrodes*. Chemical Communications, 2015. **51**(20): p. 4283-4286.

57. Feldblyum, J.I., C.H. McCreery, S.C. Andrews, T. Kurosawa, E.J.G. Santos, V. Duong, L. Fang, A.L. Ayzner, and Z. Bao, *Few-layer, large-area, 2D covalent organic framework semiconductor thin films*. Chemical Communications, 2015. **51**(73): p. 13894-13897.
58. Spitzer, S., A. Rastgoo-Lahrood, K. Macknapp, V. Ritter, S. Sotier, W.M. Heckl, and M. Lackinger, *Solvent-free on-surface synthesis of boroxine COF monolayers*. Chemical Communications, 2017. **53**(37): p. 5147-5150.
59. Zwaneveld, N.A.A., R. Pawlak, M. Abel, D. Catalin, D. Gigmes, D. Bertin, and L. Porte, *Organized Formation of 2D Extended Covalent Organic Frameworks at Surfaces*. Journal of the American Chemical Society, 2008. **130**(21): p. 6678-6679.
60. Medina, D.D., M.L. Petrus, A.N. Jumabekov, J.T. Margraf, S. Weinberger, J.M. Rotter, T. Clark, and T. Bein, *Directional Charge-Carrier Transport in Oriented Benzodithiophene Covalent Organic Framework Thin Films*. ACS Nano, 2017. **11**(3): p. 2706-2713.
61. Bisbey, R.P., C.R. DeBlase, B.J. Smith, and W.R. Dichtel, *Two-dimensional Covalent Organic Framework Thin Films Grown in Flow*. Journal of the American Chemical Society, 2016. **138**(36): p. 11433-11436.
62. Pawlak, R., L. Nony, F. Bocquet, V. Oison, M. Sassi, J.-M. Debierre, C. Loppacher, and L. Porte, *Supramolecular Assemblies of 1,4-Benzene Diboronic Acid on KCl(001)*. The Journal of Physical Chemistry C, 2010. **114**(20): p. 9290-9295.
63. Hujaya, S.D., J.F.J. Engbersen, and J.M.J. Paulusse, *Multilayered Thin Films from Boronic Acid-Functional Poly(amido amine)s As Drug-Releasing Surfaces*. Pharmaceutical Research, 2015. **32**(11): p. 3732-3745.
64. Cambre, J.N. and B.S. Sumerlin, *Biomedical applications of boronic acid polymers*. Polymer, 2011. **52**(21): p. 4631-4643.
65. Jobst, G., I. Moser, M. Varahram, P. Svasek, E. Aschauer, Z. Trajanoski, P. Wach, P. Kotanko, F. Skrabal, and G. Urban, *Thin-Film Microbiosensors for Glucose– Lactate Monitoring*. Analytical Chemistry, 1996. **68**(18): p. 3173-3179.
66. Martin, P.M., *Handbook of Deposition Technologies for Films and Coatings (Third Edition). Chapter 1 - Deposition Technologies: An Overview*. 2010.
67. Johnson, R.W., A. Hultqvist, and S.F. Bent, *A brief review of atomic layer deposition: from fundamentals to applications*. Materials Today, 2014. **17**(5): p. 236-246.
68. Dameron, A.A., D. Seghete, B.B. Burton, S.D. Davidson, A.S. Cavanagh, J.A. Bertrand, and S.M. George, *Molecular Layer Deposition of Alucone Polymer Films Using Trimethylaluminum and Ethylene Glycol*. Chemistry of Materials, 2008. **20**(10): p. 3315-3326.
69. Puurunen, R.L., *A Short History of Atomic Layer Deposition: Tuomo Suntola's Atomic Layer Epitaxy*. Chemical Vapor Deposition, 2014. **20**(10-11-12): p. 332-344.
70. Puurunen, R.L., *Surface chemistry of atomic layer deposition: A case study for the trimethylaluminum/water process*. Journal of Applied Physics, 2005. **97**(12): p. 121301.
71. Miikkulainen, V., M. Leskelä, M. Ritala, and R.L. Puurunen, *Crystallinity of inorganic films grown by atomic layer deposition: Overview and general trends*. Journal of Applied Physics, 2013. **113**(2): p. 021301.
72. Groner, M.D., F.H. Fabreguette, J.W. Elam, and S.M. George, *Low-Temperature Al₂O₃ Atomic Layer Deposition*. Chemistry of Materials, 2004. **16**(4): p. 639-645.
73. Knoops, H.C.M., S.E. Potts, A.A. Bol, and W.M.M. Kessels, *27 - Atomic Layer Deposition*, in *Handbook of Crystal Growth (Second Edition)*, T.F. Kuech, Editor. 2015, North-Holland: Boston. p. 1101-1134. Number of 1101-1134.
74. Pakkala, A. and M. Putkonen, *Chapter 8 - Atomic Layer Deposition*, in *Handbook of Deposition Technologies for Films and Coatings (Third Edition)*, P.M. Martin, Editor. 2010, William Andrew Publishing: Boston. p. 364-391. Number of 364-391.
75. Zydor, A. and S.D. Elliott, *Thermal Stability of Precursors for Atomic Layer Deposition of TiO₂, ZrO₂, and HfO₂: An Ab Initio Study of α -Hydrogen Abstraction in Bis-cyclopentadienyl Dimethyl Complexes*. The Journal of Physical Chemistry A, 2010. **114**(4): p. 1879-1886.

76. Ahvenniemi, E. and M. Karppinen, *ALD/MLD processes for Mn and Co based hybrid thin films*. Dalton Transactions, 2016. **45**(26): p. 10730-10735.
77. Jin, L., Y. Li, Z. Hu, and J. Chu, *Full three-dimensional morphology evolution of amorphous thin films for atomic layer deposition*. AIP Advances, 2018. **8**(4): p. 045304.
78. Potts, S.E., H.B. Profijt, R. Roelofs, and W.M.M. Kessels, *Room-Temperature ALD of Metal Oxide Thin Films by Energy-Enhanced ALD*. Chemical Vapor Deposition, 2013. **19**(4-6): p. 125-133.
79. Groenewoud, W.M., *Characterisation of Polymers by Thermal Analysis. Chapter 2 - Thermogravimetry*, ed. W.M. Groenewoud. 2001.
80. Haines, P.J., *Thermal methods of analysis : principles, applications and problems*. 1995.
81. Shahbazi, S., S.A. Stratz, J.D. Auxier, 2nd, D.E. Hanson, M.L. Marsh, and H.L. Hall, *Characterization and thermogravimetric analysis of lanthanide hexafluoroacetylacetonate chelates*. Journal of radioanalytical and nuclear chemistry, 2017. **311**(1): p. 617-626.
82. Kumar, C.N., *Energy collection via Piezoelectricity*. Journal of Physics: Conference Series, 2015. **662**: p. 012031.
83. Wind, R.A. and S.M. George, *Quartz Crystal Microbalance Studies of Al₂O₃ Atomic Layer Deposition Using Trimethylaluminum and Water at 125 °C*. The Journal of Physical Chemistry A, 2010. **114**(3): p. 1281-1289.
84. Kaipio, M., T. Blanquart, Y. Tomczak, J. Niinistö, M. Gavagnin, V. Longo, H.D. Wanzenböck, V.R. Pallem, C. Dussarrat, E. Puukilainen, M. Ritala, and M. Leskelä, *Atomic Layer Deposition, Characterization, and Growth Mechanistic Studies of TiO₂ Thin Films*. Langmuir, 2014. **30**(25): p. 7395-7404.
85. Nilsen, O. and H. Fjellvåg, *Measuring the heat evolved from individual reaction steps in atomic layer deposition*. Journal of Thermal Analysis and Calorimetry, 2011. **105**(1): p. 33.
86. Radozycki, T., P. Bargiela, and I. Bialynicki-Birula, *Propagation of electromagnetic waves in thin dielectric and magnetic layers*. 2017.
87. J. F. Böttcher, C., O. C. van Belle, P. Bordewijk, A. Rip, and D. D. Yue, *Theory of Electric Polarization I*. Vol. 121. 1974.
88. A. Woollam, J., B. Johs, C. M. Herzinger, J. Hilfiker, R. A. Synowicki, and C. Bungay, *Overview of Variable Angle Spectroscopic Ellipsometry (VASE), Part I: Basic Theory and Typical Applications*. Vol. -1. 1999. 3-28.
89. Benzitouni, S., A. Mahdjoub, and M. Zaabat, *Spectroscopic Ellipsometry Characterization of Thin Films Deposited on Silicon Substrate*. Vol. 4. 2014. 138-142.
90. Xu, H. and H. Feng, *Measurement of Amplitude Ratio and Phase Difference in the Ultra-Wideband Microwave Receiving System*. 2010.
91. Theeten, J. and D. Aspnes, *Ellipsometry in thin film analysis*. Annual Review of Materials Science, 1981. **11**(1): p. 97-122.
92. Bashara, N. and R. Azzam, *Ellipsometry and polarized light*. NH, Amsterdam, 1977.
93. Tompkins, H.G. and J. Hilfiker, *Spectroscopic Ellipsometry. Practical Application to Thin Film Characterization*, 2016.
94. Holy, V., T. Baumbach, and U. Pietsch, *High-resolution X-ray scattering from thin films and multilayers*. 1999: Springer.
95. Tolan, M. and M. Tolan, *X-ray scattering from soft-matter thin films: materials science and basic research*. 1999.
96. Birkholz, M., *Thin film analysis by X-ray scattering*. 2006.
97. Leng, Y., *Materials characterization: introduction to microscopic and spectroscopic methods*. 2009.
98. Levine, J.R., J. Cohen, Y. Chung, and P. Georgopoulos, *Grazing-incidence small-angle X-ray scattering: new tool for studying thin film growth*. Journal of Applied Crystallography, 1989. **22**(6): p. 528-532.

99. Müller-Buschbaum, P., *Grazing incidence small-angle X-ray scattering: an advanced scattering technique for the investigation of nanostructured polymer films*. Analytical and bioanalytical chemistry, 2003. **376**(1): p. 3-10.
100. Daillant, J. and A. Gibaud, *X-ray and neutron reflectivity: principles and applications*. 2008.
101. Lvov, Y., G. Decher, and G. Sukhorukov, *Assembly of thin films by means of successive deposition of alternate layers of DNA and poly (allylamine)*. Macromolecules, 1993. **26**(20): p. 5396-5399.
102. Evmenenko, G., T.T. Fister, F.C. Castro, X. Chen, B. Lee, D.B. Buchholz, V.P. Dravid, P. Fenter, and M.J. Bedzyk, *Structural analysis of the initial lithiation of NiO thin film electrodes*. Physical Chemistry Chemical Physics, 2019. **21**(17): p. 8897-8905.
103. Savage, D., J. Kleiner, N. Schimke, Y.H. Phang, T. Jankowski, J. Jacobs, R. Kariotis, and M. Lagally, *Determination of roughness correlations in multilayer films for x-ray mirrors*. Journal of applied physics, 1991. **69**(3): p. 1411-1424.
104. Karamancheva, I., V. Stefov, B. Šoptrajanov, G. Danev, E. Spasova, and J. Assa, *FTIR spectroscopy and FTIR microscopy of vacuum-evaporated polyimide thin films*. Vibrational spectroscopy, 1999. **19**(2): p. 369-374.
105. Lawrie, G., I. Keen, B. Drew, A. Chandler-Temple, L. Rintoul, P. Fredericks, and L. Grøndahl, *Interactions between alginate and chitosan biopolymers characterized using FTIR and XPS*. Biomacromolecules, 2007. **8**(8): p. 2533-2541.
106. Stuart, B., *Infrared spectroscopy*. Kirk-Othmer Encyclopedia of Chemical Technology, 2000: p. 1-18.
107. MacDonald, S.A., C.R. Schardt, D.J. Masiello, and J.H. Simmons, *Dispersion analysis of FTIR reflection measurements in silicate glasses*. Journal of non-crystalline solids, 2000. **275**(1-2): p. 72-82.
108. Zhang, Y., J. Zhang, Y. Lu, Y. Duan, S. Yan, and D. Shen, *Glass transition temperature determination of poly (ethylene terephthalate) thin films using reflection– absorption FTIR*. Macromolecules, 2004. **37**(7): p. 2532-2537.
109. Tamada, M., H. Koshikawa, F. Hosoi, and T. Suwa, *FTIR reflection absorption spectroscopy for organic thin film on ITO substrate*. Thin solid films, 1998. **315**(1-2): p. 40-43.
110. Kouvetakis, J., M. Todd, B. Wilkens, A. Bandari, and N. Cave, *Novel synthetic routes to carbon-nitrogen thin films*. Chemistry of materials, 1994. **6**(6): p. 811-814.
111. Chalmers, J., N. Everall, and S. Ellison, *Specular reflectance: A convenient tool for polymer characterization by FTIR-microscopy?* Micron, 1996. **27**(5): p. 315-328.
112. Lopez, T., E. Sanchez, P. Bosch, Y. Meas, and R. Gomez, *FTIR and UV-Vis (diffuse reflectance) spectroscopic characterization of TiO₂ sol-gel*. Materials Chemistry and Physics, 1992. **32**(2): p. 141-152.
113. Hsieh, P.-T., Y.-C. Chen, K.-S. Kao, and C.-M. Wang, *Luminescence mechanism of ZnO thin film investigated by XPS measurement*. Applied Physics A, 2008. **90**(2): p. 317-321.
114. Babelon, P., A. Dequiedt, H. Mostefa-Sba, S. Bourgeois, P. Sibillot, and M. Sacilotti, *SEM and XPS studies of titanium dioxide thin films grown by MOCVD*. Thin Solid Films, 1998. **322**(1-2): p. 63-67.
115. Baruwati, B., *Studies on the Synthesis, Characterization, Surface Modification and Application of Nanocrystalline Nickel Ferrite*. 2019.
116. Desai, J., H. Pathan, S.-K. Min, K.-D. Jung, and O.S. Joo, *FT-IR, XPS and PEC characterization of spray deposited hematite thin films*. Applied surface science, 2005. **252**(5): p. 1870-1875.
117. Wu, Q.-H., A. Thissen, and W. Jaegermann, *XPS and UPS study of Na deposition on thin film V₂O₅*. Applied surface science, 2005. **252**(5): p. 1801-1805.
118. Chougule, M.A., S.G. Pawar, P.R. Godse, R.N. Mulik, S. Sen, and V.B. Patil, *Synthesis and characterization of polypyrrole (PPy) thin films*. Soft Nanoscience Letters, 2011. **1**(01): p. 6.
119. Perkampus, H.-H., *UV-VIS Spectroscopy and its Applications*. 2013.

120. Atkins, P. and J. De Paula, *Physical chemistry for the life sciences*. 2011.
121. Moule, D.C. and A.D. Walsh, *Ultraviolet spectra and excited states of formaldehyde*. Chemical Reviews, 1975. **75**(1): p. 67-84.
122. Berova, N., L. Di Bari, and G. Pescitelli, *Application of electronic circular dichroism in configurational and conformational analysis of organic compounds*. Chemical Society Reviews, 2007. **36**(6): p. 914-931.
123. Shibata, T., K. Unno, E. Makino, Y. Ito, and S. Shimada, *Characterization of sputtered ZnO thin film as sensor and actuator for diamond AFM probe*. Sensors and Actuators A: Physical, 2002. **102**(1-2): p. 106-113.
124. Putman, C.A., K.O. Van der Werf, B.G. De Grooth, N.F. Van Hulst, and J. Greve, *Tapping mode atomic force microscopy in liquid*. Applied physics letters, 1994. **64**(18): p. 2454-2456.
125. Pavia, D.L., G.M. Lampman, G.S. Kriz, and J.A. Vyvyan, *Introduction to spectroscopy*. 2008.
126. Van de Kerckhove, K., M.K.S. Barr, L. Santinacci, P.M. Vereecken, J. Dendooven, and C. Detavernier, *The transformation behaviour of "alucones", deposited by molecular layer deposition, in nanoporous Al₂O₃ layers*. Dalton Transactions, 2018. **47**(16): p. 5860-5870.
127. Verlag, G.T., *Science of Synthesis: Houben-Weyl Methods of Molecular Transformations Volume 45b*. 2014.
128. Steiner, T., *The hydrogen bond in the solid state*. Angewandte Chemie International Edition, 2002. **41**(1): p. 48-76.
129. Desiraju, G.R., *Hydrogen bridges in crystal engineering: interactions without borders*. Accounts of chemical research, 2002. **35**(7): p. 565-573.
130. Nuño, M., R.J. Ball, C.R. Bowen, R. Kurchania, and G.D. Sharma, *Photocatalytic activity of electrophoretically deposited (EPD) TiO₂ coatings*. Journal of Materials Science, 2015. **50**(14): p. 4822-4835.
131. Zhou, W., J. Leem, I. Park, Y. Li, Z. Jin, and Y.-S. Min, *Charge trapping behavior in organic-inorganic alloy films grown by molecular layer deposition from trimethylaluminum, p-phenylenediamine and water*. Journal of Materials Chemistry, 2012. **22**(45): p. 23935-23943.
132. Gebhard, M., F. Mitschker, M. Wiesing, I. Giner, B. Torun, T. de los Arcos, P. Awakowicz, G. Grundmeier, and A. Devi, *An efficient PE-ALD process for TiO₂ thin films employing a new Ti-precursor*. Journal of Materials Chemistry C, 2016. **4**(5): p. 1057-1065.
133. Habuka, H., S. Akiyama, T. Otsuka, and W.-F. Qu, *Instability of diborane gas in silicon epitaxial film growth*. Journal of Crystal Growth, 2000. **209**(4): p. 807-815.
134. David, D.G., M.-A. Pinault-Thaury, D. Ballutaud, and C. Godet, *Sensitivity of photoelectron energy loss spectroscopy to surface reconstruction of microcrystalline diamond films*. Applied Surface Science, 2013. **273**: p. 607-612.
135. Mitchell, D., K. Clark, J. Bardwell, W. Lennard, G. Massoumi, and I. Mitchell, *Film thickness measurements of SiO₂ by XPS*. Surface and Interface Analysis, 1994. **21**(1): p. 44-50.
136. Lausund, K.B., *Metal-Organic Frameworks by Molecular Layer Deposition*. 2019.
137. Seghete, D., G.B. Rayner, A.S. Cavanagh, V.R. Anderson, and S.M. George, *Molybdenum Atomic Layer Deposition Using MoF₆ and Si₂H₆ as the Reactants*. Chemistry of Materials, 2011. **23**(7): p. 1668-1678.
138. Nilsen, O., K.R. Haug, T. Finstad, and H. Fjellvåg, *Molecular Hybrid Structures by Atomic Layer Deposition—Deposition of Alq₃, Znq₂ and Tiq₄ (q= 8-hydroxyquinoline)*. Chemical Vapor Deposition, 2013. **19**(4-6): p. 174-179.
139. Haug, K., *Fotoluminescerende materialer tilforbedring av solceller: En studie av Alq₃ og nanopartikler av CdSe*. 2009.
140. Manandhar, K., J.A. Wollmershauser, J.E. Boercker, and B.N. Feigelson, *Growth per cycle of alumina atomic layer deposition on nano- and micro-powders*. Journal of Vacuum Science & Technology A, 2016. **34**(2): p. 021519.

141. Díaz, B., E. Härkönen, J. Światowska, V. Maurice, A. Seyeux, P. Marcus, and M. Ritala, *Low-temperature atomic layer deposition of Al₂O₃ thin coatings for corrosion protection of steel: Surface and electrochemical analysis*. Corrosion Science, 2011. **53**(6): p. 2168-2175.
142. Su, J., *Optimization of TiO₂ Thin Film Growth at Different Temperatures by Atomic Layer Deposition*. 2011.
143. Aarik, J., A. Aidla, H. Mändar, and T. Uustare, *Atomic layer deposition of titanium dioxide from TiCl₄ and H₂O: investigation of growth mechanism*. Applied Surface Science, 2001. **172**(1): p. 148-158.
144. Gleason, K.K., *CVD polymers: fabrication of organic surfaces and devices*. 2015.
145. Momtazi, L., H.H. Sønsteby, and O. Nilsen, *Biocompatible organic–inorganic hybrid materials based on nucleobases and titanium developed by molecular layer deposition*. Beilstein Journal of Nanotechnology, 2019. **10**: p. 399-411.
146. Cappella, A., J.-L. Battaglia, V. Schick, A. Kusiak, A. Lamperti, C. Wiemer, and B. Hay, *High Temperature Thermal Conductivity of Amorphous Al₂O₃ Thin Films Grown by Low Temperature ALD*. Advanced Engineering Materials, 2013. **15**(11): p. 1046-1050.
147. DeCoster, M.E., K.E. Meyer, B.D. Piercy, J.T. Gaskins, B.F. Donovan, A. Giri, N.A. Strnad, D.M. Potrepka, A.A. Wilson, and M.D. Losego, *Density and size effects on the thermal conductivity of atomic layer deposited TiO₂ and Al₂O₃ thin films*. Thin Solid Films, 2018. **650**: p. 71-77.
148. Devi, A., 'Old Chemistries' for new applications: Perspectives for development of precursors for MOCVD and ALD applications. Coordination Chemistry Reviews, 2013. **257**(23): p. 3332-3384.
149. C. Jobanputra, M., M. F. Durstock, and S. Clarson, *Investigation of plasma polymerized benzene and furan thin films for application in opto-electronic devices*. Vol. 87. 2003. 523-528.
150. Poelman, D. and P.F. Smet, *Methods for the determination of the optical constants of thin films from single transmission measurements: a critical review*. Journal of Physics D: Applied Physics, 2003. **36**(15): p. 1850.
151. Ponja, S.D., I.P. Parkin, and C.J. Carmalt, *Synthesis and material characterization of amorphous and crystalline (α-) Al₂O₃ via aerosol assisted chemical vapour deposition*. RSC Advances, 2016. **6**(105): p. 102956-102960.
152. Dai, X., C. Shi, Y. Zhang, and N. Wu, *Hydrolysis preparation of the compact TiO₂ layer using metastable TiCl₄ isopropanol/water solution for inorganic–organic hybrid heterojunction perovskite solar cells*. Journal of Semiconductors, 2015. **36**(7): p. 074003.
153. Günzler, H. and H.-U. Gremlich, *IR spectroscopy. An introduction*. 2002.
154. Xu, H., W. Zhang, Z. Lu, and G. Zhang, *Hybrid polybenzoxazine with tunable properties*. RSC Advances, 2013. **3**(11): p. 3677-3682.
155. J. Bellamy, L., W. Gerrard, M. F. Lappert, and R. L. Williams, *Infrared Spectra of Boron Compounds*. Vol. 481. 1958.
156. Lushington, A., J. Liu, M.N. Bannis, B. Xiao, S. Lawes, R. Li, and X. Sun, *A novel approach in controlling the conductivity of thin films using molecular layer deposition*. Applied Surface Science, 2015. **357**: p. 1319-1324.
157. Abdulagatov, A.I., *Growth, characterization and post-processing of inorganic and hybrid organic-inorganic thin films deposited using atomic and molecular layer deposition techniques*. 2012.
158. Lee, C.S., K.-R. Lee, K.Y. Eun, K.H. Yoon, and J.H. Han, *Structure and properties of Si incorporated tetrahedral amorphous carbon films prepared by hybrid filtered vacuum arc process*. Diamond and Related Materials, 2002. **11**(2): p. 198-203.
159. Wagner, C., W. Riggs, L. Davis, J. Moulder, and G. Muilenberg, *Handbook of X-ray Photoelectron Spectroscopy*, Perkin-Elmer Corp. Eden Prairie, MN, 1979: p. 38.

160. Knapp, C.E., P. Marchand, C. Dyer, I.P. Parkin, and C.J. Carmalt, *Synthesis and characterisation of novel aluminium and gallium precursors for chemical vapour deposition*. New Journal of Chemistry, 2015. **39**(8): p. 6585-6592.
161. Etchepare, P.L., L. Baggetto, H. Vergnes, D. Samélor, D. Sadowski, B. Caussat, and C. Vahlas, *Process-structure-properties relationship in direct liquid injection chemical vapor deposition of amorphous alumina from aluminum tri-isopropoxide*. physica status solidi (c), 2015. **12**(7): p. 944-952.
162. Moses, P., L.M. Wier, J.C. Lennox, H. Finklea, J. Lenhard, and R.W. Murray, *X-ray photoelectron spectroscopy of alkylaminesilanes bound to metal oxide electrodes*. Analytical Chemistry, 1978. **50**(4): p. 576-585.
163. Zheng, L., X. Cheng, D. Cao, G. Wang, Z. Wang, D. Xu, C. Xia, L. Shen, Y. Yu, and D. Shen, *Improvement of Al₂O₃ Films on Graphene Grown by Atomic Layer Deposition with Pre-H₂O Treatment*. ACS Applied Materials & Interfaces, 2014. **6**(10): p. 7014-7019.
164. Jankovský, O., P. Šimek, D. Sedmidubský, Š. Huber, M. Pumera, and Z. Sofer, *Towards highly electrically conductive and thermally insulating graphene nanocomposites: Al₂O₃-graphene*. RSC Advances, 2014. **4**(15): p. 7418-7424.
165. Sherwood, P.M., *Introduction to Studies of Aluminum and its Compounds by XPS*. Surface Science Spectra, 1998. **5**(1): p. 1-3.
166. Jacobsohn, L.G., R.K. Schulze, M.E.H. Maia da Costa, and M. Nastasi, *X-ray photoelectron spectroscopy investigation of boron carbide films deposited by sputtering*. Surface Science, 2004. **572**(2): p. 418-424.
167. Sood, A., P. Sundberg, J. Malm, and M. Karppinen, *Layer-by-layer deposition of Ti-4,4'-oxydianiline hybrid thin films*. Applied Surface Science, 2011. **257**(15): p. 6435-6439.
168. Weibye, K., *Utforsking av potensielle forløparar for atomlagsavsetting av gull*. 2015.
169. Saxena, S., T. Tyson, S. Shukla, E. Negusse, H. Chen, and J. Bai, *Investigation of structural and electronic properties of graphene oxide*. Vol. 99. 2011. 013104-013104.
170. Padbury, R. and J. S. Jur, *Comparison of precursor infiltration into polymer thin films via atomic layer deposition and sequential vapor infiltration using in-situ quartz crystal microgravimetry*. Vol. 32. 2014. 041602-041602.
171. Stoica, A., L. Dobre, S. M., and I. Deleanu, *Fourier Transform Infrared (FTIR) spectroscopy for characterization of antimicrobial films containing chitosan*. 2010.
172. Mukhtar, O.A., *Metal alkoxides as starting materials for hydrolysis processes*. 1999.
173. Ivanova, T.V., P.S. Maydannik, and D.C. Cameron, *Molecular layer deposition of polyethylene terephthalate thin films*. Journal of Vacuum Science & Technology A, 2012. **30**(1): p. 01A121.
174. Liu, L., L. Weng, X. Zhu, L. Yang, and Q. Lei, *The effect of SiO₂/Al₂O₃ weight ratio on the morphological and properties of polyimide/SiO₂Al₂O₃ ternary hybrid films*. 2009.